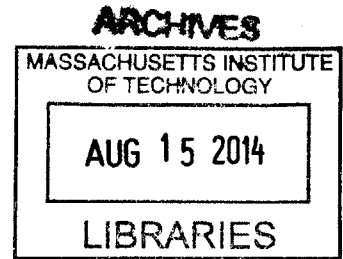# Tuning Energy Transport in Solar Thermal Systems using Nanostructured Materials

by

Andrej Lenert

B.S.E., Mechanical Engineering, University of Iowa, Iowa City, IA (2008)

S.M., Mechanical Engineering, Massachusetts Institute of Technology (2010)

SUBMITTED TO THE DEPARTMENT OF MECHANICAL ENGINEERING

IN PARTIAL FULFILLMENT OF THE REQUIREMENTS FOR THE DEGREE OF

Doctor of Philosophy in Mechanical Engineering

at the

MASSACHUSETTS INSTITUTE OF TECHNOLOGY

June 2014

Signature redacted

Signature of Author: ....

Department of Mechanical Engineering
May 9, 2014

Signature redacted

Certified by: ....

Evelyn N. Wang
Associate Professor of Mechanical Engineering
Thesis Supervisor

Signature redacted

Accepted by: ....

David E. Hardt
Professor of Mechanical Engineering
Chairman, Department Committee on Graduate Students

To my parents

Petar and Gordana Lenert

to my brother

Aleksander Lenert

to my whole family

to my fiancée

Jenna Wiens

Tuning Energy Transport in Solar Thermal Systems using Nanostructured Materials

by

Andrej Lenert

Abstract

Solar thermal energy conversion can harness the entire solar spectrum and theoretically achieve very high efficiencies while interfacing with thermal storage or back-up systems for dispatchable power generation. Nanostructured materials allow us to tune the spectral properties and heat transfer behavior to enable such systems. However, under high temperature conditions, thermal management, system optimization and minimization of parasitic losses are necessary to achieve competitive solar power generation. This thesis seeks to achieve spectral control and thermal management through manipulation of nanostructured materials.

First, this thesis presents the design and development of a nanophotonic solar thermophotovoltaic (STPV) that harnesses the full spectrum of the sun, in a solid-state and scalable way. Through device optimization and control over spectral properties at high temperatures ($\sim$1300 K), a device that is 3 times more efficient than previous STPVs is demonstrated. To achieve this result, a framework was developed to identify which parts of the spectrum are critical and to guide the design of nanostructured absorbers and emitters for STPVs. The work elucidated the relative importance of spectral properties depending on the operating regime and device geometry.

Carbon nanotubes and a silicon/silicon dioxide photonic crystal were used to target critical properties in the high solar concentration regime; and two-dimensional metallic photonic crystals were used to target critical properties in the low solar concentration regime. A versatile

experimental platform was developed to interchangeably test different STPV components without sacrificing experimental control. In addition to demonstrating significant improvements in STPV efficiency, an experimental procedure to quantify the energy conversion and loss mechanisms helped improve and validate STPV models. Using these validated models, this thesis presents a scaled-up device that can achieve 20% efficiencies in the near term. With potential integration of thermal-based storage, such a technology can supply power efficiently and on-demand, which will have significant implications for adoption of STPVs.

Second, the thesis shifts focus away from solid-state systems to thermal-fluid systems. A new figure of merit was proposed to capture the thermal storage, heat transfer and pumping power requirements for a heat transfer fluid is a solar thermal system. Existing and emerging fluids were evaluated based on the new metric as well as practical issues. Finally, sub-micron phase change material (PCM) suspensions are investigated for simultaneous enhancement of local heat transfer and thermal storage capacity in solar thermal systems. A physical model was developed to explain the local heat transfer characteristics of a flowing PCM suspension undergoing melting. A mechanism for enhancement of heat transfer through control over the distribution of PCM particles inside a channel was discovered and explained.

Together, this thesis makes significant contributions towards improving our understanding of the role and the effective use of nanostructured materials in solar thermal systems.

Thesis Committee Chair:
Professor Evelyn N. Wang, Department of Mechanical Engineering, MIT
Thesis Committee Members:
Professor Gang Chen, Department of Mechanical Engineering, MIT
Professor Carl V. Thompson, Department of Material Science and Engineering, MIT

Acknowledgements

Thank you to the members of the Device Research Laboratory. This work would have not been possible without the help and support from my labmates. Special thanks to David Bierman, Youngsuk Nam, Anand Veeraragavan, Tom Humplik, Heena Mutha, Nenad Miljkovic, Jean Sack, Yoshio Perez, Rishi Raj, Ryan Enright, and Thea Szatkowski. More than just being there for research, the DRL family has made my grad school experience an amazing one. I can only smile thinking of all the fun we've had in lab and outside of lab.

Thank you to my advisor Evelyn Wang. Her remarkable leadership style couples enthralling enthusiasm with an incredible sense of thoughtfulness and care. She is passionate and invested in her students, helping them in any way she can and dedicating more time than is seemingly "human". Thank you for taking on a personal interest in my professional success and in my life; I could not have asked for a better advisor.

Thank you to my friends at MIT (Maria Telleria, Jean Chang, Lisa Burton, Ellan Spero, Jamie and Christy Teherani, David Fenning, Kevin Cedrone, Bill Polacheck, Joe Sullivan, Thomas

Ober, and many more) and all of the wonderful communities I've had the pleasure to be a part of (Warehouse, Conner 3, MIT Masters, Brookline St. Ballers, G.A.M.E., and others) ... for being there to either distract me or support me through the challenges, and also to make the celebrations that much more meaningful and fun.

Thank you to my family: for setting the bar high! Starting with my grandma, Milesa, who was one of the first women to get her PhD in the former Yugoslavia and my grandpa, Stevan, who literally set the bar high with his pole vaulting records ... to my aunt and uncle for representing the engineering profession so well and inspiring me to pursue it ... to my brother for being a role model and teaching me patience, moderation, and diplomacy ... to my mom and dad for your determination to provide me with the best opportunities for success and for your love.

Lastly, thank you to Jenna Wiens. You were always there to encourage me, to cheer me on, to consult me, and to give me a very valuable external perspective on my work. Your endless supply of joy and happiness has made life so much more enjoyable here at MIT.

Contents

List of Figures

11

Chapter 1

1. Introduction

1.1   Motivation

The use of concentrated sunlight as a thermal energy source for production of electricity promises to be one of the most viable options to replace fossil fuel power plants. A sufficient amount of solar resources exist in the U.S. to comfortably meet the total electrical power demand of the country [1]. Nevertheless, solar power supplies less than 1% of the U.S. energy consumption [2] because it currently cannot compete with fossil-fuel power plants in terms of efficiency, availability and cost.

Can solar energy be engineered to compete with fossil fuels? Most forms of energy available on Earth, including renewable energy sources such as wind and biomass, are derivatives of solar energy in one form or another. In these derivative forms, the original solar energy has undergone at least one low-efficiency energy conversion step. Even the fossil fuels used today are derivatives of the solar radiation incident on the Earth's surface millions of years ago. It can be argued that engineers should be able to tailor power generation systems for direct utilization of solar radiation with efficiencies exceeding other multi-step energy conversion cycles that rely on the earth to modify solar energy into a higher quality and more readily usable energy source. While certain limits on the efficiency of direct solar power generation exist, current solar thermal technologies are not operating close to these limits which leaves room for improvement for future solar thermal systems.

Power generation devices utilizing solar-thermal energy conversion can harness the entire solar spectrum and theoretically achieve very high efficiencies. To achieve the potential of high efficiencies, high temperatures are needed as understood through Carnot efficiency considerations. Under high temperature conditions, however, system optimization, minimization of parasitic losses, and thermal management are important to achieve competitive solar power generation devices.   This thesis seeks to achieve spectral control and thermal management through an understanding of micro/nanoscale phenomena and materials.

Specifically, this thesis aims to contribute toward addressing the fundamental issues with solar power generation: efficiency and dispatchability. To address the issue of efficiency, it investigates solar thermophotovoltaic devices which in principle can achieve high efficiencies in a solid-state and scalable way. Dispatchability is addressed in the second part of the thesis, where engineered fluids, such as sub-micron phase change material (PCM) suspensions, are investigated for simultaneous enhancement of heat transfer and thermal storage capacity in solar thermal systems.

1.2 Background: Solid-State Systems

The most common approaches to generate power from sunlight are either photovoltaic (PV), in which sunlight directly excites electron-hole pairs in a semiconductor, or solar-thermal, in which sunlight drives a mechanical heat engine. Photovoltaic power generation is intermittent and typically only exploits a portion of the solar spectrum efficiently, whereas increased irreversibilities in smaller heat engines make the solar thermal approach best suited for utility-scale power plants.

Solar thermophotovoltaics (STPVs), on the other hand, promise to leverage the benefits of both approaches:

Highly efficient— STPVs (like CSP) harness the entire solar spectrum including high-energy and infrared photons while PVs only utilize a portion of the solar spectrum efficiently [3-5]. Because of the ability to harness the entire solar spectrum, an STPV device can achieve power generation efficiencies overcoming the Shockley-Queisser single-junction PV limit [3, 4] and on par with those of concentrated multi-junction photovoltaics [6].

Scalable and low-maintenance— STPVs are solid-state and scalable (like PV), whereas CSP is best suited for utility scale power plants, limiting its ubiquity and stalling reductions in cost.

Dispatchable— Because of the intermediate conversion to heat, STPVs (like CSP) are well-suited to provide electricity on-demand through a thermal-based energy storage system or a fuel-based back-up system [7-9]. In contrast, power generation using PVs is intermittent while the cost of electricity storage is high; two factors limiting the penetration of PVs to 5-15% of the U.S. primary energy supply [10].
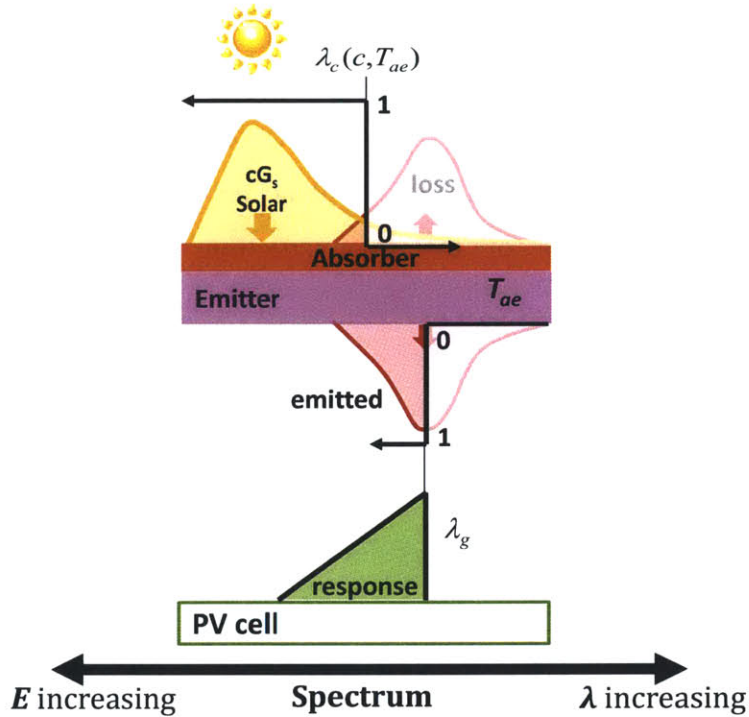
Figure 1-1 | Operating principle of a solar thermophotovoltaic.
Incident concentrated sunlight is absorbed and turned into outgoing thermal emission that matches the spectral response of a single-junction cell.

In STPVs, sunlight is absorbed and turned into heat raising the temperature of the emitter. The thermal emission from the emitter is tuned to match the spectral response of the photovoltaic cell. Ultimately, the broad solar spectrum incident on the absorber is converted into a narrower spectrum leaving the emitter, and can thus improve the overall efficiency. STPVs can be thought of as a solar-powered high-temperature solid-state heat engine. Alternatively, they can be considered as a non-linear optical element or material that creates an 'artificial sun' for a single-junction cell [11].

Since no portion of incident sunlight reaches the PV cell directly, the performance of STPVs is determined by the efficiency of several intermediate energy conversion steps. Optically concentrated sunlight is converted into heat in the absorber; the absorber temperature rises; heat conducts to the emitter; the hot emitter thermally radiates towards the PV cell, where radiation is ultimately converted into excited charge carriers and electricity (Fig. 1a). The overall efficiency (η_{stpv}) can be expressed as a product of the optical efficiency of concentrating sunlight (η_o), the thermal efficiency of converting and delivering sunlight as heat to the emitter (η_t), and the efficiency of generating electrical power from the thermal emission (η_{tpv}):

16

1-1
$$\eta_{stpv} = \eta_o \eta_t \eta_{tpv}$$

In order to excite enough thermal modes for substantial emission above the bandgap, the emitter temperature should [12] be high enough such that Planck's blackbody peak approaches the bandgap:

1-2
$$T_e^{opt} \approx 2336 \,[K/eV] \cdot E_g$$

In order to reach high efficiencies, the process relies heavily on filter-like properties in both the absorber and the emitter. The ideal spectral properties on the absorber go from high absorptance to low emittance at the cut-off wavelength in order to absorb sunlight and suppress thermal emission. The ideal spectral properties in the emitter have high emittance above the bandgap and low emittance at energies below the bandgap in order to maximize the matching between the thermal radiation and the spectral response of the cell, and eliminate low-energy emission.

The challenge with STPVs is that these filter-like properties that abruptly go from high emissivity to low emissivity are required in materials operating at high temperatures. No naturally-occurring materials meet these requirements and display these properties. Thus, efficient collection of sunlight in the absorber and spectral control in the emitter are particularly challenging. This drawback has limited prior experimental demonstrations of this approach to conversion efficiencies around or below 1% [13-15].

For the absorber, one approach to effectively enhance the intrinsic solar absorptivity of materials is to use macro cavity geometries. Because of the high aspect ratio of the cavity needed to enhance absorption, this approach typically requires high levels of optical concentration to reach T_e^{opt} (e.g., 3,183 times as used by Datas and Algora [13], 4,600 times as used by Vlasov et al.[14]). Such high optical concentration in turn requires complex systems with relatively low optical efficiencies ($\eta_o\sim$65%) [13].

For the emitter, the intrinsic spectral selectivity of tungsten is poor at T_e^{opt} since the emissivity at low photon energies ($< E_g$) increases with temperature, accompanying an increase in the electrical resistivity [16].

To improve the performance of the absorber-emitter, this thesis investigates the use of nanostructured and nanophotonic surfaces to tailor the spectral properties of the absorber-emitter. Although the underlying material properties are sensitive to temperature, the surface structure affords a degree of spectral tunability which is temperature independent. This is accomplished in a compact planar layout without resorting to more complex STPV configurations.

Researchers have investigated the design of structured surfaces [5, 7, 17-24] with spectral properties approaching those of ideal STPV components; specifically, the use of photonic crystals to control the photon density of states for narrow-band selective emission [5, 7, 17-23]. Recent developments of selective metal-based surfaces have demonstrated 1D, 2D, and 3D metallic photonic crystal structures capable of tailoring the emissivity spectrum. Two-dimensional metallic air photonic crystals (MAPhC) have been demonstrated to selectively absorb/emit light in the near infrared via cavity modes. Metamaterial and plasmonic based absorbers have demonstrated wide angle absorption due to their subwavelength periodic structures. Simulation studies using realistic nanophotonic surfaces predict STPV efficiencies exceeding 40% [5, 18, 24]. Nevertheless, these surfaces have not yet been fabricated and integrated into STPV devices operating at high enough temperatures for efficient power conversion.

1.3   Background: Thermal-Fluid Systems

Heat transfer fluids serve one or more purposes in solar thermal applications, such as: collection and transport of heat from solar absorbers; intermediate storage of thermal energy to buffer the diurnal nature of solar radiation; and heat exchange with the power cycle to produce electricity. As a result of the multiple purposes of heat transfer fluids in these applications, many constraints, both performance and practical, influence the choice of heat transfer fluid. The choice of heat transfer fluids has significant effects on the performance, cost and reliability of solar thermal systems.

In typical concentrated solar power (CSP) applications, heat transfer fluids are required to have low freezing points (near room temperature) to avoid freezing overnight, high operating temperatures (>400°C) to increase the power cycle efficiency, and low vapor pressures at high temperatures to reduce installation costs. For heat transfer performance, fluids are expected to have high thermal conductivity, high volumetric heat capacity, and low viscosity. They also need to be environmentally benign, non-corrosive, safe and cost-effective. Since pure substances and commonly used fluids such as synthetic oils and molten salts rarely meet all of the practical and performance criteria, the development of new solar heat transfer fluids continues to be an active area of research. Two of the most commonly pursued research avenues include: mixtures, such as multi-component salts; and composite fluids, such as suspensions of submicron-sized solid particles in liquids (i.e., nanofluids). New developments have been discovered in the recent years in the field of mixtures and composite fluids, such as nanofluids and phase-change material suspensions, which can potentially lead to significant breakthroughs for solar thermal applications.

When suspended in a heat transfer fluid, micron-sized encapsulated phase-change materials (PCMs) serve to increase the effective heat capacity of a fluid over a relatively small temperature range as the inner core undergoes melting or phase-change. PCMs are most commonly composed of a wax or organic inner core and a polymer-based outer shell; paraffin is the most common inner core material because of its relatively high latent heat, low vapor pressure, negligible supercooling and chemical stability [25]. Since the systems are operated with a limited temperature difference between source and sink, the enhancement of effective heat capacity resulting from the latent heat of fusion increases the energy storage density. Consequently, either thermal performance is improved or the pumping power requirement may be reduced.

Previous studies have developed numerical models to understand the hydrodynamic and heat transfer characteristics of PCM suspensions (*i.e.*, slurries). A review by Dutil *et al.* focuses on numerical studies modeling convective heat transfer in PCM suspensions with summaries of methods, model validation steps and main contributions [26]: while, Zhang *et al.* summarizes work addressing material properties and applications of PCM suspensions [27]. Most of the numerical studies model the slurry as a bulk fluid using the effective heat capacity model [28-34] originally introduced by Alisetti *et al.* [28]. Alternative approaches treat the latent heat as an additional source term representing the absorbed heat during the phase change process in the PCM [35, 36], or describe the carrier fluid and the PCM phases using separate conservation equations with appropriate interaction terms [37].

Experiments have also been conducted to evaluate the heat transfer characteristics of PCM suspensions [38-48]; results from forced convection, constant heat flux experiments with suspensions of microencapsulated PCM particles show the effects of the *Stefan* number, the PCM mass fraction, the flow rate, the flow regime, the inlet temperature subcooling, and the particle size. The thermal performance tends to increase as the mass fraction increases, but the optimal mass fraction balances both the heat transfer enhancement and the pumping power increase [40, 41, 48]. To improve the effective thermal conductivity of slurries, investigators have studied hybrid suspensions of alumina nanoparticles and PCMs [46, 47]; however, experiments showed that the viscosity of hybrid suspensions is anomalously high, exceeding enhancements in heat transfer.

Although previous work has shown that PCM suspension fluids can enhance certain thermal performance metrics, however, the effects of PCM suspensions on the local heat transfer characteristics have not been fully investigated. In particular, understanding the influence of the distribution of PCM particles inside the channel is needed for further heat transfer enhancements.

1.4 Thesis Outline

In *Chapter 1*, the motivation for studying nanostructured materials for concentrated solar power generation was discussed. State-of-the-art solar power generation technologies were discussed.

PART I: SOLID-STATE SYSTEMS

Chapter 2 investigates the design of solar thermophotovoltaics (STPVs) in the presence of spectral non-idealities and parasitic losses. The framework developed in this chapter can be used as a guide for materials selection and targeted spectral engineering depending on the concentration level and the bandgap of the photovoltaic cells.

Chapter 3 describes the development of a nanophotonic STPV device that targets the critical spectral properties in the high-concentration regime (~1000 Suns), using an array of carbon nanotubes as the absorber, and a one-dimensional photonic crystal as the emitter.

Chapter 4 describes the design of an absorber-emitter aiming to improve the conversion efficiency relative to the device from Chapter 3 at low optical concentrations (~100 Suns). To achieve the necessary spectral selectivity, a two-dimensional metal photonic crystal is developed and experimentally investigated.

PART II: THERMAL-FLUID SYSTEMS

In *Chapter 5*, a new figure of merit capturing the combined effects of thermal storage capacity, convective heat transfer characteristics and hydraulic performance of the fluids is developed to evaluate existing heat transfer fluids such as oils and molten salts as well as alternative options including water-steam mixtures (direct steam), ionic liquids/melts and suspensions of nanoparticles (nanofluids).

In *Chapter 6*, focusing of sub-micron phase change particles near a heated wall is investigated for simultaneous enhancement of local heat transfer and thermal storage capacity in solar thermal systems.

In *Chapter 7*, the main contributions of this thesis are summarized. Recommendations for future work are presented.

PART I: SOLID-STATE SYSTEMS

Chapter 2

2. The role of non-idealities in the design of solar thermophotovoltaics

Solar thermophotovoltaic power generation relies on an intermediate material, an absorber-emitter, situated between the sun and a photovoltaic cell. Ideally, this material converts the broad solar spectrum into heat, before tuning the thermal emission such that only useful radiation is delivered to the PV cell. Theoretical studies predict that solar-to-electrical efficiencies can approach 85% for STPVs [3]. Experimentally demonstrated STPVs, on the other hand, have until recently been limited to efficiencies around 1%. The large discrepancy between these two realms is in large part due to spectral non-idealities and parasitic losses.

In order to bridge the gap between theoretically suggested and experimentally demonstrated efficiencies of solar thermophotovoltaics (STPVs), this section investigates the efficiency of solar thermophotovoltaics (STPVs) in the presence of spectral non-idealities and realistic parasitic losses. A model is developed to investigate how spectral non-idealities impact the efficiency and the optimal design of STPVs over a range of PV bandgaps (0.45-0.80 eV) and optical concentrations (1-5,000 Suns). On the emitter side, we show that suppressing or recycling sub-bandgap radiation is critical. On the absorber side, the relative importance of absorptive to re-emissive spectral non-idealities depends on the energy balance. The results are well described using dimensionless parameters weighing the relative importance of non-idealities on the emitter side and the absorber side. Our framework can be used as a guide for materials selection and targeted spectral engineering in STPVs.

2.1   STPV Spectral Engineering

Spectrally-engineered surfaces can be used as both absorbers, to efficiently collect sunlight, and as emitters, to selectively emit useful radiation towards a PV cell.

The primary goal of solar absorbers is to maximize the amount of solar irradiation absorbed compared to the thermal radiation emitted in the infrared; this desirable property is known as spectral selectivity. Spectrally or wavelength selective absorbers are used in most solar thermal applications ranging from domestic hot water heating to concentrated solar power generation. The cut-off wavelength (λ_c) and the spectral properties optimize absorption (high ε_λ) of short-wavelength concentrated sunlight ($\lambda < \lambda_c$), and suppress re-emission (low ε_λ) of long-wavelength thermal radiation ($\lambda > \lambda_c$) [49]. The ideal cutoff wavelength can approximately be interpreted as the graphical intersection of the spectral solar irradiation and thermal emission (as shown in Figure 2-1), shown here for a concentration of 40 suns and a temperature of 1300 K.

In actual solar power generation devices, however, connecting solar-thermal to thermal-electrical energy conversion provides a coupling (through an energy balance at steady state) between solar concentration and the temperature of the absorber. This coupling sets a unique ideal cutoff wavelength for a given solar concentration or temperature.
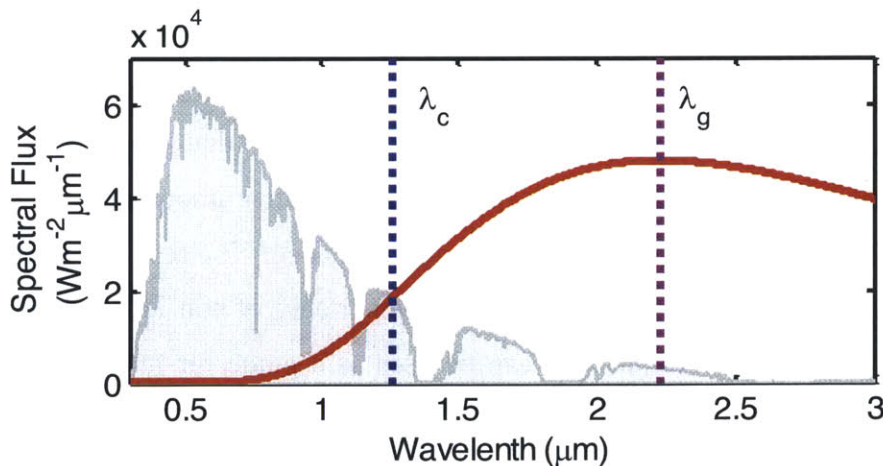
Figure 2-1 | Ideal cut-off wavelengths on the absorber-side (λ_c) and the emitter-side (λ_g).
The spectral flux for concentrated (C=40, AM1.5D) sunlight incident on the absorber and the blackbody thermal emission (T= 1300).

In STPVs, the TPV (emitter/PV) system provides the coupling and sets the temperature for a given solar input. In order to optimize the amount of useful radiation delivered to the PV, the

spectral properties of the emitter enhance thermal emission of useful radiation with energies above the PV bandgap ($\lambda < \lambda_g$) while suppressing sub-bandgap radiation ($\lambda > \lambda_g$).

Current state-of-the-art spectrally-engineered surfaces, compatible with the high operating temperatures of STPVs, have tunable cutoff wavelengths with an average emittance of ~0.80 at wavelengths below the cutoff, and ~0.20 at wavelengths above the cutoff [20, 21, 50-53]. Compared to an ideal selective surface, these properties represent approximately a 0.20 deviation (δ) from ideality. Despite their remarkable properties and tunability, this level of spectral non-ideality is insufficient for STPV power generation to reach high efficiency (*i.e.* exceeding the Shockley-Queisser limit [4] at moderate optical concentrations on the order of 1000 suns and below), as evidenced by previous experimental results and our subsequent analysis.

To achieve high efficiencies, a second level of spectral control in addition to the absorber-emitter is needed to suppress wasteful radiation from escaping the system. This second level of control comes in the form of selective windows and filters. Selective windows allow solar radiation to pass while reflecting thermal emission back to the absorber. Windows with a rugate interference coating have been demonstrated with solar-weighted transmittance exceeding 0.80 and thermal reflectance of approximately 0.50 (weighted for a 1100 °C blackbody) [54]. Similarly, sub-bandgap reflecting filters allow useful (above-bandgap radiation) to pass while reflecting sub-bandgap radiation back to the emitter. Tandem filters (interference + plasma filter) with (1300 K thermally-averaged) reflectance exceeding 0.95 below the bandgap and 0.60-0.85 transmittance above the bandgap have been demonstrated [55, 56] and are available commercially. Through a stacked configuration of spectrally-engineered surfaces surrounded by windows/filters (Figure 2-2) it is expected that non-idealities on the order of 1% are possible in the near term (at least in parts of the spectrum).
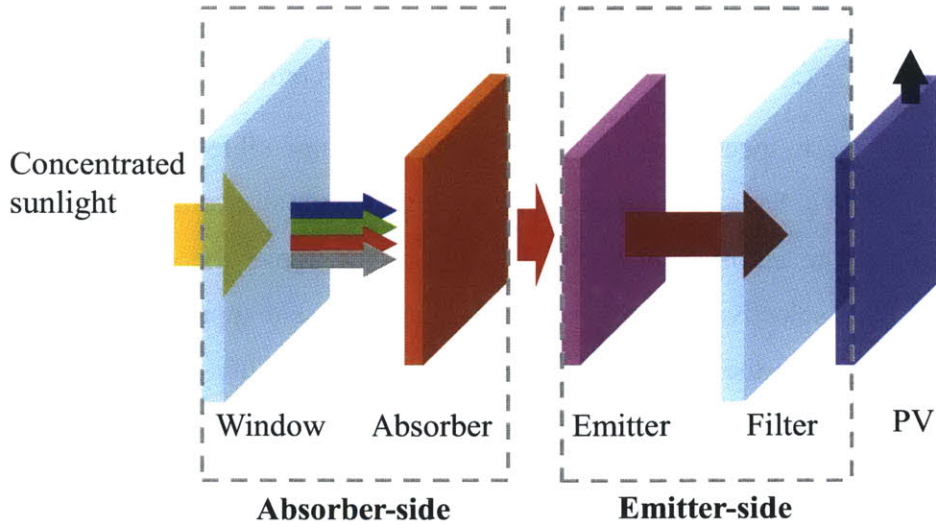
Figure 2-2 | Expanded view of STPV components.
The window and the absorber are grouped together as "absorber-side". The emitter and the filter are grouped together as "emitter-side".

Interference filters and nanophotonic surfaces allow us to engineer the properties with a certain degree of tunability and temperature-independence. However, tradeoffs between high transmittance/absorptance in one part of the spectrum and high reflectance in another part are inevitable. Therefore, uniformly decreasing the spectral non-idealities from 20% to 1%, is difficult to achieve, and it also possibly unnecessary. In practice, it is important to understand what spectral properties have the most impact in improving the efficiency of the system from its current level of non-idealities.

The goal of this section is to present a simple framework that helps determine which spectral properties are critical for improving the STPV efficiency. This framework guides us forward in determining what parts of the spectrum should be targeted using either additional components (windows/filters) or spectral engineering. Short of a global optimization ([18, 57]) coupling electromagnetic solvers for structured surfaces with a full STPV thermo-electrical model there is little guidance as to what materials or structures can be used as a starting point for the design and where our spectral engineering efforts should be directed.

This chapter aims to first understand the sensitivity of the performance and the optimal design to the non-idealities. Then, we aim to suggest physically-meaningful dimensionless quantities which can be used as weight factors or figures-of-merit to guide the materials selection and the design of nanophotonic surfaces en route to achieving high STPV efficiency.

26
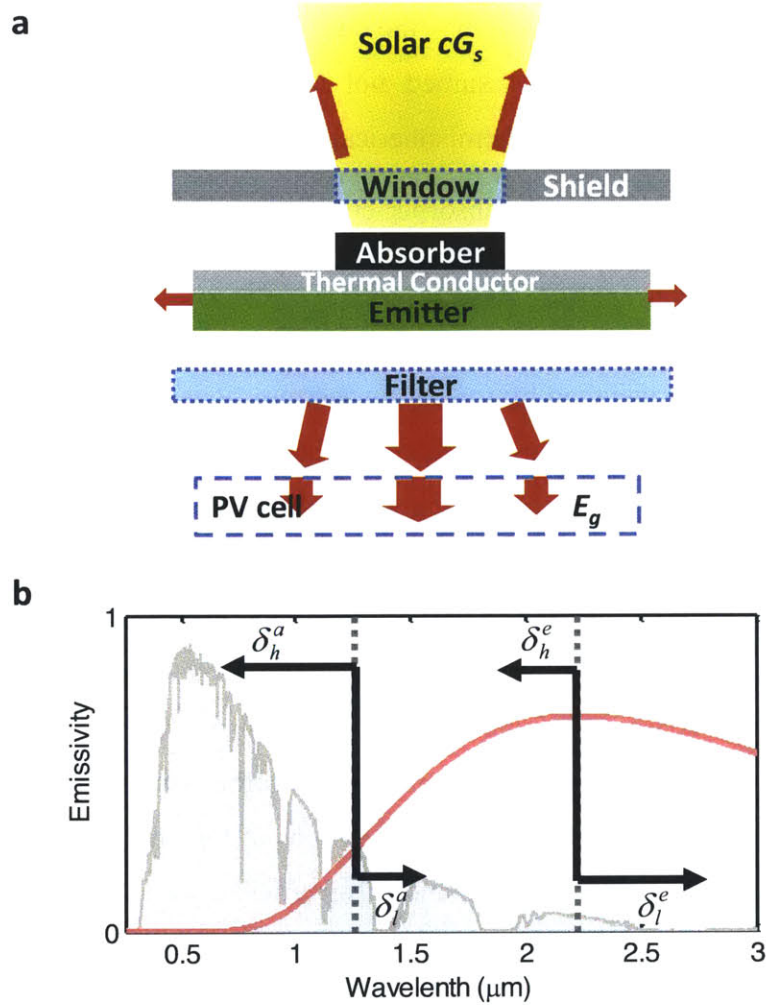
Figure 2-3 | Energy balance (a) and spectral properties (b) of an STPV with non-idealities.
The model accounts for the following STPV non-idealities: deviations from the ideal spectral properties in the absorber (δ^a) and emitter (δ^e): parasitic emissive losses from the inactive area between the absorber and emitter, and losses to the mechanical supports (5% of $Q_{E>Eg}$).

We developed a model for STPVs which closely follows the framework established by Shockley-Queisser for determining the limits of solar energy conversion with a single-junction cell. The model however accounts for the following: the actual AM 1.5D solar spectrum (appropriate for concentrated solar applications), spectral non-idealities on the absorber and emitter side, non-ideal cell behavior (non-radiative recombination), and parasitic losses through the hot inactive area and the mechanical supports. We are primarily interested in the influence of the spectral non-idealities shown in Figure 2-3b: specifically: δ_h^a – the absorber-side deviation from ideal (unity) emissivity for $\lambda < \lambda_c$ (the emissivity is $1 - \delta_h^a$ in that region), δ_l^a – the absorber-

side deviation from zero emissivity for $\lambda>\lambda_c$, δ_h^e – the emitter-side deviation from ideal emissivity above the bandgap ($\lambda<\lambda_g$), and δ_l^e – the emitter-side deviation from zero sub-bandgap emissivity ($\lambda>\lambda_g$). The emissivity is assumed not to be angularly-dependent; alternatively, spectral properties can be considered as hemispherically-averaged.

An energy balance is implemented at the absorber-emitter to determine its operating temperature:

$$2\text{-}1 \qquad \sigma(T_{ae}^4 - T_{amb}^4)(\bar{\varepsilon}_a A_a + \bar{\varepsilon}_e A_e + \bar{\varepsilon}_{na}^{eff}|A_e - A_a|) + Q_{parasitic} = \bar{\alpha}_a A_a c G_s$$

where $\bar{\alpha}$ is the absorptivity weighed by the solar spectrum, $\bar{\varepsilon}$ is the emissivity weighed by the emitted spectrum, T is the temperature of the absorber-emitter, G_s is the nominal solar flux (1000 W/m^2 = 1 sun), c is the level of optical concentration, σ is Stefan's constant, and A is the area of the component. In this formulation of the energy balance, the device is assumed to be surrounded by a blackbody maintained at 300 K. Two fundamental approximations are in fact embedded in this assumption: (i) the fraction of radiation from the absorber that reaches the sun compared to the ambient is assumed to be small (it is as high as 10.6% at C=5,000), and (ii) the impact of radiative recombination in the PV cell on the absorber-emitter temperature is neglected ($f < 1$, see below). By neglecting these two contributions to the energy balance, we are indeed slightly underestimating the STPV performance. Nevertheless, we are more interested in the relative influence of non-idealities and not the ultimate efficiency of the system.

Regarding the parasitic losses, the emissivity of the inactive area is set to δ_l of the appropriate side. For example, if the emitter is larger than the absorber ($A_e>A_a$) then $\bar{\varepsilon}_{na} = \delta_l^a$, and vice versa. The effective emissivity of the inactive area is determined by accounting for an opposing reflective shield with a reflectance of 0.96 (which is a reasonable value for a metallic mirror):

$$2\text{-}2 \qquad \bar{\varepsilon}_{na}^{eff} = \left[\frac{1}{\delta_l} + \frac{1}{(1-0.96)} - 1\right]^{-1}$$

The gap between the inactive area and the shield is assumed to be small relative to their areas such that the approximation of radiative exchange between infinite plates holds. The parasitic loss to the mechanical supports ($Q_{parasitic}$) is assumed to be 5% of thermal emission above the PV bandgap (i.e., $0.05Q_{e,E>Eg}$); this is a reasonable target for a scaled up STPV system as determined using a more rigorous model [58].

28

Once the temperature of the absorber-emitter is determined from the energy balance for a given solar input, the amount of electrical power generated by the PV cell was calculated using the approach described by Wu et al. [24]. First, the ultimate power (p_u) generated per unit area of the PV cell is determined by assuming that every photon reaching the cell with energy greater than E_g excites one electron–hole pair, extracted at E_g:

$$2\text{-}3 \qquad\qquad p_u = \int_0^{\lambda_g} \varepsilon_\lambda e_{b\lambda} \frac{\lambda}{\lambda_g} d\lambda$$

where $\lambda_g = hc/E_g$ (h is Planck's constant and c is the speed of light in vacuum) and $e_{b,\lambda}$ is the spectral emissive power. The ultimate power is then corrected by two factors: v, which accounts for the fact that the open circuit voltage (V_{oc}) is less than the bandgap voltage ($V_g=E_g/e$), and m, an impedance matching factor:

$$2\text{-}4 \qquad\qquad \upsilon = \frac{V_{oc}}{V_g} = \frac{k_b T_{PV}}{E_g} \ln\left(f \frac{R_{e,E>Eg}}{R_{PV,E>Eg}} \right)$$

where $R_{E>Eg}$ is the flux of photons with energies above the bandgap, and f accounts for non-idealities in the PV cell (non-unity absorption and non-radiative recombination). As in [24], f was set to 0.5 in our model. The impedance matching factor (m) describes the maximum output power that can be extracted from a single p-n junction cell:

$$2\text{-}5 \qquad\qquad m = \frac{z_m^2}{(1 + z_m - e^{-z_m})(z_m + \ln(1 + z_m))}$$

where z_m is determined using the following equation:

$$2\text{-}6 \qquad\qquad z_m + \ln(1 + z_m) = \frac{eV_{oc}}{k_b T_{PV}}$$

Using the above factors, the actual power generated by the PV cell is determined as $P = A_{pv} p_u m \, v$. Once the generated power is obtained, it can be normalized by the solar input power ($cG_s A_a$) to determine the overall solar-to-electrical conversion efficiency of the STPV system.

2.3 Optimization of efficiency in the presence of non-idealities

Using the model described above, this section goes on to find the optimal STPV efficiency over a range of optical concentrations (1-5,000x), and bandgaps (0.45-0.80 eV). From an engineering perspective, it is envisioned that the level of optical concentration and the choice of PV cell will likely be determined by factors such as cost, availability, system size, *etc*. Thus, these two parameters were allowed to vary. At each operating point within this concentration/bandgap space, the system design that optimized STPV efficiency was determined. Although in theory the optical concentration can exceed 45,000, we are more interested in optical concentrations practically used in terrestrial solar thermal applications (typically below 5,000). Regarding the range of bandgaps, the analysis described in this section can easily be extended to larger PV bandgaps such as that of silicon. However, considering the current level of non-idealities, reaching high efficiencies with larger bandgaps would require high levels of optical concentration which we hoped to avoid, and high temperatures which may not be realistic considering the thermal stability of nanostructured surfaces.
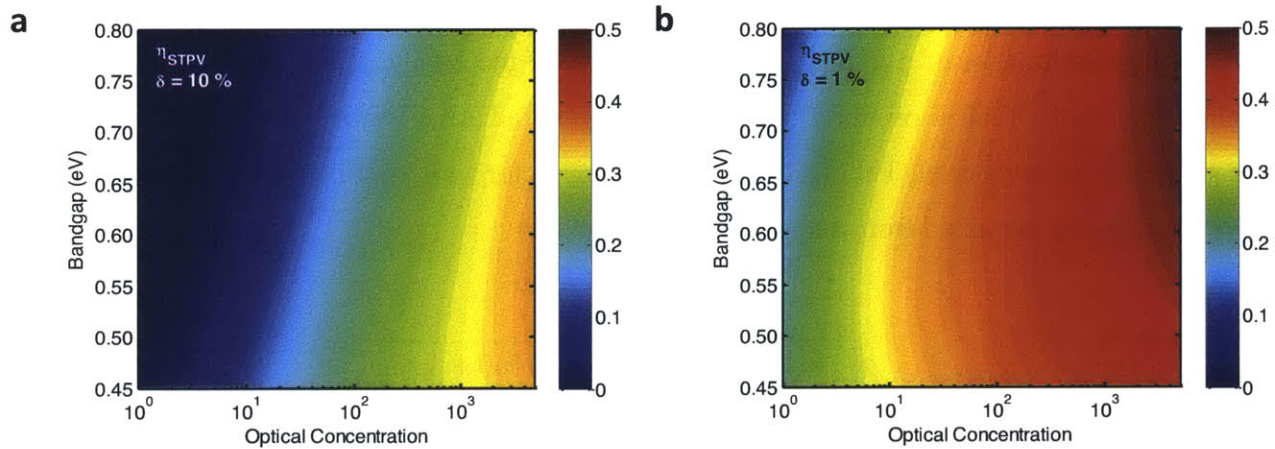
Figure 2-4 | Optimized STPV efficiency in the presence of (a) 0.10 and (b) 0.01 non-idealities (δ). Design space covers a range of bandgaps and optical concentrations

The optimal STPV efficiency for a system with 0.10 and 0.01 non-ideality (δ) is shown in Figure 2-4a and Figure 2-4b, respectively. In general, the STPV efficiency increases strongly with increasing optical concentration at a fixed bandgap. Depending on the concentration and the level of non-idealities, the efficiency typically increases with increasing bandgap up to a point (because the PV efficiency increases with the bandgap). Beyond some bandgap, the losses in the system begin to dominate and the efficiency goes back down with increasing bandgap.

The major impact of decreasing the level of non-idealities from 10% to 1% is that high STPV efficiencies become attainable at much more moderate optical concentrations (*i.e.,* >40% efficiency at 100 suns). However, to achieve 1% non-idealities, additional components such as a selective windows and filters or absorber-emitter surfaces with much better spectral control are needed. Thus, in order to maintain a high STPV efficiency there is a tradeoff between increasing complexity of the solar tracking system with increasing optical concentration, and increasing complexity of the spectrally-engineered components with decreasing optical concentration.

2.4   Impact of Non-Idealities and Parasitic Losses on the Optimal Parameters

To determine the design which maximized the overall STPV efficiency at each operating point shown above, the following the parameters were simultaneously optimized: the temperature of the absorber-emitter, the emitter-to-absorber area ratio, the absorber-side cutoff wavelength (note: the emitter-side cutoff is fixed by the bandgap of the PV). How these optimal parameters were determined, and how the level of non-idealities impacts the optimal parameters within the considered design space will discussed in more detail in the following sub-sections.

2.4.1   Cutoff wavelength optimization

A cutoff wavelength is where the absorber-side properties transition from high emissivity at shorter wavelengths, needed to absorb and thermalize sunlight, to low emissivity at longer wavelengths, needed to suppress thermal re-emission from the absorber. The "location" of the cutoff wavelength on the absorber-side maximizes the amount of solar energy collected as heat. Despite the fact that they are separated by a vacuum gap, we can consider the window and the absorber as part of one absorber-side unit whose goal it is to create this spectral selectivity (*i.e.* allow sunlight to get absorbed while suppressing thermal emission from leaving the unit).

In the simple case where the solar spectrum is approximated by a blackbody at 5800 K and the selective surface transitions from ideal absorptance to zero emittance, the cutoff wavelength is defined by the intersection of the two curves: the incident spectral flux (set by the optical concentration) and the thermal emissive flux outgoing from the surface (set by the temperature). Here we consider a slightly more complex case where the actual solar spectrum that reaches the absorber in concentrated solar thermal systems (AM 1.5D) is used, and non-idealities are introduced above and below the cutoff. The net spectral flux (solar incoming minus thermal outgoing) is shown in Figure 2-5a. Because of the discrete nature of the AM 1.5D spectrum,

31

multiple wavelengths could exists where the net flux is zero, meaning the thermal flux (Q_λ) equals the solar flux (H_λ). Nevertheless, there is typically only one cutoff wavelength that maximizes the amount of heat collected by the absorber-side. This cutoff is more rigorously determined by integrating the net spectral flux up to a given wavelength, as shown in Figure 2-5b. The ideal cutoff wavelength corresponds to the maximum point along this curve.
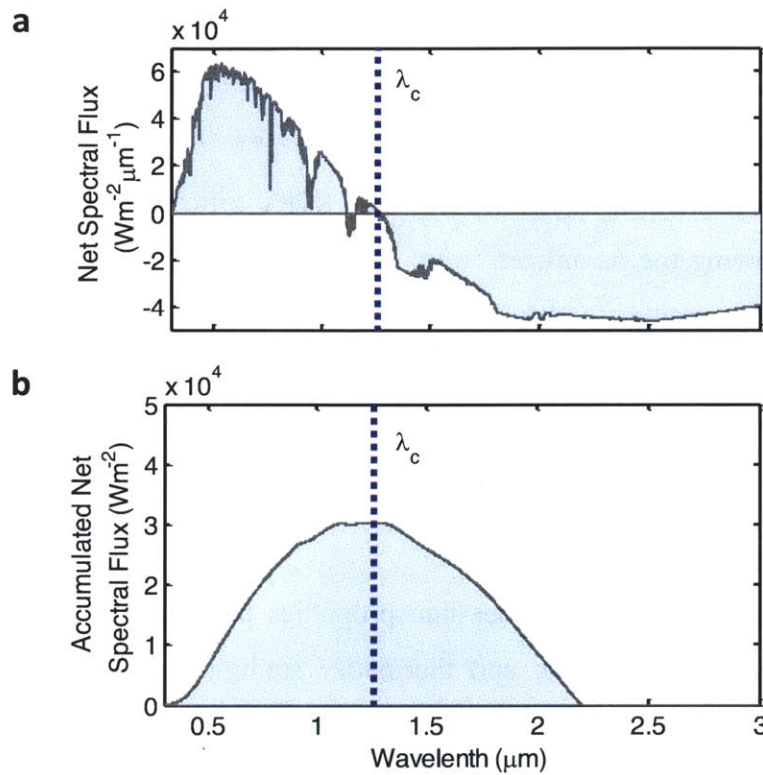
Figure 2-5 | Optimization of absorber-side cut-off wavelength.
Net spectral flux (a) integrated up a wavelength of interest (b) showing optimum cutoff wavelength.

Even though we have determined the cutoff wavelength by assuming ideal absorptance at wavelengths below the cutoff and zero emittance above the cutoff, the methodology is general. The assumption of ideality allowed us to represent the accumulated net flux (or heat collected) with a simple integral of H_λ -Q_λ up to the wavelength of interest:

2-7
$$\int_0^\lambda H_{\lambda'} - Q_\lambda \cdot d\lambda'$$

The question naturally arises whether or not this cutoff wavelength optimizes the collected sunlight when spectral non-idealities are introduced. It can be mathematically shown that by

32

introducing spectral non-idealities, the new function to be optimized is a scaled and vertically translated version of the original accumulation function, taking on the following form:

$$2\text{-}8 \qquad C_1\left(\int_0^\lambda H_{\lambda'} - Q_{\lambda'} d\lambda'\right) + C_2$$

where C_1 and C_2 are wavelength-independent constants:

$$2\text{-}9 \qquad C_1 = 1 - \delta_l^a - \delta_h^a \qquad\text{(a)}$$

$$C_2 = \delta_l^a\left[cG_s - \sigma(T_{ae}^4 - T_{amb}^4)\right] \qquad\text{(b)}$$

Therefore, as long as the emittance below the cutoff is bigger than the emittance above the cutoff (and the cutoff is perfectly sharp), the cutoff wavelength determined using the accumulation methodology is universal.

The only parameters determining the optimal cutoff wavelength are the optical concentration and the temperature of the absorber, and of course, the solar spectrum of interest. In the case of AM1.5 there are specific bands of sunlight that are attenuated due to atmospheric absorption. These spectral features lead to clustering of the cutoff wavelengths at the high-energy edge of the atmospheric bands, as shown in Figure 2-6. From the median of each cluster, we can determine the three most prevalent cutoff wavelengths: 1.33 μm, 1.78 μm and 2.40 μm.

33
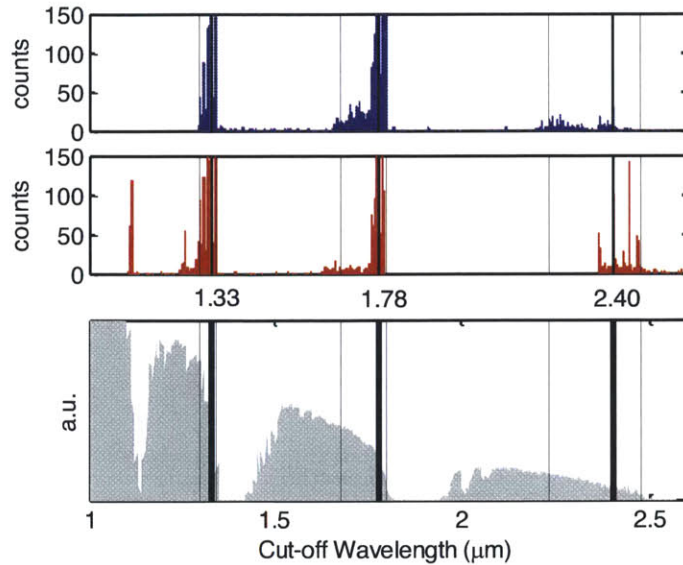
Figure 2-6 | Clustering of absorber-side cut-off wavelengths.
These are the optimal cutoff wavelengths corresponding to Figure 2-4. Dark lines represent the median cutoff wavelength within each cluster and the dashed lines represent the 5% and 95% percentile. Red and blue clusters represent 10% and 1% non-ideality cases, respectively.

Figure 2-7 shows the ideal cutoff wavelengths that optimize the STPV efficiencies shown in Figure 2-4. Each of the three prevalent cutoff wavelengths (short, medium and long) is best suited for a band of operating points. In general, the ideal cutoff wavelength increases with increasing optical concentration to allow more of the solar flux to be absorbed. Below ~10 suns in the 10% non-ideality case, however, the ideal cutoff wavelength increases with decreasing optical concentration because the design cannot reach high enough temperatures for efficient operation (this will be discussed in more detail when considering the optimal temperature). This regime however is not of practical interest since the efficiency is low.
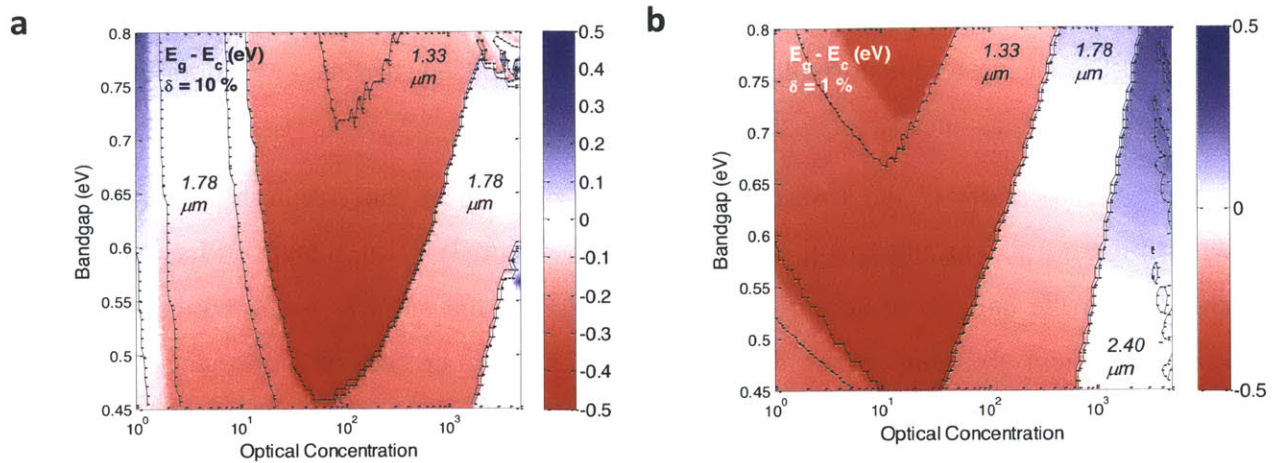
Figure 2-7 | Optimal absorber-side cut-off wavelength.
Note: the emitter-side cutoff is set to the bandgap energy.

By comparing Figure 2-7a and b, we observe that the optimal cutoff wavelength is shifted to the left by decreasing the non-idealities to 1%. This trend of shifting to the left with a reduction of non-idealities mirrors the behavior of the efficiency.

Figure 2-7 also shows the bandgap energy (E_g) relative to the cutoff energy (E_c). *Red* corresponds to regions where the bandgap is red-shifted relative to the cutoff energy. In contrast, *blue* corresponds to regions where the bandgap is blue-shifted relative to the cutoff energy. The latter does not imply energy up-conversion because the mean energy of the solar irradiation is still higher than the mean energy of the thermal emission. Nevertheless, this analysis can be extended to higher bandgap PV cells to investigate realistic regions where thermally-driven energy up-conversion is achievable [59]. The white regions are also interesting because the cutoff energy matches the bandgap energy, meaning that the absorber-side spectral design can potentially double as the emitter-side spectral design. In essence, one spectral control strategy can realistically serve two purposes.

2.4.2 Temperature optimization

The temperature of the absorber-emitter is an important parameter because it has strong implications for both the efficiency and the practicality of an STPV system. The temperature plays a major role in the choice of material, the type of surface structuring used for spectral control, the thermal stability of the device, and the device lifetime. It also determines the strength of energy modes excited above the bandgap of the PV and hence the power density of the

generator. The power density is an important consideration in the thermo-economic analysis since the cost of the system is normalized by the power produced. It is also an important metric in portable applications because of space/weight constraints.

The optimal temperature of the absorber-emitter as a function of concentration and bandgap is shown in Figure 2-8. The ideal temperature for the case with 10% non-idealities has a stronger dependence on the concentration and the PV bandgap. As the spectral performance improves (1% non-idealities), the temperature dependence of the absorber and TPV efficiency is not as strong. This leads to a more uniform optimal temperature distribution across the design space of consideration.
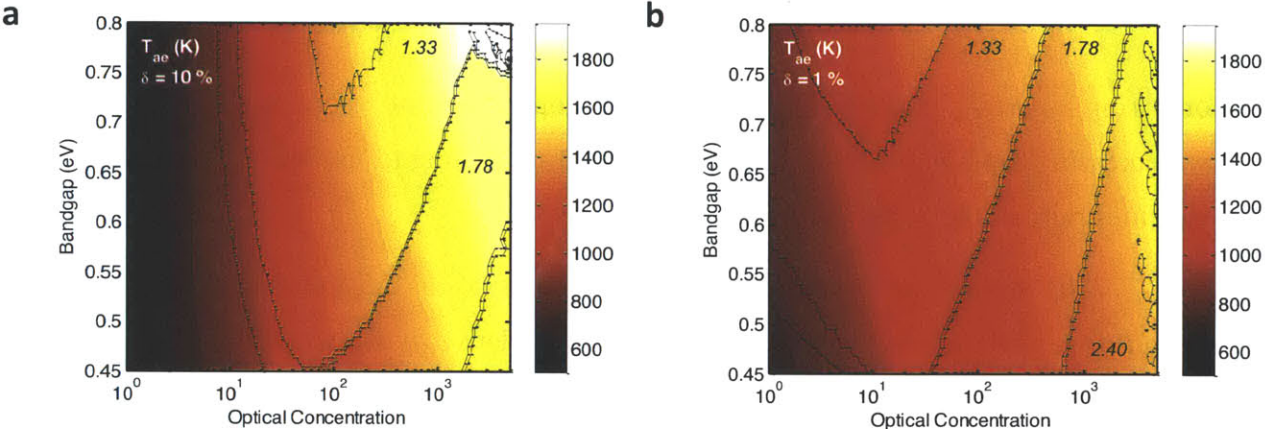
Figure 2-8 | Optimal temperature of the absorber-emitter.

It is also noticeable that in the areas where the cutoff wavelength bands meet there are discontinuities in the optimal temperature. For example, two points that close in parametric space might see a shift from a medium cutoff (1.78 μm) to a longer cutoff wavelength (2.40 μm) accompanied by a 50-100 K drop in optimal temperature.

Finally, it is also observed that at concentrations lower than ~50 suns in the 10% case, and ~10 suns in the 1% case, the optimal temperature drops off more quickly. This regime is characterized by low efficiency, since the optical concentration is insufficient to bring the emitter to reasonable temperatures for efficient power generation.

2.4.3 Geometric (area ratio) optimization

Geometrical parameters, such as the size of the emitter relative to the absorber, can be used to achieve optimal performance at a specific solar irradiance or optical concentration. With unconcentrated or low optically-concentrated solar radiation, thermal concentration [60, 61] boosts the hot-side temperature, enabled by low-emittance spectrally-selective surfaces. When high optically-concentrated solar radiation is available, high conversion efficiency is achieved through thermal spreading (high emitter-to-absorber area ratios [58]) enabled by high-absorptance surfaces. Both strategies have been experimentally implemented to achieve substantial improvements (3-8x) [58, 60] in conversion efficiency compared to prior solar-heated thermoelectric [62] (TE) and thermophotovoltaic [13] (TPV) generators.

Here we consider more generally the emitter-to-absorber area ratio (AR) as a free parameter used for optimization of the overall STPV performance. The low AR and high AR envisioned devices are shown Figure 2-9. As mentioned in the model, a reflecting radiation shield is used to limit the losses from the mismatched areas.
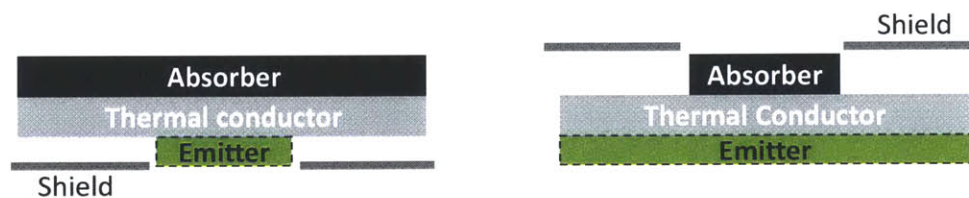
Figure 2-9 | Geometrical optimization of the size of emitter with respect to the absorber (AR).
a. Emitter is smaller than the absorber, thus $AR<1$, b. Emitter is larger than the absorber, this $AR>1$.

The optimal area ratio as a function of optical concentration and bandgap is shown in Figure 2-10. In general, the optimal AR increases with concentration. As with the temperature, the gradients in optimal AR are steeper when the level of non-idealities is higher. To achieve high efficiencies with 10% non-idealities, the area ratio climbs to almost 100 at high optical concentrations (above 1000x). Reducing the size of the absorber decreases the area for re-emissive thermal losses and increases the efficiency of solar collection. The high concentration regime pushes the cutoff absorber-side wavelength to longer wavelengths such that it coincides or surpasses the PV bandgap and the emitter-side spectral cutoff (*i.e.,* the blue-shifted regime in Figure 2-7). However, the high area ratio regime requires higher levels of optical concentration

and effective thermal spreading between the absorber and the emitter to maintain near-isothermal operation.
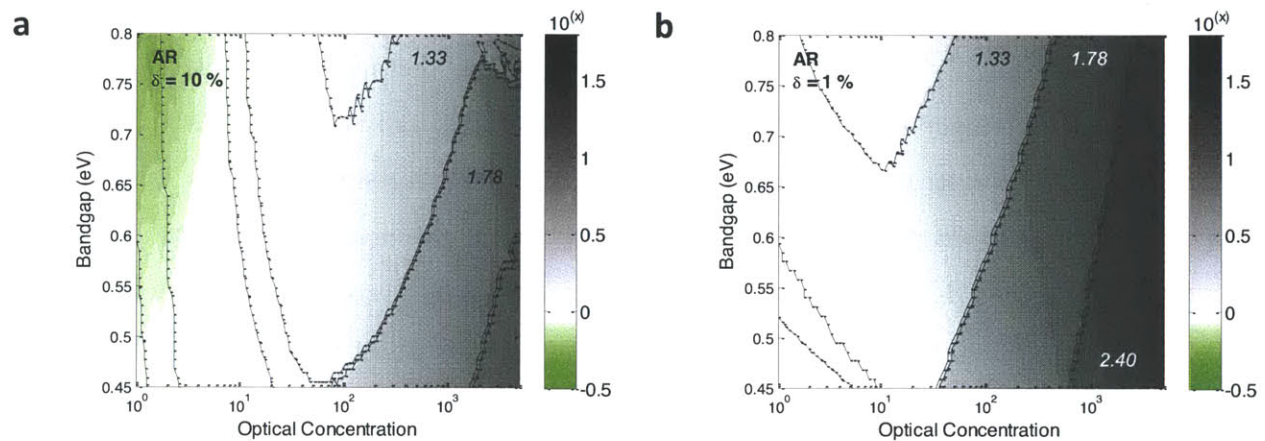
Figure 2-10 | Optimal absorber-emitter geometry (emitter-to-absorber size, *AR*).
Optimal AR for an STPV with (a) 10% non-idealities, compared to an STPV with (b) 1% non-idealities.

There is also a regime where thermal concentration is optimal, albeit with low efficiency. The issue with relying on thermal concentration to achieve these high operating temperatures is that the emissive losses from the large absorber area begin to dominate. Additionally, the parasitic losses from the inactive areas contribute to making efficient thermal concentration difficult to achieve without exceptionally low levels of spectral non-idealities. This effect was previously observed by Bermel *et al.* [63], hence, in addition to wavelength selectivity, angular selectivity was suggested to enable use of unconcentrated sunlight.

2.5   Relative importance of Emitter-side Non-Idealities

Thus far, we have explored the impact of uniformly improving the spectral performance from 10% to 1% non-idealities on the efficiency at moderate optical concentrations, as well as the optimal temperature, cutoff wavelength and area ratio.

Instead of uniformly decreasing the non-idealities on the emitter side, we consider the impact of independently increasing the above-bandgap emittance ($1-\delta_h^e$) from 0.90 to 0.99 and decreasing the emittance below the bandgap (δ_l^e) from 0.10 to 0.01 (see Figure 2-11a). Figure 2-11b shows the boost in efficiency at a specific bandgap (0.55 eV) for each of the spectral improvements. Increasing the above-bandgap emittance has a relatively negligible effect on the efficiency. On the other hand, decreasing the below-bandgap emittance increases the efficiency significantly; a

0.09 decrease in emittance improves the efficiency by as much as 200% at low optical concentrations, and by approximately 15% at high optical concentrations.
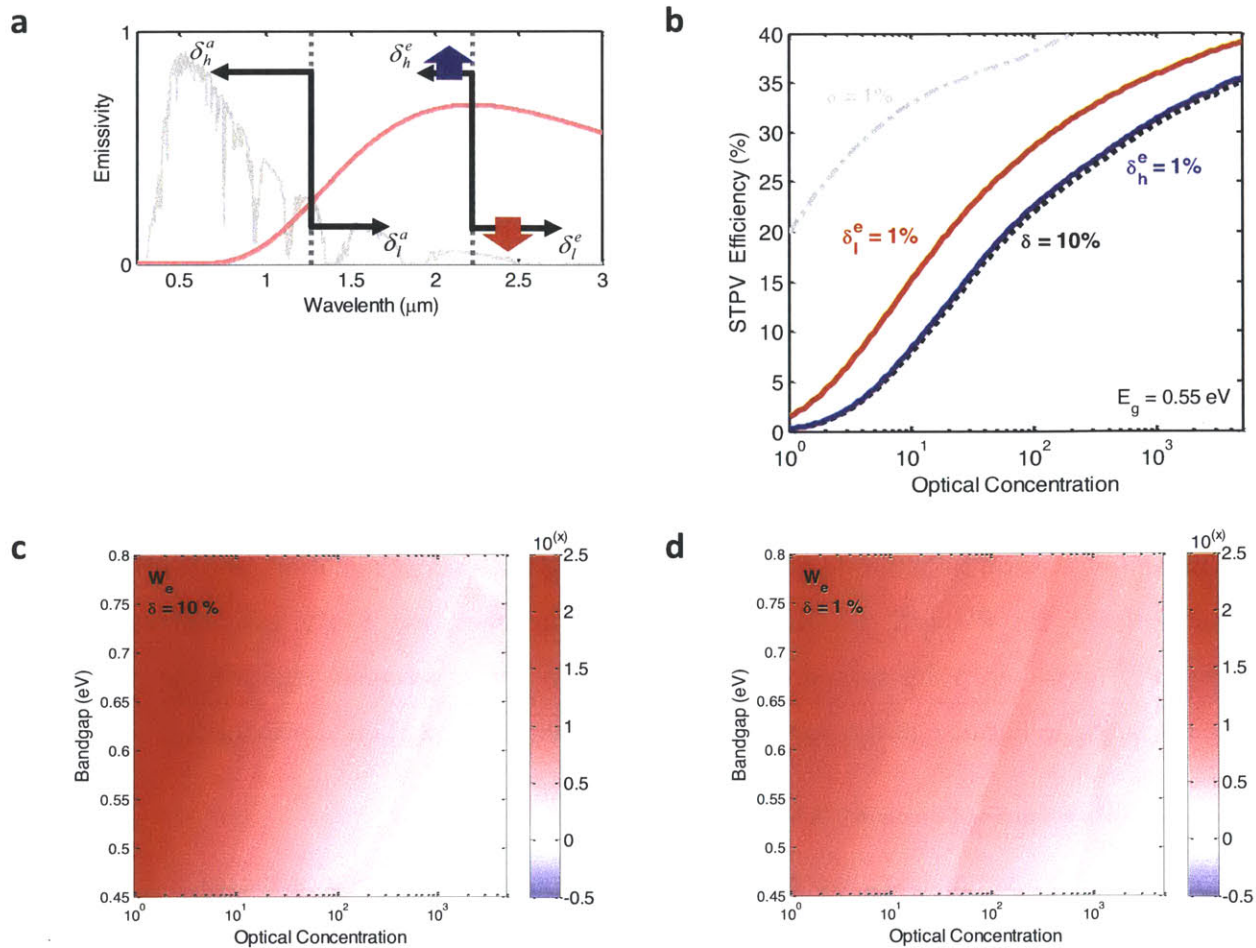
Figure 2-11 | Relative importance of high above-bandgap vs. low below-bandgap emittance.

To understand why decreasing the below-bandgap emittance has a much stronger impact on the efficiency, we compare the emissive power below and above the bandgap at the optimal operating point. This ratio is termed the emitter-side weighing parameter (W_e):

$$2\text{-}10 \qquad\qquad W_e = \frac{e_{E<E_g}}{e_{E>E_g}}$$

where e is the emissive power within the range specified by the subscript. As shown Figure 2-11c-d, W_e is much greater than one, over the entire range considered. This implies that the

emissive power below the bandgap is much greater than above the bandgap, by as much as one or two orders of magnitude depending on the operating point. The emissive power is greater below the bandgap for the following reasons: i) when the bandgap wavelength coincides with the peak blackbody wavelength, the shape of Planck's distribution dictates that roughly ~75% of the energy is below the bandgap, ii) increasing the temperature is detrimental to the absorber efficiency and shifts the emitted power content away from the bandgap, where the spectral response is lower. For these reasons, the power content below the bandgap is high and any deviation from ideality results in a large direct loss. This observation explains why the efficiency is drastically improved when the emittance below the bandgap is decreased.

The fact that W_e is still high at 1% uniform non-ideality (Figure 2-11d) means that efforts should be focused on suppressing or recycling sub-bandgap radiation even further. Thus, in addition to having a low emittance substrate as the emitter, the following components will be beneficial: a filter that allows useful radiation to pass while reflecting low-energy radiation, and a reflector on the backside of the PV cell. By using all three approaches, the STPV efficiencies can be significantly improved. Care should of course be taken not to seriously degrade the emittance above the bandgap because of the power density considerations mentioned previously.

2.6   Relative importance of Absorber-side Non-Idealities

Similarly to the above analysis, we can consider the relative importance of increasing the solar absorptance (at wavelengths below the cutoff wavelength) to that of decreasing the thermal emittance (at wavelengths above the cutoff wavelength). Figure 2-12b shows the increase in efficiency when the emittance below the cutoff wavelength ($1-\delta_h^a$) is independently increased from 0.90 to 0.99 (in *blue*), and when the emittance above the cutoff wavelength (δ_l^a) is independently decreased from 0.10 to 0.01 (in *red*). The improvement in efficiency can be as high as 5-10 absolute percentage points due to each of the spectral improvements, depending on the optical concentration and the operating regime.
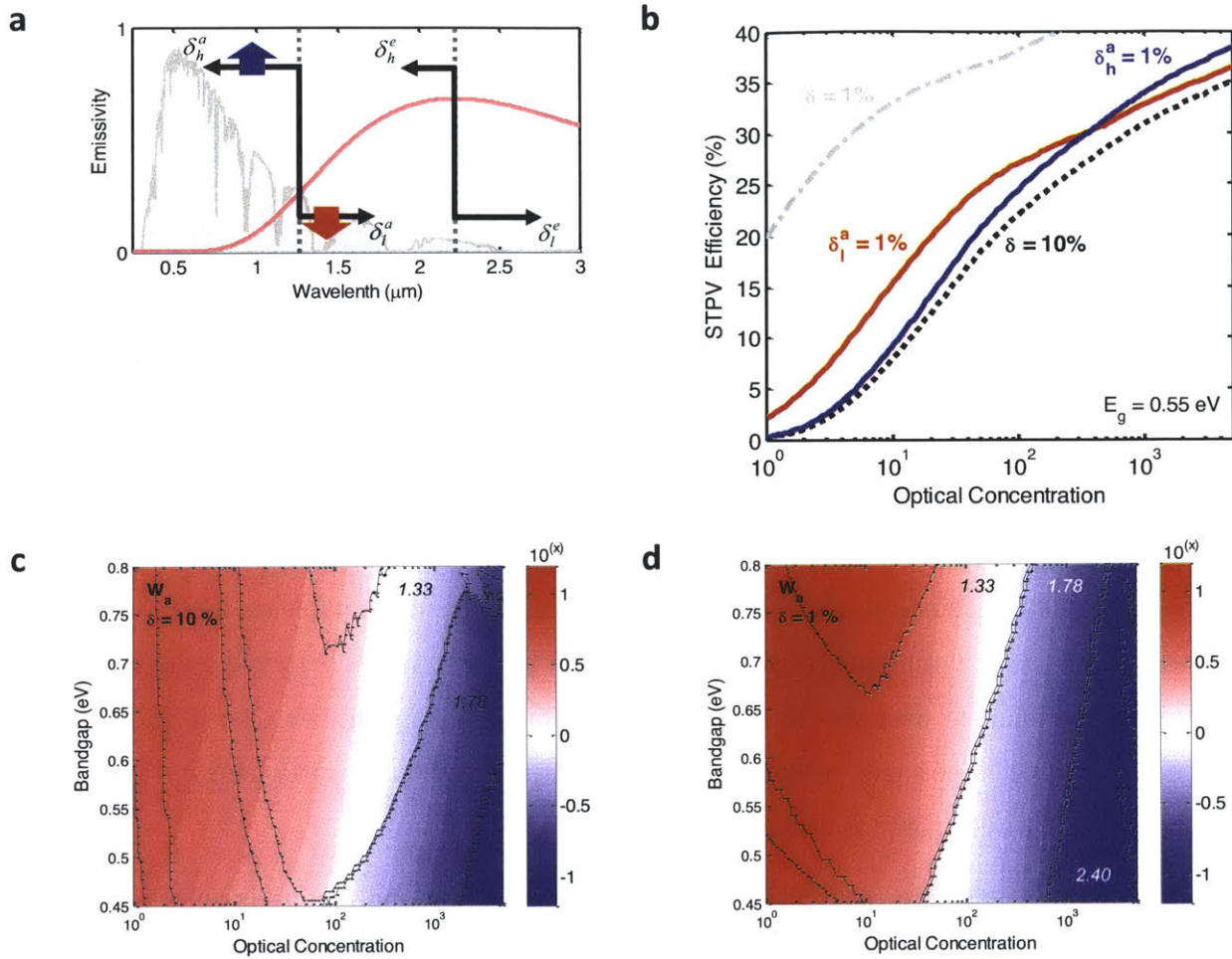
Figure 2-12 | Relative importance of high solar absorptance vs. low thermal emittance in the absorber

To understand why there is a cross-over point between the importance of high absorptance versus low emittance on the absorber-side, we compare the incident solar flux (cG_s) to the emissive flux (σT^4). This ratio is termed the absorber-side weighing parameter (W_a):

$$2\text{-}11 \qquad\qquad W_a = \frac{\sigma(T_{ae}^{\ 4} - T_{amb}^4)}{cG_s}$$

Figure 2-12c,d show the W_a at the optimal design. There is indeed a regime where $W_a < 1$ and the incident solar flux dominates (in *blue*), and a regime where $W_a > 1$ and the emissive flux dominates (in *red*). If the solar flux dominates then increasing the absorptance below the cutoff wavelength is beneficial; on the other hand, if the emissive flux dominates, then decreasing the

41

emittance above the cutoff wavelength is expected to be more beneficial. The absorber-side weighing parameter explains why we observe the cross-over behavior in efficiency and why there are two distinct regions: a low W_a ratio regime where high absorptance is more important and a high W_a regime where low emittance is more important.

It is interesting to note that W_a can be obtained by re-arranging the energy balance (Equation 2-1) on the absorber-emitter:

$$
2\text{-}12 \qquad W_a = \frac{\sigma(T_{ae}{}^4 - T_{amb}{}^4)}{cG_s} = \frac{\bar{\alpha}_{abs}A_{abs}}{\bar{\varepsilon}_{abs}A_{abs} + \bar{\varepsilon}_{emit}A_{emit} + parasitic}
$$

$$
= \frac{\bar{\alpha}_{abs}}{\bar{\varepsilon}_{abs} + \bar{\varepsilon}_{emit} \cdot AR + parasitic}
$$

After re-arranging the equation, we observe that the area ratio and the parasitic losses appear in the denominator. Thus, with increasing area ratio and/or parasitic losses we expect the solar flux to increase and dominate over the thermal emission. This explains why we observe a coupling between the relative importance of spectral non-idealities and the area ratio, and by extension, the optimal cutoff wavelength (as previously mentioned).

This information is valuable as a guide for spectral engineering and materials selection. Even within each band of cutoff wavelengths there could be a subtle transition from $W_a > 1$ to $W_a < 1$ meaning that the cutoff wavelength does not fully specify which selective surface is best suited for a particular operating point. For example, two surfaces that have the same cutoff wavelength but different absorptance/emittance values might perform better under distinct operating conditions.

In the subsequent chapters, we explore the design of a device that is best-suited for the high optical concentration regime where high broad-band absorptance is important (Chapter 3), and a device that is best-suited for a moderate optical concentration regime where both high absorptance below the cutoff and low emittance above the cutoff are important (Chapter 4).

2.7   Summary

This chapter investigated the design of solar thermophotovoltaics (STPVs) in the presence of spectral non-idealities and parasitic losses. The detailed-balance approach was modified to

account for the actual AM 1.5D solar spectrum, spectral non-idealities, and parasitic losses. This model was used to maximize the STPV efficiency over a range of PV bandgaps (0.45-0.80 eV) and optical concentrations (1-5,000 Suns) by determining the optimal temperature, emitter-to-absorber area ratio (AR) and absorber cutoff wavelength at each operating point. The impact of non-idealities on the efficiency and the optimal parameters was investigated. The results are explained using dimensionless parameters weighing the relative importance of non-idealities on the emitter-side and the absorber-side. On the emitter-side, we show that emissive power below the bandgap dominates ($W_e > 1$) such that suppressing or recycling sub-bandgap radiation is critical. On the absorber side, the relative strength of thermal emissive power to solar irradiance (W_a) depends on the operating regime, and so does the importance of re-emissive to absorptive spectral non-idealities. Due to the atmospheric absorption bands in the AM 1.5D spectrum there are three prevalent absorber-side cutoff wavelengths, each of them coupled to a specific regime: 1.33 μm ($AR \approx 1$, $W_a \approx 0.1$-1), 1.78 μm ($AR \approx 1$-10, $W_a \approx 1$-10) and 2.40 μm ($AR \approx 10$-100, $W_a \approx 10$-100). These dimensionless parameters can be used to construct a physically meaningful figure of merit when calculating the optimal surface nanostructure using an E-M solver without resorting to a full STPV system-level calculation. In general, the framework developed in this chapter can be used as a guide for materials selection and targeted spectral engineering in STPVs.

Chapter 3

3. High optical concentration regime: Targeting critical spectral properties

The high temperature operation of the emitter poses two key challenges to efficient STPV power conversion: collecting sunlight to efficiently reach T_e^{opt}, and maintaining spectral selectivity at elevated temperatures. Past STPV embodiments have relied on the intrinsic properties of materials such as tungsten [13, 14]. Ultimately, the reliance on the intrinsic spectral properties of materials for the absorber-emitter has limited previously reported experimental STPVs to conversion efficiencies around 1% [13-15].

Here we report on a full solar thermophotovoltaic device which, thanks to the nanophotonic properties of the absorber-emitter surface, reaches experimental efficiencies of 3.2%. The device integrates a multi-wall carbon nanotube absorber and a one-dimensional Si/SiO$_2$ photonic crystal emitter on the same substrate, with the absorber-emitter areas optimized to tune the energy balance. Our device is planar and compact and could become a viable option for high-performance solar thermophotovoltaic energy conversion.

3.1 Device Design and Fabrication

We varied the emitter-to-absorber area ratio ($AR=A_e/A_a$) from 1 to 10 to achieve optimal performance. With increasing area ratio, we supply enough heat for the absorber-emitter to reach T_e^{opt} by increasing the level of irradiance and leveraging the high absorptance of the nanotube array. Thermal resistance between the absorber and emitter is minimized by integrating the absorber and emitter on the same conductive silicon substrate such that heat is effectively delivered to the emitter via thermal spreading. Since the absorber area is reduced with respect to the planar area of the sample (Figure 3-1c), the area for re-emissive losses from the nearly-blackbody nanotube array surface is decreased, thus boosting thermal efficiency. To reduce parasitic radiative losses, we metallized the sides of the silicon substrate and inactive area around the nanotube absorber with W, a relatively low-emissivity high-temperature material, and incorporated a high-reflectivity Ag-coated shield (Figure 3-1a) to recycle this parasitic radiation back to the device.
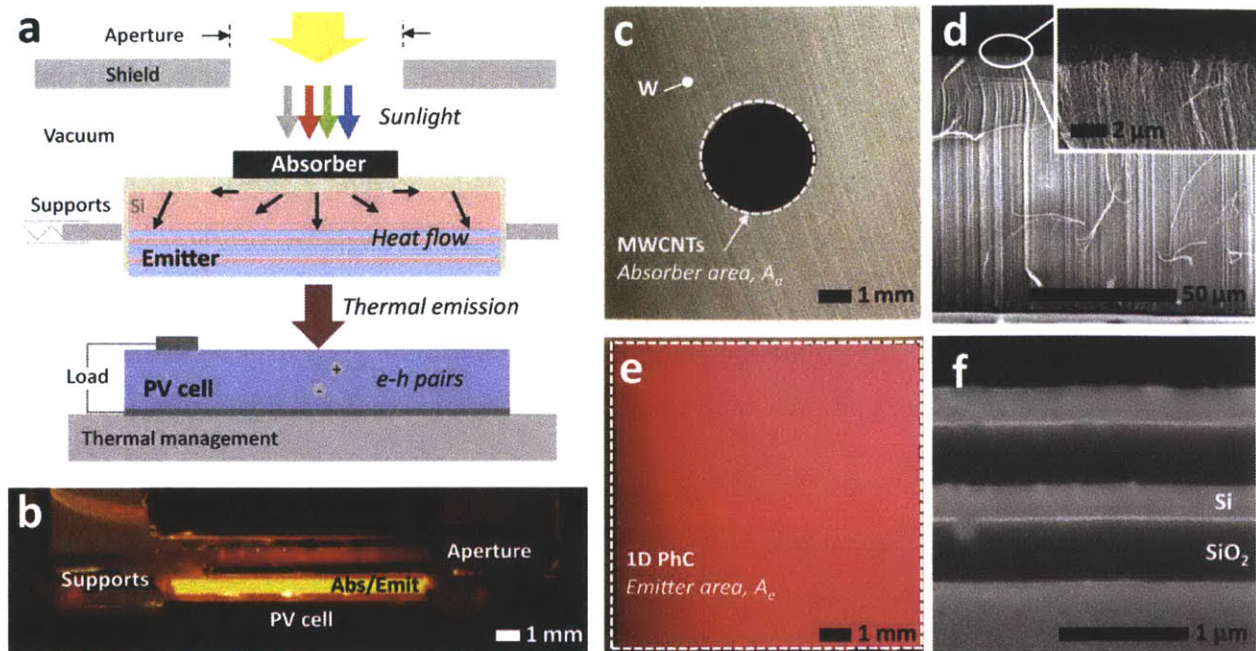
Figure 3-1 | Operating principle and components of the nanophotonic, area ratio optimized (NARO) STPV.
Sunlight is converted to useful thermal emission, and ultimately electrical power, via a hot absorber-emitter. (a) Schematic and (b) optical image of our vacuum-enclosed devices composed of an aperture/radiation-shield, a array of multi-walled carbon nanotubes (MWCNT) as the absorber, a one-dimensional Si/SiO$_2$ photonic crystal emitter (1D PhC), a 0.55 eV bandgap PV cell (InGaAsSb), and a chilled water cooling system. c, Absorber-side optical image of an $AR(=A_e/A_a)=10$ module showing spatially-defined MWCNTs (A_a=0.1 cm^2) on a W-coated Si substrate (1x1 cm planar area, 550 μm thick). d, SEM cross-section of the MWCNTs (inset: magnified view of the nanotube tips). e, Optical image of the 1D PhC emitter (A_e=1 cm^2). f, SEM cross-section of the 1D PhC showing the alternating layers of Si and SiO$_2$.

The absorber-emitter module was composed of an array of multi-wall carbon nanotubes as the solar absorber and a one-dimensional Si/SiO$_2$ photonic crystal as the selective emitter.

3.1.1 Absorber

Vertically-aligned carbon nanotubes were chosen as the solar absorber due to their high-temperature stability in vacuum and their nearly ideal absorptance, crucial for absorbing highly-concentrated irradiance at elevated emitter-to-absorber area ratios. As shown in Figure 3-1d, the as-grown nanotubes are 10-15 nm in outer diameter and 80-100 μm tall with a ~0.5 μm variation in height at the tips. The broad-spectrum absorptance of the nanotube array in this study exceeds 0.99, consistent with previous reports for similar nanotube array geometries [64-66].

The radiative properties of the MWCNT absorbers were characterized across a broad range of wavelengths (Figure 3-2). Total reflectance (diffuse + specular) was gathered between 250 and

47

1750 nm using a UV-Vis-NIR spectrophotometer (*500i, Cary*) with a diffuse reflectance accessory. The baseline reference measurement was performed with a certified reflectance standard (*SRS-99-010, Labsphere*). The MWCNT surface was further characterized in the infrared region (2.8-10 μm) using a FT-IR (*Spectrum ONE, Perkin Elmer*). During these measurements, specular reflectance was measured at an incidence angle of 30 degrees using a variable angle specular reflection accessory (*VeeMax II*). Both characterizations support previously reported broadband emittance measurements exceeding 0.99 [64-66]. Significant variations in emittance before and after high-temperature operation and amongst samples (*AR*=1 to 10) were not observed.
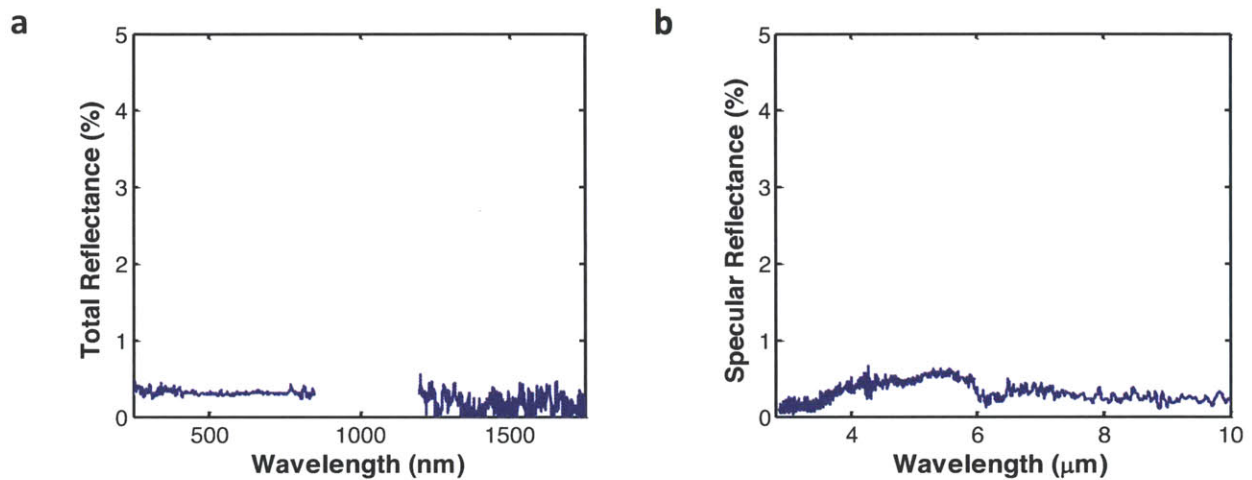
Figure 3-2 | Optical characterization of MWCNT absorber.
a, Total reflectance (diffuse + specular) spanning the relevant solar wavelength range (0.25-1.75 μm); data near 1 μm omitted due to high noise level associated with lamp/detector change. b, Specular reflectance (30° incident angle) in the infrared (2.8-10 μm).
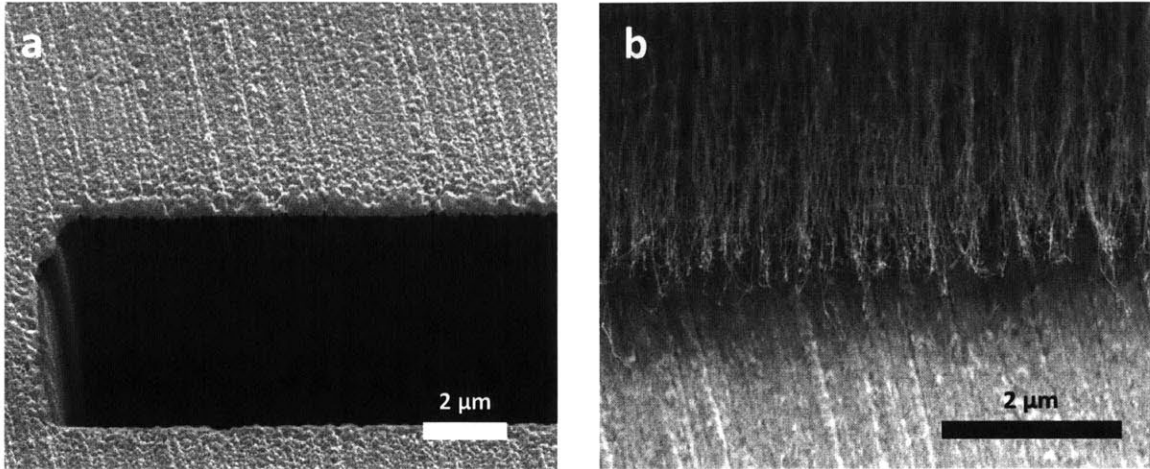
Figure 3-3 | SEMs of absorber-side interfaces.
a, W/substrate and b, CNT/W.

The above figure shows the W/substrate and CNT/W absorber-side interfaces. These SEMs were taken on a sample after approximately 1 hr of high-temperature operation (1000-1300 K). The micro/nanoscale morphologies of the interfaces between the different materials are clearly distinguishable in the SEMs.

3.1.2   Emitter

The multilayer Si/SiO$_2$ structure of the photonic crystal, composed of five alternating layers of Si and SiO$_2$, improves the spectral matching between the emittance of the emitter and the internal quantum efficiency of the InGaAsSb PV cell [67-69] (E_g=0.55 eV). These materials were chosen for ease of fabrication and high-temperature compatibility with the silicon substrate. The layer thicknesses were optimized via a constrained global optimization of the product of efficiency and power density [7].
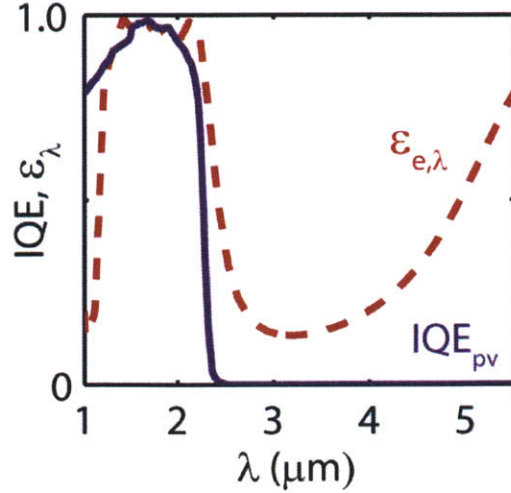
Figure 3-4 | Emitter and PV cell spectral properties.
Measured spectral emittance of the 1D PhC at 1285 K and the internal quantum efficiency of the PV used by the SQ1DD model.

3.2   Modeling

We have developed a system level model to predict both input and output power to the device for a given equilibrium temperature. Our assumption of isothermal operation (quasi 1-D) is justified due to the geometry of the planar absorber/emitter device as well as its relatively high thermal conductivity (as supported by a highly-fidelity 2-D model [57, 70]). When an equilibrium temperature is specified, heat transfer (radiation and conduction) with the surrounding components (PV cell, shield, supports, and vacuum chamber) can be determined. Radiative transfer is solved on a spectral basis through an energy balance at each surface. The spectral radiosity (J_λ) is the sum of the thermal emission ($E_{b\lambda}$) and the reflection of the irradiance (H_λ). The irradiance is defined as the portion of the radiosity from other surfaces (j) in the network which is intercepted by the surface of interest (i). The intercepted portion is determined using diffuse view factors (F_{ij}).

3-1
$$J_{\lambda_i} = \varepsilon_{\lambda_i} E_{b\lambda_i} + (1 - \varepsilon_{\lambda_i}) H_{\lambda_i}$$

3-2
$$H_{\lambda_i} = \sum_{j=1}^{n} J_{\lambda_j} F_{ij}$$

Equations 3-1 and 3-2 are solved for each surface at each wavelength. After integrating over all wavelengths, the total radiative heat transfer to each component is known.

Conduction from the supports is estimated using a fin approximation. This is justified by a small Biot number (<<0.1). For a fin with an adiabatic tip, the heat loss is given by the following equation:

3-3 $$\dot{q}_{fin} = (T_b - T_v)\sqrt{\bar{h}\,P\,k\,A_c}\,\tanh(mL)$$

where T_b is the temperature at the contact between the absorber-emitter and the support, T_v is the temperature of the vacuum chamber, $\bar{h}$ is the average heat transfer coefficient (approximated using a linearized radiation coefficient), P is the perimeter, k is the thermal conductivity, A_c is the cross-sectional area, and L is the length of the support. The fin constant (mL) is given by:

3-4 $$mL = \sqrt{\frac{P\,\bar{h}}{k\,A_c}}\,L$$

The emittance and the thermal conductivity for stainless steel (SS304) are estimated at the mean temperature of the fin.

The sum of the radiative emission and heat conduction is the total heat that must be supplied to the absorber-emitter to maintain the specified equilibrium temperature. From this energy balance, we solved for the required irradiance (H_s) based on two limiting cases: treating H_s as collimated or diffuse. For the collimated approximation, all of the incoming light through the aperture is simply incident on the MWCNT absorber. For the diffuse approximation, the radiative flux passing through the aperture is split between the active MWCNT absorber and the surrounding tungsten area based on their respective view factors (undergoing multiple reflections with the aperture/shield).

To determine the output power, we first solved for the total radiative heat transfer from the emitter to the PV cell for wavelengths smaller than that associated with the bandgap energy of the InGaAsSb cell (< 2.22 μm). This useful radiation generates photocurrent (I_{ph}) based on the following expression:

3-5 $$I_{ph} = \frac{-e}{hc_0}A_{pv}\int_0^\infty \lambda\,IQE_\lambda\,Q_{\lambda,e-pv}d\lambda$$

where e is the charge of an electron, h is Planck's constant, c_0 is the speed of light in a vacuum, A_{pv} is the area of the PV cell, IQE_λ is the spectral internal quantum efficiency of the PV cell, and

51

$Q_{\lambda,e\text{-}pv}$ is the spectral absorber radiation on the cell. Once the photocurrent was determined, the I-V characteristics (*i.e.*, maximum power point) of the PV cell were determined semi-empirically following the methods described by Chan *et al.*[69].

3.3   Experimental Procedure

To gain more insight into the complex energy conversion in our nanophotonic, area ratio optimized (NARO) STPV devices and compare it to theoretical predictions, we conducted two independent experiments—TPV and STPV. We investigated the maximum output power density (p_{out}) of the PV diode as a function of the absorber-emitter temperature (T_{ae}) in the TPV experiment and irradiance (H_s) in the STPV experiment. The temperature measurement in the TPV characterization was achieved by bonding a fine gage thermocouple directly to the absorber-side of the substrate.

Our mechanical system ensured alignment and gap control while minimizing parasitic conduction losses. The entire experimental layout was maintained in vacuum (< 0.5 Pa) to suppress convective and conductive heat transfer through the environment. We used a Xe-arc light source to simulate the solar spectrum and to supply a range of irradiances (H_s) from 10 to 75 Wcm^{-2}.

Solar Simulator Calibration
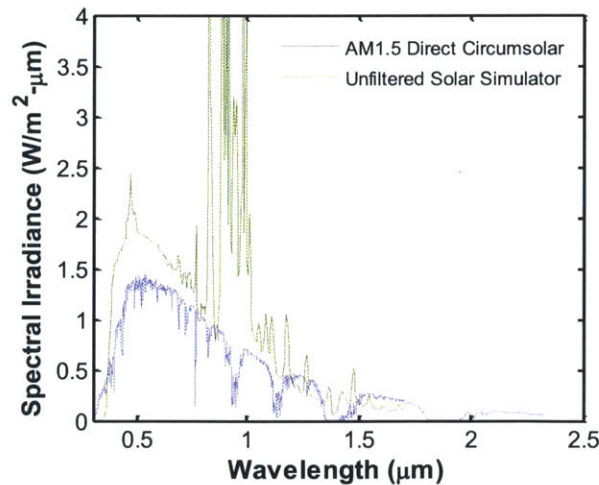
Figure 3-5 | Simulated solar spectrum.
Comparison between the AM1.5 direct spectrum used a standard for CSP applications and the spectrum provided by the Xe-arc lamp in our experiments.

The input power in our experiments was provided by a solar simulator (*92192, Newport Oriel Inc.*). While the Xe-arc spectrum deviates slightly from the standard AM1.5D (Figure 3-5), the MWCNT absorbing surface displays broad-spectrum near-blackbody absorptance [64-66] such that the difference in spectrally-weighted absorptance for the two spectra is negligible.

Light from the solar simulator was concentrated using a focusing lens system (*Hi Flux Concentrator, Newport Oriel Inc.*), shown in Figure 3-6a. The concentrator has two distinct configurations, converging-diverging and converging, which enable a wide range of irradiances to be supplied. This light was further concentrated with a secondary concentrator—a converging "light pipe" which reduces the size of the illuminated spot. The "light pipe" was constructed by sputtering a 250 nm silver layer on large glass microscope slides. The slides were cut using a die saw and assembled into a square frustum. The input power was determined shortly after each experiment by measuring the power through the aperture used in the experiment. This value was obtained using a thermopile detector (*919P-040-50, Newport Oriel Inc.*), which measures the total radiative power incident on the sensing surface. To determine the irradiance, this power was normalized by the area of the aperture (or equivalently, the absorber area in our experiments). The irradiance was varied between 10 and 75 W/cm^2 by utilizing both optical configurations mentioned above and moving the optical setup relative to our vacuum-enclosed experimental setup (Figure 3-6b) along a linear track (*i.e.*, the further the light source, the lower the irradiance).
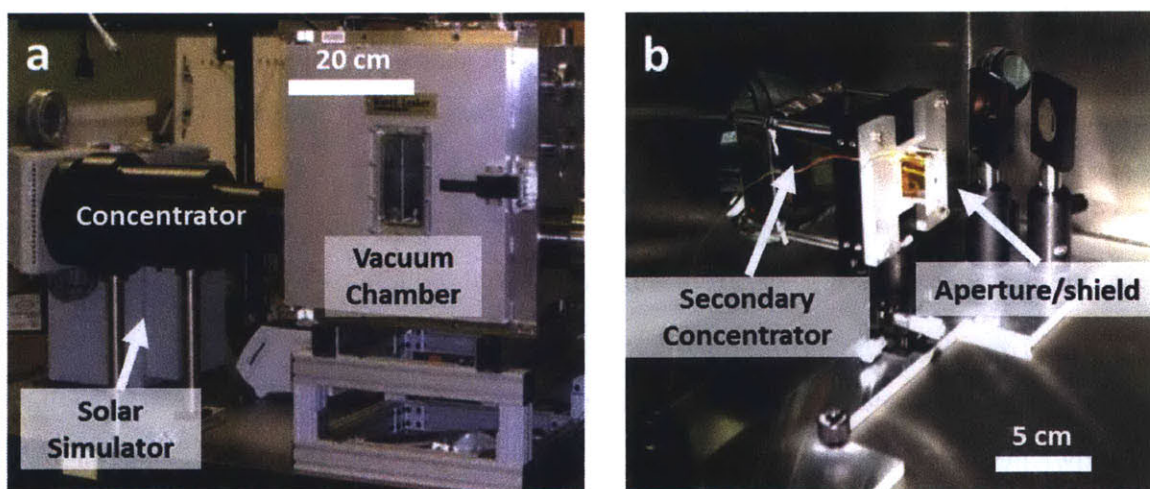
Figure 3-6 | Experimental setup.
a, Optical image showing solar simulator, primary concentrator, and vacuum chamber. b, Optical image of the experimental setup inside the vacuum chamber showing the secondary concentrator and the aperture/shield assembly.

Alignment and Gap Control

We developed a mechanical system and procedure to ensure repeatable alignment and gap control between the absorber-emitter sample, the PV cell, and the aperture/shield. In a horizontal orientation as shown in Fig. 1a (with gravity pointing down), the PV cell assembly was first mounted to the thermal management stage which was fixed to a z-axis stage (*122-0101, Opto Sigma Corp.*). The absorber-emitter sample was then placed on top of the PV; since the PV and the emitter have equal dimensions, the sample edges were easily aligned with the PV edges using a vertical straightedge. Second, the mechanical support needles were brought into contact with two sides of the absorber-emitter (550 μm thickness) to secure its position while maintaining alignment with the PV cell. Three stainless steel mechanical supports were used in the design: two hypodermic needles (*27Gx1.25", B-D*) on one side and a spring-loaded pin (*POGO-72U-S, ECT*) on the opposite side. The spring-loaded pin ensured that a light force was constantly applied on the absorber-emitter and the supports, minimizing pitch errors due to thermal expansion of the sample during operation. After securing the sample, a 300 μm gap between the emitter and the PV cell was set using the z-stage to lower the PV cell assembly with respect to the mounted absorber-emitter. The experimental setup was then mounted in the vacuum chamber and aligned with the aperture/shield (Ag-coated) using a manual linear stage to set the gap. Finally, the setup was connected to the chilled water loop and the instrumentation via feedthroughs.

TPV Emitter Temperature Measurement

The temperature of the absorber-emitter during the TPV-validation experiment was measured using a fine gage special limits thermocouple (*CHAL-005, Omega Engineering Inc.*) bonded to the absorber-side of the sample. The bond was established using a zirconia-based ceramic epoxy (*516 Ultra-Temp, Aremco Products Inc.*); the manufacturer's thermal annealing instructions were followed but in an inert (N_2/H_2-5%) environment to avoid oxidation of the MWCNT absorber.

PV Temperature and Thermal Load

The temperature of PV cell was measured using a type-K thermocouple (*Omega Engineering Inc.*) sandwiched between the packaged cell assembly and the thermal management stage. Chilled water was supplied to the thermal management stage using a liquid to liquid heat exchanger (*013736, NESLAB*) at a steady flow rate of 0.20±0.04 LPM and an inlet temperature

of 291±0.4 K. In the range of our experiments results, the temperature of the PV cell (T_{pv}) was dependent on the output power density (p_{out}) according to the following line of best fit:

3-6
$$T_{pv}[K] = 291.8 + 6.59\, p_{out}[Wcm^{-2}]$$

During our experiments, T_{pv} did not exceed 296 K. Using the flow rate and temperature measurements at the inlet and outlet of the stage, we determined the thermal load on the PV cell during operation:

3-7
$$q_{th}\,[Wcm^{-2}] = 0.33 + 15.46\, p_{out}\,[Wcm^{-2}]$$

The above thermal load is specific to the TPV components and geometrical configuration used in our experimental setup. By combining the above information, we can extract an effective thermal resistance between the PV cell and the environment (the chilled water inlet in our case):

3-8
$$R_{eff} = \frac{T_{pv} - T_{in}}{q_{th}} = 0.404[KW^{-1}cm^2]$$

Although our system relies on forced liquid convection to provide the desired experiment control, the above thermal resistance can easily be achieved using air-cooled heat sinks in a practical terrestrial application.

Determining Maximum Power Output

We performed several current-voltage (I-V) sweeps using a precision source-meter (*2440, Keithley Instruments Inc.*) once steady state operation of the STPV device was established. The I-V sweep was conducted in a 4-wire configuration with 50 points acquired in the range of 0-0.7 V. The reported output power density (p_{out}) is an average of the maximum power points for each I-V sweep acquired at steady operating conditions, normalized by the total cell area (1 cm^2).

3.4   TPV Results and Model Comparison

As shown in Figure 3-7, the output power of the PV cell is highly temperature-dependent as higher energy modes ($> E_g$) are excited with increasing emitter temperature. These experimental results are supported by a spectral quasi-1D diffuse radiative network model (SQ1DD). Our model assumes isothermal operation of the absorber-emitter (*i.e.,* $T_a=T_e=T_{ae}$) and accounts for

55

the experimentally measured spectral properties of the components and the geometrical configuration of our planar STPV layout. The results of the TPV experiment serve as validation of our model and provide an indirect method for determining the absorber-emitter temperature from the measured output power. This approach was used in the STPV characterization since a direct *in-situ* measurement of the absorber-emitter temperature increases parasitic losses and reduces the efficiency.
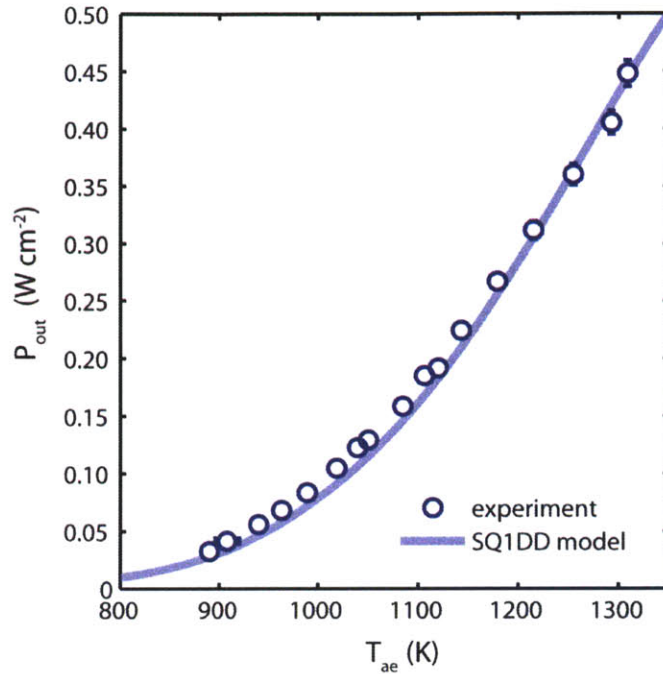
Figure 3-7 | TPV characterization.
Electrical output power density (p_{out}) generated by the InGaAsSb PV cell as a function of the 1D Si/SiO$_2$ PhC emitter temperatureModel prediction (solid line) shows an excellent agreement with experimental points (markers). Errors bars represent 95% confidence interval.

3.5   STPV Results and Model Comparison

With the TPV performance characterized, we investigated the full energy conversion processes in our NARO-STPVs with increasing emitter-to-absorber area ratios. Figure 3-8a shows the electrical output power of the STPV devices as a function of irradiance (H_s) and the absorber-emitter temperature (determined using the relation between p_{out} and T_{ae} shown in Figure 3-7). The upper and lower estimates of our SQ1DD model (associated with treating H_s as collimated or diffuse, respectively) bound the data within the experimental uncertainty.

The effect of increasing area ratio is manifested in shifting the operating points to a regime of increased irradiance (H_s) relative to the thermal re-emission loss (σT_{ae}^4). If we consider the

56

absorber solar collection efficiency (a major component of the thermal efficiency) for a blackbody surface:

$$3\text{-}9 \qquad \eta_a^{BB} = 1 - \frac{\sigma T_{ae}^4}{H_s}$$

we observe that decreasing the $\sigma T_{ae}^4/H_s$ ratio results in higher absorber efficiency. For our nearly-blackbody nanotube absorbers, this regime graphically corresponds to the lower right corner of Figure 3-8a. Using equation 3-9, we estimated that the absorber efficiency for AR 10 is above 75%.

Nevertheless, absorber efficiency is only a component of the overall STPV efficiency. Indeed, the efficiency of converting concentrated sunlight into electrical power ($\eta_t \eta_{tpv}$) does not monotonically increase with increasing area ratio for a fixed irradiance (H_s); as shown in Figure 3-8b, an optimal area ratio exists. To understand why this optimal area ratio arises, the competing effects of the thermal efficiency and the TPV efficiency are considered. The thermal efficiency is significantly enhanced as the area ratio is increased due to a rise in absorber efficiency (as explained above). In contrast, with increasing area ratio for a fixed H_s, the operating temperature of the absorber-emitter decreases since the ratio of the absorbed solar power ($\sim A_a H_s$) relative to the thermal emission ($\sim A_e \sigma T_{ae}^4$) decreases; ultimately leading to a decrease in TPV efficiency as the temperature drops significantly below the T_e^{opt}. These two competing effects lead to an optimal area ratio for a fixed irradiance, or equivalently, for a fixed optical concentration (10 times = 1 Wcm^{-2}, *ASTM E772*). In general, the optimum area ratio increases with optical concentration as shown in Figure 3-8b, where the optimum shifts from approximately $AR=2$ to $AR=5$ as H_s is increased from 20 to 48 Wcm^{-2}.

Using the relation between p_{out} and T_{ae}, we investigated the system performance as a function of absorber-emitter temperature. Figure 3-8c shows that the efficiency initially increases sharply with emitter temperature (below 1200 K) as modes with energies above E_g are increasingly excited. As the temperature approaches T_e^{opt}, the efficiency plateaus as increasing useful emission (*i.e.*, radiation at $E > E_g$) is balanced by increasing re-emission losses and PV inefficiencies associated with high photocurrents. Increasing area ratio for a given absorber-emitter temperature results in increased conversion efficiency (Figure 3-8d). Since the TPV

efficiency is determined by the emitter temperature, the relative increase in conversion efficiency ($\eta_t \eta_{tpv}$) is completely attributed to the increase in thermal efficiency. At T_e^{opt} (1285 K), we experimentally demonstrated a two-fold increase in thermal efficiency from $AR=1$ to $AR=5$.
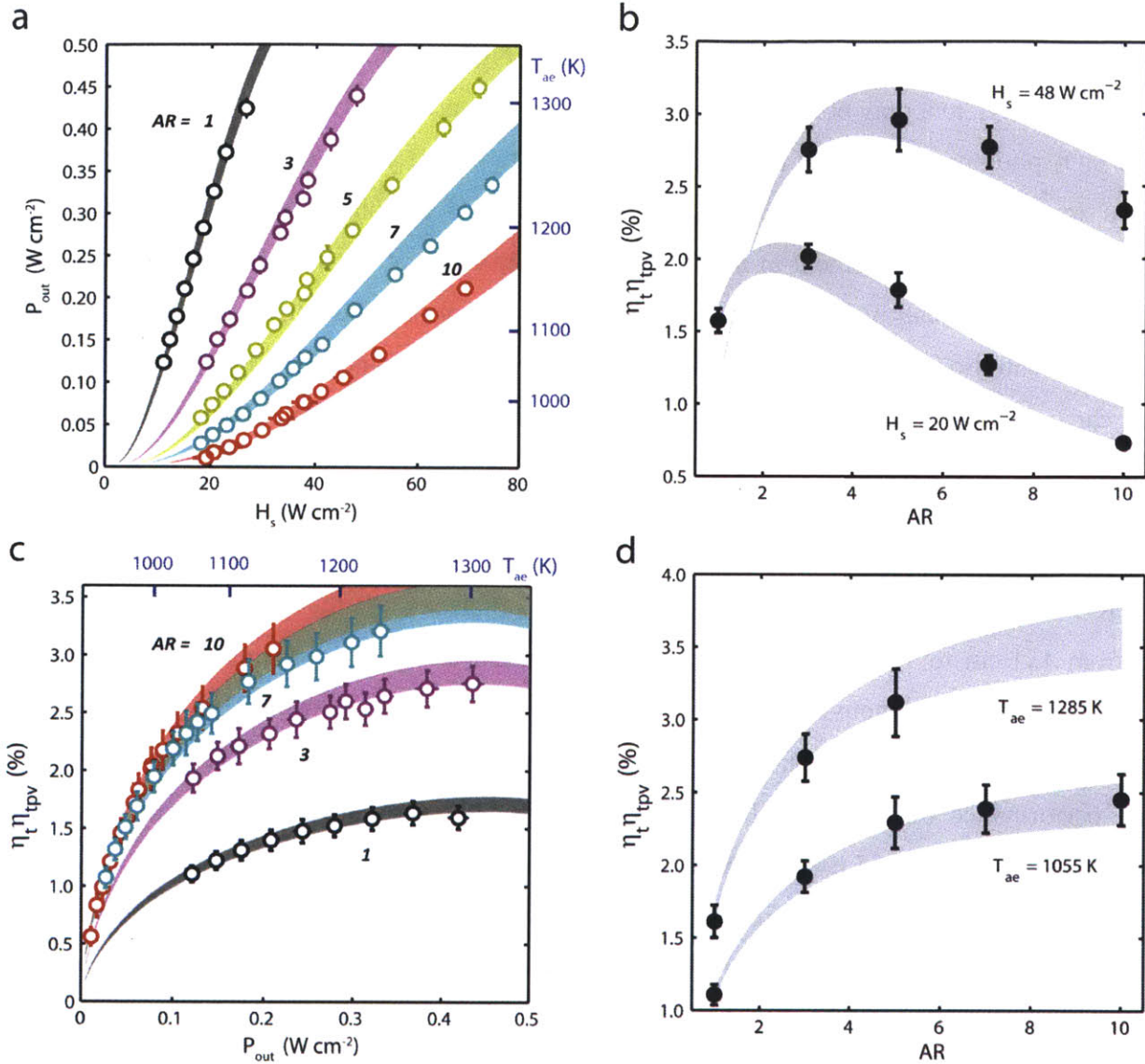
Figure 3-8 | Performance characterization and optimization of the nanophotonic STPV device.
a, Electrical output power density (p_{out}) and absorber-emitter temperature (T_{ae} determined from Fig. 2) with increasing H_s (input solar power normalized by the aperture area) for AR=1 to 10. As the area ratio is increased, the device operates in a regime of low $\sigma T_{ae}^4/H_s$, which is favorable for the absorber efficiency of the nanotube array. b, Conversion efficiency (concentrated solar to electrical, $\eta_t\eta_{tpv}$) with increasing area ratio for a fixed H_s=20 and 48 W/cm². Competing effects of the thermal efficiency and the TPV efficiency lead to an optimal area ratio for a fixed H_s. c, Conversion efficiency as a function of the p_{out}, or equivalently, T_{ae} (AR=5 omitted for clarity). d, At a given p_{out} or T_{ae}, the conversion efficiency increases with increasing area ratio which is attributed to an increase in thermal efficiency. Markers are experimental points (errors bars represent 95% confidence interval); solid bands represent the SQ1DD model: treating H_s as collimated or diffuse sets upper and lower bounds, respectively.

Overall, the highest conversion efficiency ($\eta_t\eta_{tpv}$) that we measured is 3.2±0.2% using an AR=7 device, which is 3-4 times greater than previous STPV experiments [13]. This was achieved

using a compact design at substantially lower levels of optical concentration (~750 times), which will enable higher optical efficiencies. As shown in Figure 3-9, significant enhancements in efficiency relative to a gray body absorber-emitter ($\varepsilon=0.5$) were achieved through the use of: (i) a 1D Si/SiO_2 photonic crystal for improved spectral performance of the emitter and a vertically-aligned multi-walled carbon nanotube array for nearly ideal solar absorptance (a two-fold contribution to the improvement in $\eta_t\eta_{tpv}$) and (ii) optimization of the active emitter-to-absorber area ratio (an additional two-fold improvement). The concept of optimizing area ratio at a fixed optical concentration with a nanophotonic absorber-emitter, experimentally demonstrated in this work, can be easily implemented in future STPV designs to increase overall efficiency.

3.6   Near-term Improvements

From the SQ1DD model, our highest efficiency operating point corresponds to a temperature of 1235 K with 54% thermal efficiency and 5.8% TPV efficiency. As the device scales in planar area from 1x1 cm to 10x10 cm (Figure 3-9), the thermal efficiency will improve to ~75% as parasitic losses to the inactive area and mechanical supports decrease from 91% to 20% of the useful emission (see Figure 3-9b,c). Another important aspect limiting our conversion efficiency is the performance of the PV cell ($V_{oc}=0.57E_g$, 0.48 fill factor, 83% active area). Using an improved, yet realistic 0.55 eV InGaAsSb cell ($V_{oc}=0.70E_g$, 0.74 fill factor, 90% active area) and a sub-bandgap photon reflecting filter [68], the STPV efficiency will approach 20% at moderate optical concentrations (Figure 3-9a). Although this result requires scale up of our processing and experimental systems, our robust experimental STPV demonstration of the (1 cm^2) nanophotonic absorber-emitter and key design elements validates our model.
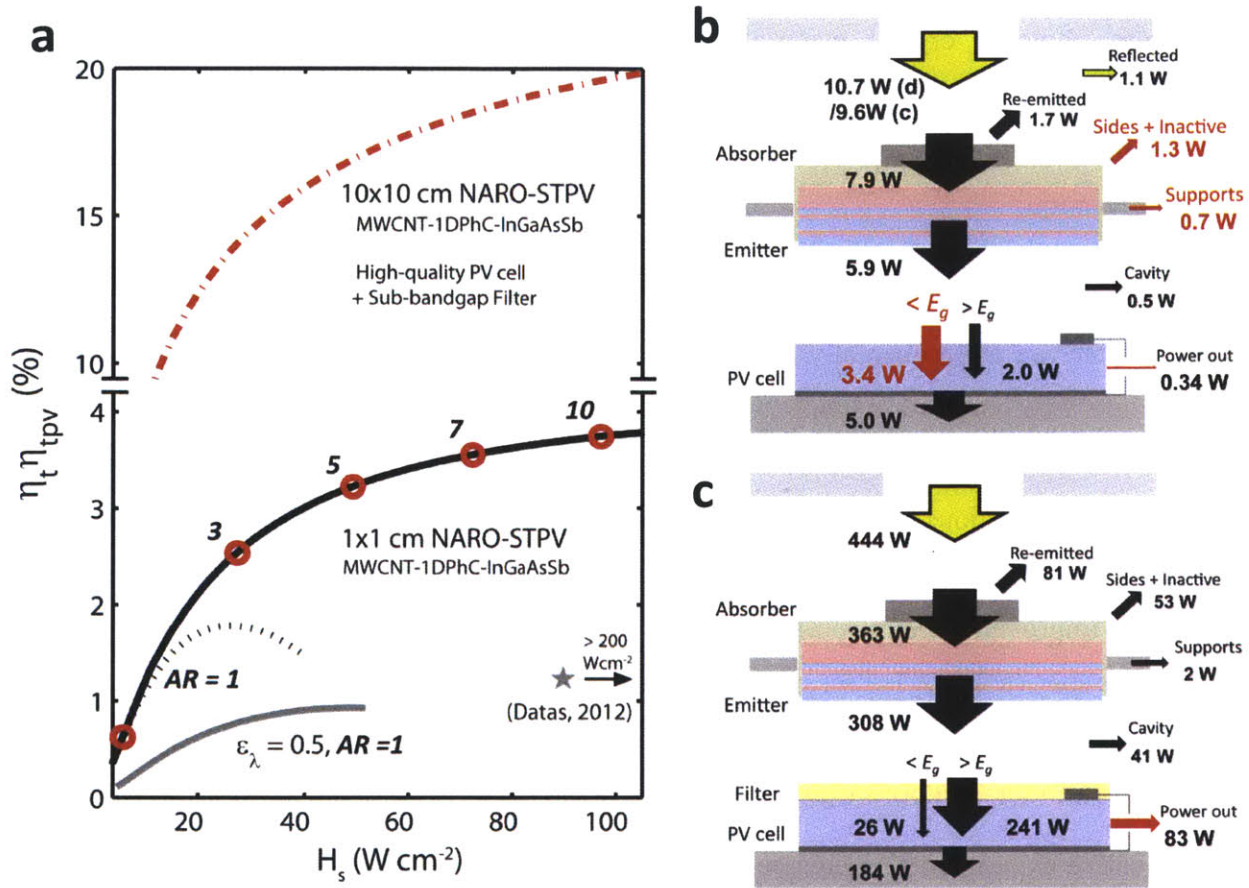
Figure 3-9 | Near-term improvements in efficiency for nanophotonic, area ratio optimized (NARO) STPVs.

Conversion efficiency ($\eta_t\eta_{tpv}$) as function of a solar irradiance (H_s). Contributions to $\eta_t\eta_{tpv}$ relative to a gray body absorber-emitter MWCNT-1DPhC absorber-emitter (two-fold improvement), area ratio optimization (additional two-fold improvement). Efficiencies approaching 20% were predicted with a scaled-up (10x10 cm) NARO-STPV utilizing a high-quality 0.55 eV PV module with a sub-bandgap reflector20. All points and predictions were made using the SQ1DD model (Hs treated as collimated). Power conversion and loss mechanisms at an irradiance of 75 W/cm^2 in the following NARO-STPVs (obtained using the SQ1DD): a, the experimentally demonstrated AR=7 (1cm^2) device (d and c represent diffuse and collimated irradiance, respectively); and b, a scaled-up (100 cm^2) AR=17 device utilizing a high-quality 0.55 eV PV module with a sub-bandgap reflector [68].The scaled-up device was simulated with 1 mm gaps between the shield/absorber and emitter/PV, and mounted using 8 stainless steel supports (difference between the diffuse and collimated irradiance is negligible in this configuration). Width of arrow is proportional to the magnitude of power it represents.

The efficiency can be further enhanced through improvements in low-bandgap PVs (such as GaSb, Ge, and graphene-based PVs), better spectral control [5, 18, 24] and higher temperature operation. Unlike Si PV cells that have reached ~85% of their thermodynamic efficiency, the best-performing low-bandgap (TPV) cells exhibit 30-50% of their thermodynamic efficiency [14, 67, 68, 71]. By re-optimizing the geometry of the 1D photonic crystal, our nanophotonic absorber-emitter may be paired with PV bandgaps up to ~0.7 eV; beyond this point, higher

61

temperature photonic crystal materials are required, such as refractory metals [21]. The efficiency improvements demonstrated in this work, along with the promising predictions using a validated model, suggest the viability of nanophotonic STPVs for efficient and scalable solar energy conversion.

3.7   Summary

In this chapter, we experimentally demonstrated a novel nanophotonic STPV device which for the first time incorporates a nanophotonic absorber-emitter. By integrating these materials into an innovative device design, we achieved a solar-to-electrical conversion efficiency of 3.2%, much better than previous STPV embodiments which relied on the intrinsic spectral properties of materials. Significant improvements were achieved through the use of (i) Si/SiO$_2$ photonic crystals for improved spectral performance of the emitter and vertically aligned multi-walled carbon nanotubes (MWCNTs) for nearly ideal solar absorptivity and (ii) by operating the device in a higher-flux regime (*i.e.*, ~750 suns) through effective thermal spreading between the absorber and emitter, and optimization of the active emitter-to-absorber area ratio.

The innovative experimental design enables facile integration of nanophotonic surfaces in STPV research and development, which has been predominately theoretical to this point. Unlike previous STPV embodiments, the following are easily accomplished in our planar design: fabrication of nanophotonic surfaces via conventional planar processing techniques, and device optimization via tuning of the emitter-to-absorber area ratio.

The work facilitates a technology for conversion of sunlight to electricity which promises to leverage the benefits of both the photovoltaic (PV) and the concentrated solar power (CSP) approach.

Chapter 4

4. Low optical concentration regime: Achieving high-temperature spectral selectivity

This chapter presents the design and experimental characterization of a STPV device which incorporates a two-dimensional photonic-crystal (2D PhC) absorber-emitter to achieve experimentally measured spectral conversion efficiencies >10%. These results were achieved by tailoring the spectral properties of the absorber-emitter through surface nanostructuring of tantalum (Ta) and minimizing parasitic thermal losses through an innovative vacuum-enclosed experimental setup. The chapter describes the design and fabrication of the 2D Ta PhCs absorber and emitter that enabled the high spectral performance. The experimental methods described in Chapter 3 are used to characterize the 2D PhC absorber-emitter when coupled to a 0.55 eV InGaAsSb PV cell as a function of the solar irradiance. This chapter shows how this absorber-emitter PhC surface can be used to exceed the ultimate efficiency of a 0.55 eV cell (as defined by Shockley-Queisser). By incorporating a sub-bandgap photon reflecting filter on the PV surface and optimizing the absorber-emitter ratio, the demonstrated 2D Ta PhCs enable a realistic STPV configuration to reach over 40% spectral conversion efficiency at moderate optical concentrations.

The performance of STPVs is highly dependent on the efficient conversion of sunlight to useful thermal emission, which the PV cell can then harness to excite electron-hole pairs and generate power. To identify the added value of placing an absorber-emitter in between the incident solar radiation and a (low-bandgap) PV cell, we consider the efficiency of the same cell when exposed to solar radiation (AM 1.5D), and when exposed to thermal emission from the solar-powered emitter. We demonstrate that unless the absorber-emitter is properly designed, placing it in front of the PV cell may degrade the overall solar-to-electrical efficiency of the system.
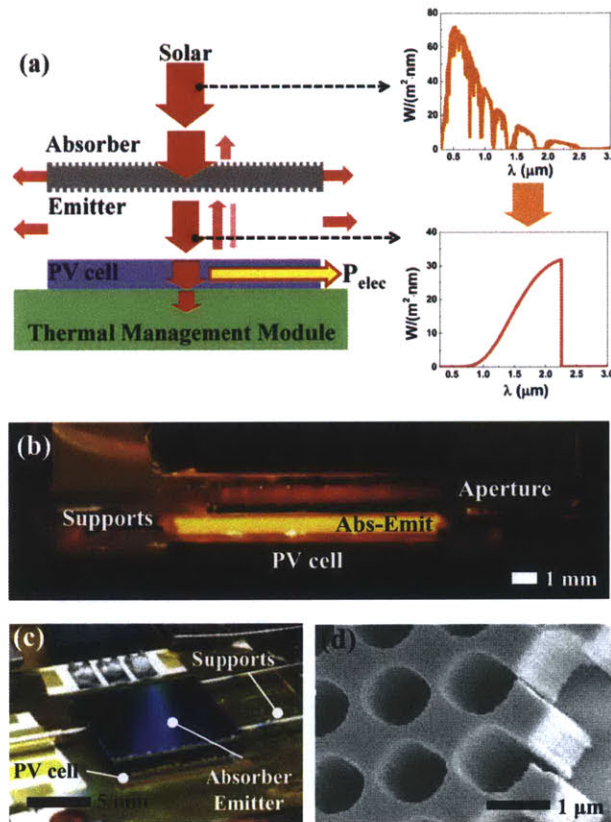
Figure 4-1 | 2D photonic crystal based STPV device.
(a) Schematic of a 2D PhC absorber-emitter that converts solar radiation with a broad spectrum into a tailored spectrum matched to the spectral response of the PV cell. (b),(c) Optical images of our vacuum-enclosed devices composed of a 2D PhC absorber-emitter and a 0.55 eV bandgap PV cell (InGaAsSb). The visibly glowing absorber-emitter (b) indicates successful high temperature operation (~1300 K). The device was suspended by spring-loaded hollow metallic supports to minimize parasitic thermal losses. (d) SEM of the 2D PhC emitter showing an array of high-aspect ratio cavities etched in Ta.

To isolate the effect of the absorber-emitter mediated spectral-conversion process, we consider the limit in which the PV cell generates one electron-hole pair from each incident photon with sufficient energy ($>E_g$) and extracts it at the bandgap voltage (V_g). This limit is in accordance with the definition of ultimate efficiency, presented by Shockley-Queisser [4]. Here, we extend the definition of ultimate efficiency to account for the possibility of a converted incident spectrum using the ultimate spectral conversion efficiency (SCE_U):

$$4\text{-}1 \qquad SCE_U = \frac{E_g R_s}{H_s} = \frac{\int_0^{\lambda_g} \frac{\lambda}{\lambda_g} H_{\lambda,pv} d\lambda}{H_s}$$

where H_s is the total solar irradiance on the device, H_λ is the spectral irradiance on the PV cell, R_s is the flux of above-bandgap quanta incident of the cell, and λ_g and E_g are the bandgap wavelength and energy of the PV, respectively. In the case where the spectral irradiance is equal to the solar irradiance, the SCE_U is equivalent to the ultimate efficiency. However, when the incident spectrum is modified through the *photo-thermal-photo* conversion process in the absorber-emitter, the ultimate efficiency can naturally be exceeded in the case that the thermal emission contains a greater fraction of useful near-bandgap radiation.

In real devices, the spectral conversion efficiency of the PV is proportional to the photocurrent density (J_{ph}) generated by the PV assuming a wavelength and angular independent external quantum efficiency. Hence, using easily measurable quantities, we will define the real spectral conversion efficiency as:

$$4\text{-}2 \qquad SCE_R = \frac{J_{ph} V_g}{H_s}$$

where V_g is the PV bandgap voltage. In our experimental section, we will use SCE_R to compare the performance of the PV cell with and without the absorber-emitter.

4.2 Photonic Crystal Design and Optimization

The photonic crystal absorber-emitter consists of a 2D array of high-aspect ratio micro-cavities (Figure 4-1d) etched into both sides of a Ta substrate. These structures were fabricated using interference lithography followed by deep reactive ion etching of Ta [21, 51]. Even at the high operating temperatures, the spectral properties of the Ta PhCs exhibit high-selectivity with a

sharp cut-off enabled by the PhC surface structure (Figure 4-2). For the absorber, the cut-off wavelength (λ_c) and the spectral properties were designed to optimize absorption (high ε_λ) of short-wavelength concentrated sunlight ($\lambda<\lambda_c$), and suppress re-emission (low ε_λ) of long-wavelength thermal radiation ($\lambda>\lambda_c$). For the emitter, the spectral properties were optimized to enhance thermal emission of useful radiation with energies above the PV bandgap ($\lambda<\lambda_g$) while suppressing sub-bandgap radiation ($\lambda>\lambda_g$).

The design of the PhCs is a square array of cylindrical holes with period (a), radius (r), and depth (h) created on a tantalum (Ta) substrate. Ta was selected due to its high melting point (3290 K), low vapor pressure and low emissivity at long wavelengths. The emissivity of the substrate is selectively enhanced in the PhC by coupling to the cavity modes, and the cutoff wavelength is tunable by adjusting the fundamental cavity resonant frequency through changes in the dimensions of the cavities, while the maximum emittance of the first resonance peak below the cutoff is achieved via Q-matching [19].
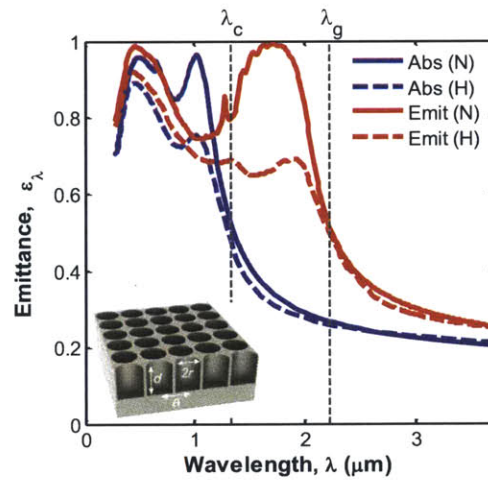
Figure 4-2 | 2D Ta PhC absorber-emitter spectral properties.
Simulated normal (N) and hemispherically-averaged (H) spectral emittance at 1300 K for the fabricated. For the absorber, cavity dimensions are a=0.65/r=0.25/h=4.6 μm. For the emitter, the cavity dimensions are a=1.3/r=0.55/h=8.0 μm.

The optimization of the emitter was performed using the spectral efficiency η_{sp} as a figure of merit (FOM), which is defined as the number of photons emitted in the useful wavelength range relative to the total number of emitted photons. This is a measure of the spectral selectivity of the emitter at a given operating temperature T. The useful wavelength range is given by the bandgap and EQE of the PV cell; we used InGaAsSb PV cells with a bandgap of 0.55 eV and a useful

wavelength range of about 1 µm-2.3 µm and we optimized the geometrical parameters of the emitter for a target operating temperature of 1300 K, using the hemispherical emissivity of the PhC. The hemispherical emissivity of the PhCs was computed using the Fourier Modal Method using a freely available software [72].

For the optimization of the absorber, the thermal transfer efficiency η_T was used as the FOM [18, 73]:

$$4\text{-}3 \qquad\qquad \eta_T = \bar{\alpha}_{abs} - \frac{\bar{\varepsilon}_{abs} \cdot \sigma T^4}{H_s} = \bar{\alpha}_{abs}\left(1 - \frac{\bar{\varepsilon}_{abs}}{\bar{\varepsilon}_{tot}}\right)$$

where T is the operating temperature, $\bar{\alpha}$ is the absorptivity of the absorber averaged over the solar spectrum, $\bar{\varepsilon}$ is the emissivity of the absorber averaged over the blackbody radiation at T, σ is the Stefan-Boltzmann constant, H_s is the irradiance of the solar spectrum (AM 1.5D). In a STPV system, the irradiance needed to reach a certain operating T depends on the balance of the input and output power, and we can rewrite the equation using the sum of the averaged emissivities of all surfaces, including the absorber, emitter and sides. We approximate that all of the absorber-emitter losses are radiative.

Again, we optimize the design for a target operating of 1300 K. The spectral emittance of the 2D Ta PhC absorber and emitter is close to the black-body limit at short wavelengths and approaching that of polished metal at long wavelengths, with a sharp cutoff separating the two regimes. The spectral emittance of the fabricated PhCs, as determined from reflectance measurements at near normal incidence at room temperature, shows good agreement with the simulated spectra.

4.3 Device Characterization

We designed the experimental system for characterizing high-temperature planar STPVs aiming to validate our previously-developed model [74] and compare the performance to the PV cell without the absorber-emitter. The following experimental capabilities were developed to properly account for the coupled energy conversion steps and to measure the device characteristics: incident power of simulated solar radiation, absorber/emitter temperature (see *TPV Validation*), current-voltage characterization, and thermal load on the PV cell. The

experimental layout (Figure 4-1b-c) minimizes parasitic heat losses while allowing for precise alignment and gap control between the absorber-emitter and the PV cell.

4.3.1   TPV Validation

An accurate measurement of the emitter temperature with minimal impact on the temperature distribution of the emitter was obtained using a thin gauge thermocouple bonded to the back of the emitter substrate.
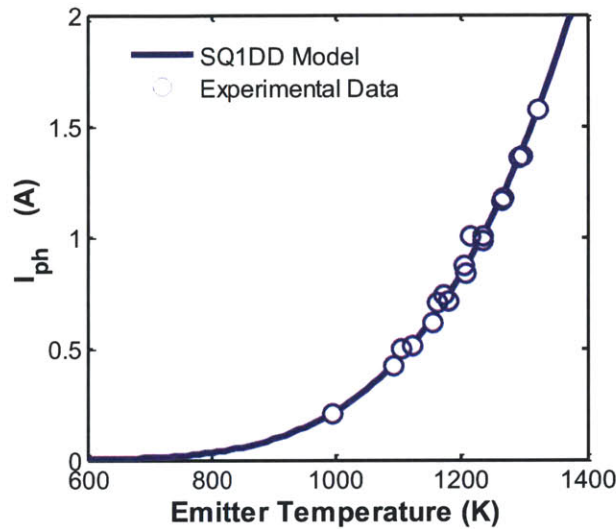
Figure 4-3 | Photocurrent generated by 2D Ta PhC- InGaAsSb TPV.
Two 0.55 eV InGaAsSb (0.5cm x1cm) cells connected in series as a function of the 2D Ta PhC (1x1 cm) emitter temperature. The cell and emitter were separated by a 300 μm vacuum gap. Line and symbols represent the results obtained from the model and experiments, respectively.

Using the experimental system, we investigated a solar-powered TPV system composed of the 2D Ta PhC as a high-temperature spectrally selective emitter paired with an InGaAsSb PV cell (0.55 eV). The IV characteristics of the TPV were experimentally characterized by controlling the solar power incident on the device, and accordingly varying the emitter temperature from room temperature to around 1300 K. The photocurrent generated by the PVs (at a slightly negative bias voltage) was measured as a function of the 2D PhC emitter temperature. As shown in Figure 4-3, predictions using our numerical model [74] match the results within experimental uncertainty, validating the numerical models used throughout the study.

4.4 STPV and PV Comparison

In a STPV configuration, we characterized the *SCE* of our 2D PhC absorber-emitter when coupled to the 0.55 eV InGaAsSb PV cell as a function of the solar irradiance (Figure 4-4). The incident simulated sunlight was passed through an aperture with matching dimensions to the absorber, spaced 500 μm apart. As in the TPV experiment, the emitter was separated from the cell by a 300 μm vacuum gap. For comparison, we performed the same experiment but in a concentrated PV configuration where we measured the photocurrent generated by the PV cell without the absorber-emitter in front of it. To be consistent, the absorber and the PV cell were held in the same plane for both experiments (relative to the aperture). Furthermore, the temperature of the PV cell was consistent in both experiments.

In the STPV configuration, the *SCE* increased with increasing irradiance since the system efficiency was highly temperature-dependent. The highest overall *SCE* we measured for the STPV configuration was approximately 11% at 13 W/cm^2 of irradiance. At this point, the absorber-emitter was approximately at 1300 K, which is near the design temperature. On the other hand, the PV configuration achieved a *SCE* of 19-20%, suggesting that placing the absorber-emitter degrades the overall performance, primarily due to parasitic losses and sub-bandgap emission. Nevertheless, the experimental system represents a proof-of-concept STPV demonstration and integration of 2D Ta PhCs. When the system is scaled-up and optimized, the STPV performance can significantly exceed that of the PV configuration.
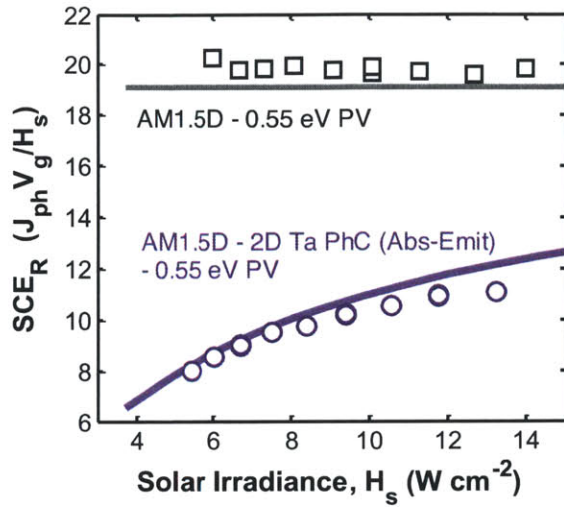
Figure 4-4 | Spectral conversion efficiency.
Comparing direct AM 1.5D illumination of the 0.55 eV cell (PV configuration), to the STPV configuration with a 2D Ta PhC absorber-emitter under the same conditions.

4.5 Exceeding the Shockley-Queisser Limit

The above experimental validation suggests that STPVs are rapidly approaching the performance of single junction PV cells. By incorporating a sub-bandgap photon reflecting filter on the PV surface [68] and scaling the emitter to ten times the area of the absorber (*i.e.*, area ratio of 10) [75], the ultimate spectral conversion efficiency (SCE_U) of the 2D PhC-based STPV will exceed ultimate efficiency (as defined by the Shockley-Queisser) for this 0.55 eV cell at optical concentrations as low as ~200 Suns (Figure 4-5). At higher concentrations, the ultimate spectral conversion efficiency approaches 45% for this device. These are promising results for low concentration STPVs.

70
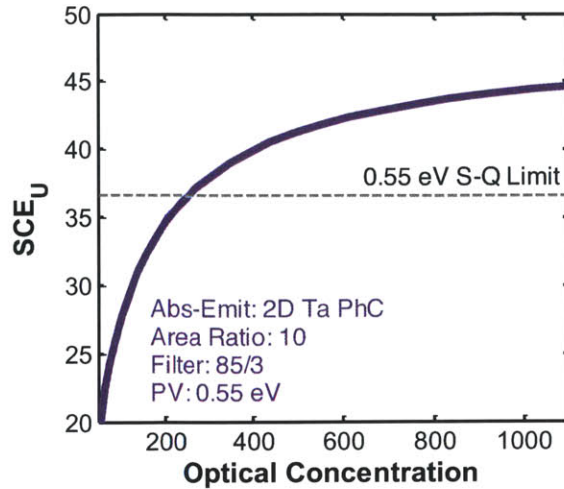
Figure 4-5 | Increasing the ultimate efficiency.
2D Ta PhCs enable STPV to exceed the ultimate efficiency for a 0.55 eV cell (as defined by Shockley-Queisser), at relatively low optical concentrations when integrated in an optimized system design (*i.e.*, by scaling up the emitter relative to the absorber and introducing a sub-bandgap reflecting filter).

4.6   Summary

We presented the design and characterization of a planar STPV composed of 2D Ta PhC absorber-emitter and a 0.55 eV InGaAsSb PV cell. The experimental setup minimized parasitic heat losses and allowed precise alignment of the components. Through TPV and STPV experiments, we showed excellent agreement with our previously reported models. We also directly compared the performance with and without the absorber-emitter, showing that the absorber-emitter can degrade the overall performance if the system has substantial sub-bandgap emission and parasitic losses. By scaling-up the emitter relative to the absorber and incorporating a sub-bandgap filter into our model, we showed that a 2D Ta PhC enabled STPV can exceed the Shockley-Queisser ultimate efficiency at relatively low irradiances (~200 Suns). This study demonstrates the components and facilitates the design of such a high-efficiency system.

71

PART II: THERMAL-FLUID SYSTEMS

Chapter 5

5. Evaluating solar thermal heat transfer fluids

The choice of proper heat transfer fluids is essential for the development of high-efficiency solar thermal power plants, as it determines the thermal and hydraulic performance of the collector field. Previously, Becker [76] evaluated various heat transfer fluids for use in solar thermal power plants by comparing their individual thermophysical properties. However, the performance of heat transfer fluids is determined by the combination of the properties rather than by each of the individual properties. To evaluate the effects of combined thermophysical properties, researchers have suggested various figures of merit (FOMs). Mouromtseff introduced the Mouromtseff number (Mo) to evaluate the effects of combined fluid properties on the convective heat transfer coefficient of internal turbulent flow based on the Dittus-Boelter correlation [77]:

$$Mo = \frac{\rho^{0.8} c_p^{0.33} k^{0.67}}{\mu^{0.47}} \ .$$

5-1

Bonilla suggested another FOM by comparing the required pumping power to maintain the temperature difference between inlet and outlet of carrier fluid [78]:

$$\frac{\rho^2 c_p^{2.8}}{\mu^{0.2}} \ .$$

5-2

Even though these FOMs provide meaningful comparisons among various heat transfer fluids, there are several limitations. Mouromtseff [77] compared only heat transfer characteristics in the radial direction assuming that all fluids have the same flow velocity. Meanwhile, Bonilla [78] ignored radial heat transfer between the wall and the fluid and only considered axial heat flow. Since performance of solar thermal heat transfer fluids is determined by the combined effects of

73

the thermal storage capacity of the fluid, convective heat transfer from the wall to the fluid and hydraulic performance characterized by pumping power, an alternative FOM is desired.

Recently, Murakami and Mikić reported the optimization of heat sinks based on the minimization of pumping power assuming the same temperature difference between wall outlet and fluid inlet [79]. Their approach introduced dimensionless pumping and thermal loads, and showed important relationships among the parameters to optimize heat sink designs considering the axial and radial heat flow as well as the pumping power requirement. Here, the methodology suggested by Murakami and Mikić [79] is used to develop a new FOM to evaluate the performance of conventional solar thermal heat transfer fluids.

In section 5.2, existing heat transfer fluids such as oils and molten salts are evaluated based on a new figure of merit capturing the combined effects of thermal storage capacity, convective heat transfer characteristics and hydraulic performance of the fluids. Thermal stability, freezing point and safety issues are also discussed. Emerging technologies and alternative options for solar thermal heat transfer fluids are examined in the rest of the chapter including ionic liquids/melts (5.3) and suspensions of nanoparticles (5.4), focusing on the benefits and technical challenges.

5.1 New figure of merit

Nomenclature

a ratio of heated perimeter to perimeter

A area (m^2)

C_k coefficient of k enhancement ($Wm^{-1}K^{-1}$)

C_p specific heat capacity at constant pressure ($Jkg^{-1}K^{-1}$)

C_μ coefficient of μ enhancement ($kgm^{-1}s^{-1}$ or Pa s)

d particle diameter (nm)

D diameter (m)

E heat transfer enhancement factor

Fr Froude number

g gravitational acceleration (ms^{-2})

G Total mass flux through a tube ($kgm^{-2}s^{-1}$)

h heat transfer coefficient ($Wm^{-2}K^{-1}$), height (m), enthalpy (Jkg^{-1})

k thermal conductivity ($Wm^{-1}K^{-1}$)

K permeability (m^2)

L length (m)

m'' mass flux ($kgm^{-2}s^{-1}$)

M two-phase flow pressure drop multiplier

p perimeter (m)

P pressure (Pa)

Pr Prandtl number

q'' heat flux (Wm^{-2})

r radius (m)

Re Reynolds number

S heat transfer correction factor

T temperature (K)

u velocity (ms^{-1})

V averaged bulk velocity (ms^{-1})

We Weber number

x vapor quality

Greek symbols

α	thermal diffusivity (m^2s^{-1})
β	tilt angle (º)
θ	angle (º)
Λ	dimensionless thermal load
μ	dynamic viscosity ($kgm^{-1}s^{-1}$)
ρ	density (kgm^{-3})
Y	dimensionless pumping load
ϕ	volume fraction of solid phase
ν	kinematic viscosity (m^2/s)

Subscript

c	capillary
eff	effective
f	fluid
g	gas
h	hydraulic diameter
in	inlet
l	liquid
le	assuming the entire flow as liquid
max	maximum
out	outlet
p	particle
ph	phase
$pool$	pool boiling
s	surface
w	wall

Figure 5-1 shows a schematic of a solar collector tube which is simplified as a single channel of diameter D and length L. The heat flux is assumed to be uniform throughout the entire length and the temperature distribution inside the solid walls is neglected.
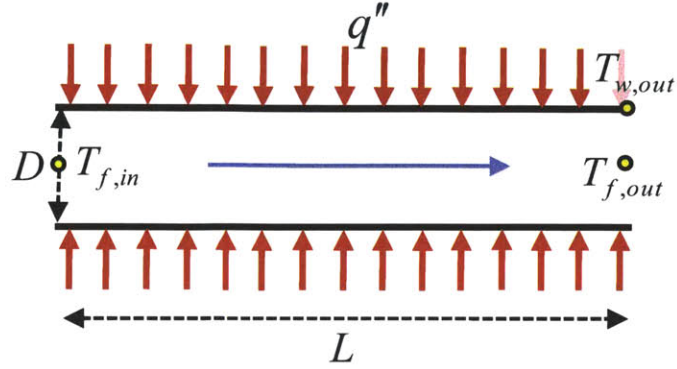
Figure 5-1: Schematic of a solar collector tube.
The tube is simplified as a single channel of diameter D and length L; $T_{f,in}$ and $T_{f,out}$ represent the inlet and outlet temperature of carrier fluid, respectively. $T_{w,out}$ is the outlet wall temperature.

From conservation of energy, the amount of heat stored in the fluid can be described as:

$$\rho V A c_p (T_{f,out} - T_{f,in}) = q'' a p L ,$$

5-3

where V and p represent the average bulk velocity of fluid and the perimeter of tube, respectively. a is the correction factor for the case when the heat flux is applied to a fraction of the perimeter. For solar thermal collector tubes, the thermal stability of the heat transfer fluid and the selective coating imposes a restriction on $T_{w,out}$. Therefore, Eq. 5-3 is rewritten using the maximum temperature difference between the tube wall and fluid inlet ($\Delta T_{max} = T_{w,out} - T_{f,in}$):

$$T_{f,out} - T_{f,in} = (T_{w,out} - T_{f,in}) - (T_{w,out} - T_{f,out}) = \Delta T_{max} - \frac{q''}{h} .$$

5-4

Then, the pumping power is normalized by the amount of heat transferred to the fluid per time:

$$\overline{P} = \frac{\Delta P V A}{q'' a p L} = \frac{1}{8a} \frac{Y}{A} \frac{f \, \mathrm{Re}^3}{\overline{D}^3} ,$$

5-5

where $\overline{D}$ is a normalized diameter (D/L), f is the internal friction factor, and Re is the Reynolds number. Y and Λ represent the dimensionless pumping and thermal loads, respectively:

$$Y \equiv \frac{\rho v^3}{k\Delta T_{max} L^2}$$

5-6

$$\Lambda \equiv \frac{q'' L}{k\Delta T_{max}} \quad .$$

Eqs. 3 and 6 are substituted into Eq. 5-4:

5-7

$$1 = \frac{\Lambda\overline{D}}{Nu} + F \quad ,$$

where F is a normalized temperature rise of the fluids, ($T_{f,out} - T_{f,in}$)/ ΔT_{max} , described by:

5-8

$$F \equiv \frac{4a\Lambda}{Re \cdot Pr} \quad .$$

For turbulent flow in circular tubes, the internal friction factor and the *Nusselt* number (*Nu*) can be estimated as [80, 81]

5-9

$$f = 0.184 Re^{-0.2}$$

$$Nu = 0.023 Re^{0.8} Pr^{0.4} \quad .$$

By substituting Eqs. 5-6-5-9 into Eq. 5-10:

5-10

$$\overline{P} \propto \left(\frac{Y\Lambda^{2.4}}{Pr^{1.6}}\right)\left(\frac{1}{F^{0.4}(1-F)^3}\right) .$$

Assuming the heat flux (q''), tube length (L) and the maximum temperature difference between the tube wall and fluid inlet (ΔT_{max}) are fixed, the normalized pumping power is determined by the properties of the fluid and the Reynolds number. To elucidate the effect of fluid properties on the normalized pumping power without introducing complexity associated with the Reynolds number, the normalized temperature rise (F) is optimized:

78

5-11
$$\frac{\partial}{\partial F}\left(\frac{1}{F^{0.4}(1-F)^3}\right)=0 .$$

By substituting the optimized F (= 2/17) into Eq. 5-10, the normalized pumping power can be described:

5-12
$$\overline{P} \propto \left(\frac{\mu^{1.4}}{\rho^{2.0}c_p^{1.6}k^{1.8}}\right)\left(\frac{q''^{2.4}}{\Delta T_{max}^{3.4}}\right)L^{0.4} .$$

Then, the performance of heat transfer fluids is determined by the combination of fluid properties in the first parentheses. Since the normalized pumping power needs to be minimized, the FOM of solar thermal heat transfer fluids becomes:

5-13
$$FOM = \frac{\rho^{2.0}c_p^{1.6}k^{1.8}}{\mu^{1.4}} .$$

This new FOM is suggested to evaluate the thermal and hydraulic performance of heat transfer fluids for solar thermal applications. Compared with the Mo number (Eq. 5-1), the suggested FOM (Eq. 5-13) has a strong dependency on ρ and c_p which characterize the heat storage capacity of fluid. In addition, unlike the previous FOM (Eq. 5-2), the thermal conductivity of fluid k also has a strong effect as the new FOM includes heat transfer characteristics between wall and fluid in the radial direction. When the carrier fluids experience phase-change in the collector tube, the changes in thermal and hydraulic performance associated with the phase-change process need to be considered.

5.2   Conventional Heat Transfer Fluids

In addition to the FOM discussed in Section 2, the choice of fluid for solar thermal applications is governed by many other practical considerations. The commonly available heat transfer fluids for solar thermal power plants are summarized in Table 5-1. For large scale solar thermal plants (*e.g.*, SEGS plants), synthetic or mineral oils have been the most common heat transfer fluid due to their high stability over a relatively wide temperature range (15°C – 400°C) [82, 83]. The use of molten salts that are stable at higher temperatures (> 400°C) has also been suggested by previous studies to enhance the power cycle efficiency [84].

79

Table 5-1 | Conventional and potential heat transfer fluids for solar collector fields.

		Fluid
Oils	Synthetic	Therminol® VP-1[85]
	Mineral	Caloria HT 43 [76]
Molten salts	Nitrates	Hitec® [86], Hitec® Solar Salt [86]
	Chlorides	KCl-MgCl$_2$ [87]
	Fluorides	LiF-NaF-KF (FLiNaK) [87]
Other liquids		Mercury [24]
		Water [88]
Pressurized gases		Water vapor (30 - 100 bar) [88]
		Air (30-100 bar) [89]

Figure 5-2 shows the thermophysical properties and the FOM of the various heat transfer fluids listed in Table 5-1. Volumetric heat capacity (Figure 5-2a), thermal conductivity (Figure 5-2b), and dynamic viscosity (Figure 5-2c) values are shown, and the combined effects of these properties (Figure 5-2d) are evaluated using the FOM discussed below.

(a)

Volumetric Heat Capacity (J/m³K)

Air [16]
100 bar
60 bar
30 bar

VP-1 [10]
Caloria HT [1]
Hitec [11]
Solar salt [12]
KCl-MgCl₂ [13]
FLiNaK [13]
Mercury [14]
Water [15]

Water-vapor [15]
100 bar
60 bar
30 bar

Temperature (K)

(b)

Viscosity (Pa·s)

Temperature (K)
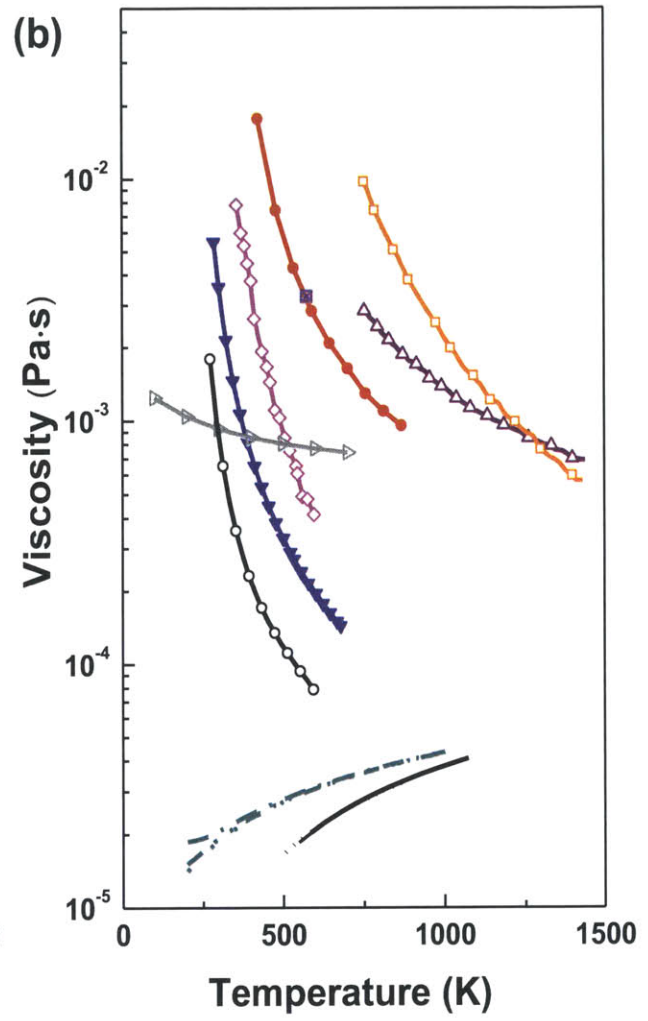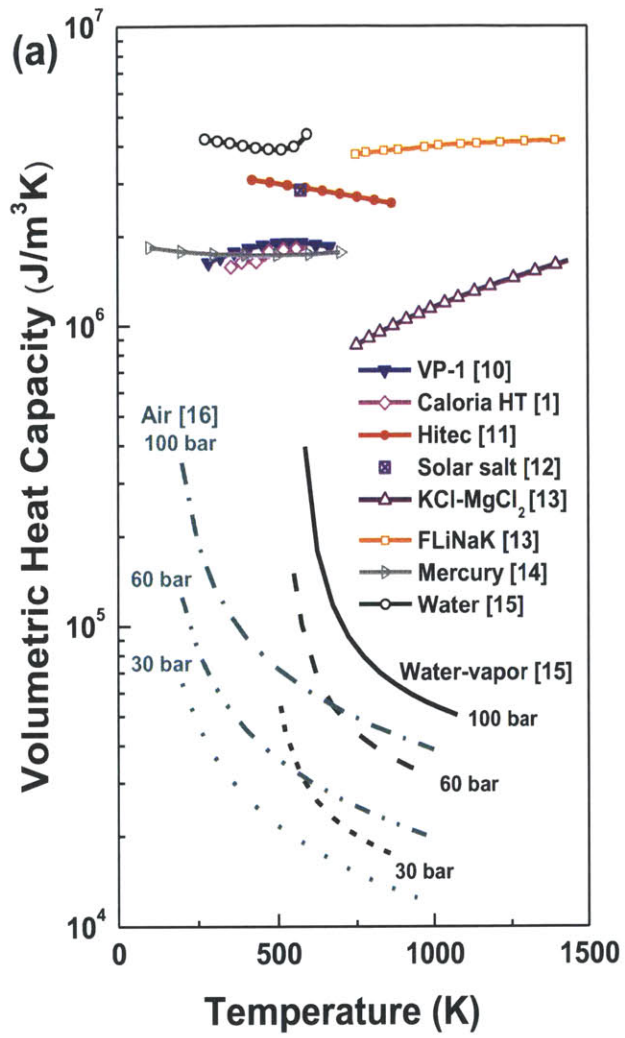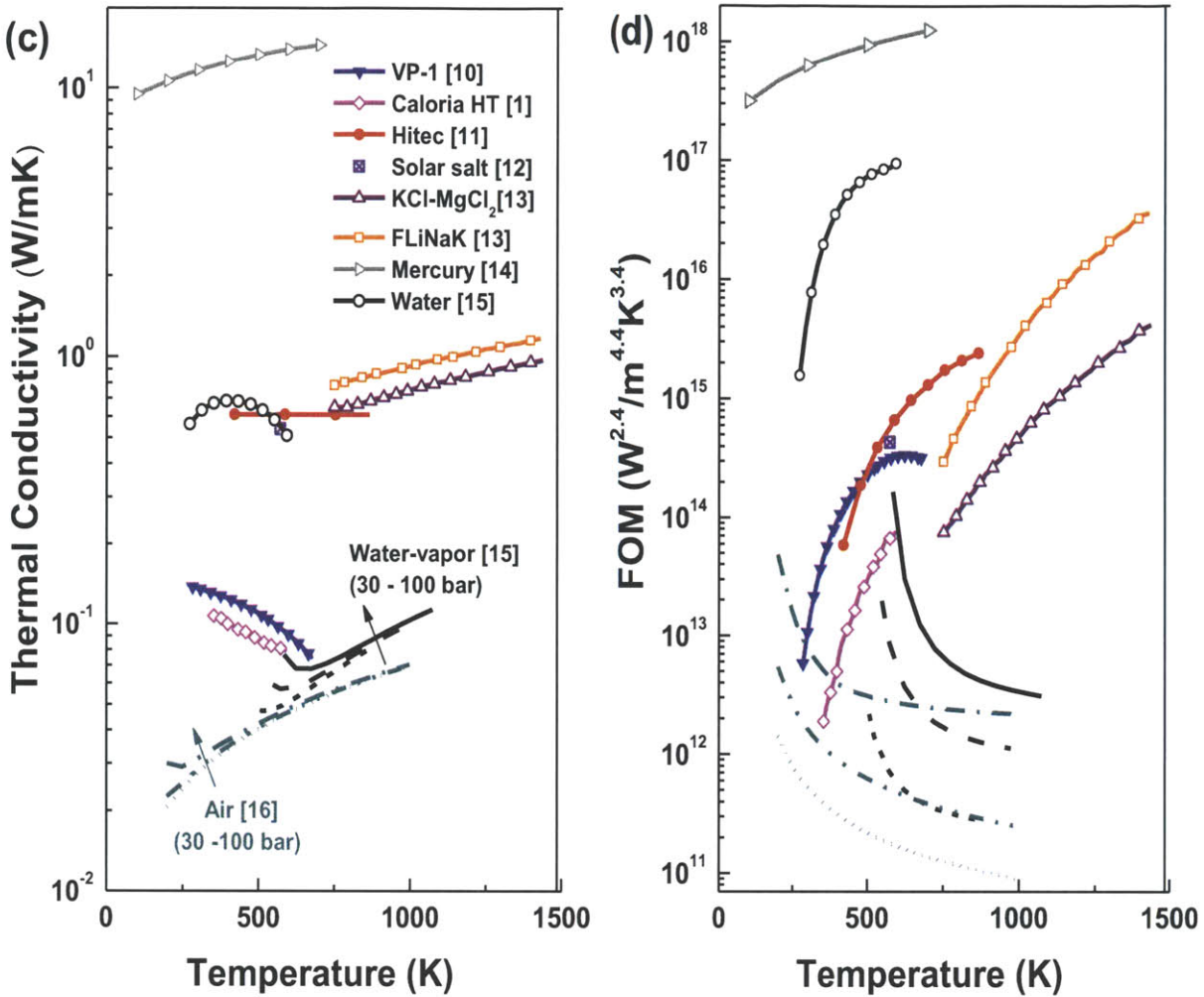
Figure 5-2 | Thermophysical properties and FOM of heat transfer fluids.
(a) volumetric heat capacity, (b) dynamic viscosity, (c) thermal conductivity, (d) figure of merit (FOM).
$P_l = P_{sat}(T)$ and $P_g = 30 - 100$ bar.

Between the two types of oils, the synthetic oil performs better than the mineral oil due to its higher thermal conductivity and lower viscosity. Therminol® VP-1 has been the most common heat transfer fluid used in parabolic trough solar plants; however, its modest thermal breakdown temperature (~400°C) limits the efficiency of power cycles [83].

Between the oils and the salts, the molten salts have a higher FOM due to their higher volumetric heat capacity and thermal conductivity. At 325°C, for example, the FOM of nitrate salts (*e.g.*, Hitec®, Hitec® Solar Salt) is approximately two and nine times higher than the synthetic (*e.g.*, Therminol® VP-1) and mineral oil (*e.g.*, Caloria HT 43), respectively. Fluoride molten salts (*e.g.*, FLiNaK) have higher energy density and thermal conductivity than the nitrate ones, but the

higher viscosity limits their overall benefit. At high temperatures (> 525°C), the FOM of fluoride salts becomes larger than that of the nitrate salts due to the decrease in viscosity. However, the freezing point (> 425°C) is too high for existing solar thermal applications.

Molten salts have a potential to improve both the collector field and power cycle efficiencies due to their higher FOM compared with the oil-based heat transfer fluids. Moreover, molten salts are cheaper and environmentally less harmful than the oils. However, the high freezing point of the molten salts requires a freeze protection method in the solar field, which increases the operation and maintenance cost. For example, Hitec® freezes at ~140°C [86] while the synthetic oil usually freezes at ~15°C. To further reduce the freezing point of molten salts, recent studies have introduced advanced molten salt mixtures based on nitrate/nitrite anions [90]. Details of the recent progress in multi-component molten salts and ionic liquids will be discussed in 5.3.1 and 5.3.2.

Water and water-vapor are also promising heat transfer fluids for solar thermal plants, as shown in Figure 5-2d. In fact, alternative solar thermal plants using water and water-vapor as heat transfer fluids have been successfully operated for more than 4000 hours through the DISS project [91]. The alternative system, the so-called direct steam generation (DSG) solar thermal plants

Gases such as air are also promising heat transfer fluids due to their extremely low viscosity and cost. The volumetric heat capacity can be increased by increasing the operating pressure. However, the increase in working pressure may raise the cost of solar field piping.

5.2.1   Operating temperature

Figure 5-2d shows that the performance of heat transfer fluids is strongly temperature-dependent. For the presented liquids, the FOM rapidly increases as the temperature increases mainly due to the rapid decrease in viscosity (Figure 5-2b). For the gases, the trend is reversed; the FOM decreases with temperature, primarily because the volumetric capacity decreases rapidly as the temperature increases (Figure 5-2a).

The operating temperature also affects the power cycle efficiency since an increase in fluid outlet temperature increases the Rankine cycle efficiency of steam turbines. For typical concentrated solar power (CSP) plant designs, power cycle efficiency increases from 37.6% to 40% by increasing the solar field fluid outlet temperature from ~390°C to ~450°C [84].

Despite the benefits of increasing the operating temperature, the thermal stability of fluids and selective coatings on collector tubes sets an upper limit on the fluid temperature. The Luz System Three (LS-3) collector tube, utilized in the most recent SEGS and DISS plants, is only stable up to ~400°C [92, 93]. Two new selective coatings with interface stacks and cermet layers stable up to ~450°C were recently developed by CIEMAT within the DISS project but have not been applied yet [91]. Therefore, the operating temperature of fluids should be carefully determined considering the entire system, including the collector tubes, the power block steam turbine, and the fluid itself.

5.2.2 Safety and reliability

Other characteristics of the heat transfer fluids including flammability, toxicity and corrosiveness also need to be considered for the safe and reliable operation of solar plants. For the collector fields using highly flammable heat transfer fluids such as oils, fire extinguishing systems are required to protect the solar plants against fire hazards. In fact, the first SEGS plant using mineral oil was destroyed in 1999 by a fire. In subsequent SEGS plants, mineral oil was replaced by less flammable synthetic oil [94]. Even though mercury has a very high FOM (see Figure 2d), the use of mercury is not suggested because mercury and most of its compounds are extremely toxic. For solar plants using molten salts, the collector tubes need to be corrosion resistant. At elevated temperature (~450°C), molten salts may corrode some metals including steel, stainless steels and copper. The corrosion rates of various metals by nitrate salts (*e.g.*, Hitec®) are provided by manufacturers [86].

The performance of various heat transfer fluids is evaluated for solar thermal applications based on the individual thermophysical properties and the new FOM. The comparison shows that molten salts should perform better than oil-based fluids. However, several technical issues including freeze protection and the selection of proper materials for piping need to be considered to successfully apply the molten salts to large scale solar plants. Pressurized gases including air and water vapor are also promising economical heat transfer fluids but the levelized electricity cost (LEC) should be investigated considering the high pressure requirement in the collector tube.

5.3 Ionic Liquids and Melts

Compared to synthetic oils which are commonly used in parabolic trough applications, molten salts operate at higher temperatures, have lower vapor pressures, are more environmentally-

friendly and less expensive. Recent feasibility studies have shown that molten salts, serving as both a heat transfer fluid and a storage medium, have the potential to improve performance and lower the overall costs of parabolic trough solar plants [84]. It is envisioned that excess molten salt supplied by the collector loop during periods of high-irradiation can be stored in an insulated tank and later used for power production during periods of low-irradiation (*e.g.,* extended periods of cloud cover, nighttime, *etc.*). Moreover, the ability to increase the operating temperature (> 450°C) of the system translates into more efficient thermal-to-electrical conversion in the power cycle [84, 90, 95].

The feasibility of molten salts as heat transfer fluids and storage media has been successfully demonstrated in CSP applications with central receiver designs. Nevertheless, the primary issue preventing the widespread use of molten salt is their relatively high freezing point. During periods of limited or no solar irradiation, the ambient temperature can drop well below 25°C resulting in solidification of the molten salts which ultimately leads to damage of the piping and increased costs associated with thawing [90]. Freeze prevention mechanisms, including overnight circulation of the fluid, auxiliary heaters and heat trace wire, are needed in such systems [84].

To eliminate the solidification problems, current research efforts aim to lower the freezing point of ionic fluids. For this purpose, ionic liquids and multi-component salts have received a significant amount of interest. The difference between ionic liquids and ionic melts (*i.e.,* molten salts) is subtle: ionic liquids, by definition, have freezing point temperatures below the boiling point of water. Furthermore, ionic liquids typically have organic cations, while molten salts are composed of inorganic anions and cations [96]. The focus of this section is to review and discuss recent advances in both ionic liquids and multi-component salts for use in solar thermal applications, most of which have targeted lowering the freezing point and extending the working range of the fluid.

5.3.1   Multi-component salts

The melting point of binary and ternary mixtures is significantly lower as compared to the pure components for entropic reasons. In a simple binary mixture system, a particular composition of the two components (*i.e.,* eutectic point) will minimize the freezing point (or liquidus temperature). For this reason, salts currently used in solar thermal applications such as Hitec®

and Hitec® Solar Salt are eutectic binary or ternary mixtures. Liquidus temperatures as low as 108°C for eutectic mixtures of nitrate/nitrite anions with two alkaline cations have been reported [97].

Recent work has focused on extending this concept by investigating multi-component salt mixtures. In such systems, the phase diagram can be significantly more complex and harder to predict [98]; hence, a combinatorial experimental approach has been adopted to determine the composition with the lowest melting point.

As shown in the phase diagram in Figure 5-3, Cordaro *et al.* investigated a mixture of cations of sodium, potassium and lithium with a fixed 1:1 molar ratio of nitrate/nitrite anions [90]. They were not able to find a eutectic or near-eutectic point, yet they obtained liquidus temperatures below 80°C. By sampling aliquots of the liquid phase during freezing and experimentally determining their composition, a liquidus temperature near 70–75°C for a Li:K:Na (30%:50%:20%) salt with a nitrate/nitrite ratio of approximately 0.56 was obtained.
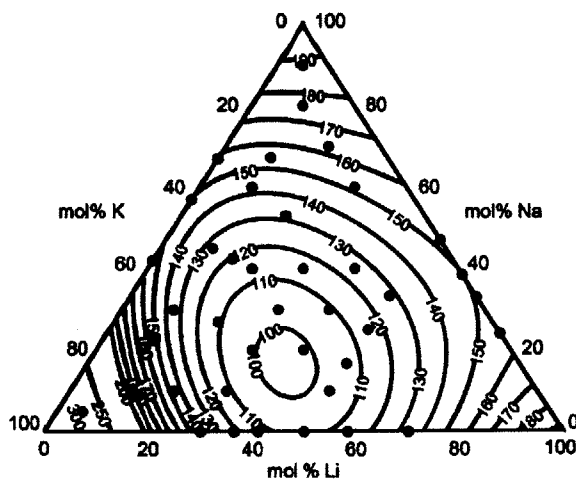
Figure 5-3 | Phase diagram for Li:Na:K mixture with nitrate/nitrite (1:1 molar ratio).
(Dots: experimental data; Lines: mathematically interpolated.) From [90] (Copyright 2011, ASME).

Bradshaw *et al.* [98] investigated nitrate/nitrite systems with sodium, potassium, lithium and calcium cations. Calcium nitrate was found to lower the liquidus temperature moderately and significantly increase the viscosity of the melt. Lithium nitrate, on the other hand, was found to reduce the liquidus temperature significantly and have a weak effect on viscosity.

The thermal stability of nitrate/nitrite multi-component salts is expected to be limited by the oxidation of nitrite into nitrate. As nitrate is formed, the mixture shifts away from the eutectic

point elevating the freezing point such that insoluble products may form in the heat transfer fluid which clog the valves and pipes [98]. An inert atmosphere can prevent this problem since the nitrite/nitrate reaction is governed by the partial pressure of oxygen in contact with the molten salts. The thermal stability of nitrate/nitrite multi-component salts in air is expected to be similar to existing nitrate/nitrite salts (*i.e.*, ~500°C). Thermal decomposition of these salts at high temperatures yielding different types of oxides is also a concern since soluble oxide ions can increase the amount of corrosion [98].

A limited amount of research currently exists on the thermophysical properties and heat transfer performance of low melting point multi-component salt mixtures. Moreover, the cost of lithium containing salts is high; low-cost substitutes for lithium need to be investigated if the fluid is to be used as a thermal storage medium.

5.3.2   Ionic liquids

In contrast to molten salt mixtures where the freezing point is decreased via the addition of salts with small and polarizing inorganic cations (*e.g.*, Li), ionic liquids have large and asymmetrical organic cations [99]. Although other cations have been synthesized and used in ionic liquids, the imidazolium cation ([im]) and its derivatives have been prevalent in research because of their low melting points which are attributed to the asymmetrical nature of [im] [99]. Moreover, properties of ionic liquids (such as the melting point) can be tuned through modification of the chemical group attached to the basic [im] structure [95]; examples of which are shown in Figure 5-4.
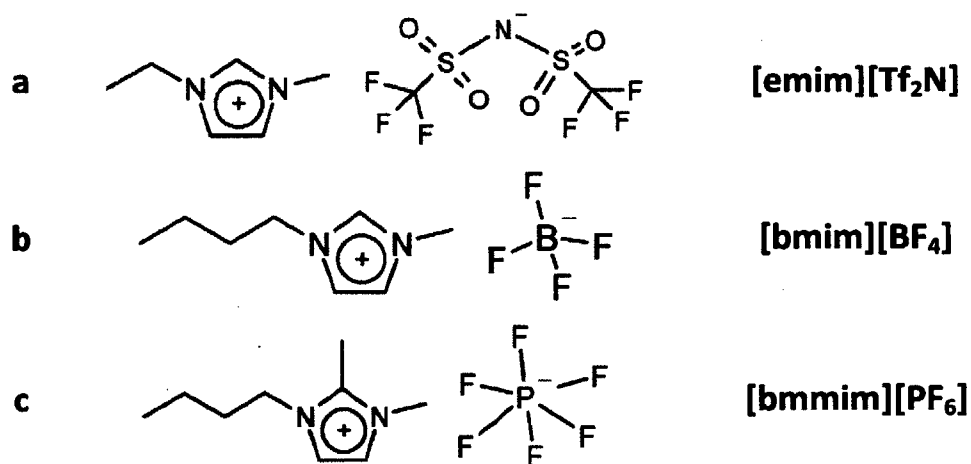
Figure 5-4 | Chemical structure of the following imidazolium-based ionic liquids.
a) 1-*n*-ethyl-3-methylimidazolium bis(trifluoromethylsulfonyl)imide, [emim][Tf₂N]; b) 1-*n*-butyl-3-methylimidazolium tetrafluoroborate, [bmim][BF₄]; c) 1-*n*-butyl-2,3-dimethylimidazolium hexafluorophosphate, [bmmim][PF₆]. Adapted from [100] (Copyright 2004, American Chemical Society).

Van Valkenburg studied several "common" [im]-based ionic liquids for use as HTFs in solar thermal applications [96]: 1-methyl-3-ethylimidazolium tetrafluoroborate ([emim][BF₄]), 1-methyl-3-butylimidazolium tetrafluoroborate ([bmim][BF₄]), and 1,2-dimethyl-3-propylimidazolium bis(trifluorosulfonyl)imide ([dmpi]Im). The thermophysical properties of these ionic liquids are summarized in Table 5-2. The thermal conductivity, heat capacity and density of the three ionic liquids are comparable and similar to the properties of synthetic oils such as Therminol® VP-1; the viscosity of the ionic liquids, however, is at least an order of magnitude higher.

When evaluated on the basis of the FOM discussed in Sections 1 and 2, the heat transfer performance of the three [im]-based ionic liquids in Table 5-2 is relatively poor ($\sim10^{11}$-10^{12}) and comparable to low-pressure air or water-vapor. The increased viscosity severely limits the applicability of these ionic liquids, especially in parabolic trough applications where the pressure drop is a concern because of the relatively long solar collector loop.

Table 5-2 | Summary of thermophysical properties and temperature ranges for three ionic liquids [96].

Property	Ionic Liquids		
	[emim][BF₄]	[bmim][BF₄]	[dmpi]Im

Density, 60° C (kgm^{-3})	1253	1175	1421
Heat capacity, 100° C (Jkg^{-1}K^{-1})	1281	1659	1196
Thermal conductivity, 25°C (Wm^{-1}K^{-1})	0.200	0.186	0.131
Dynamic viscosity, 25°C (kgm^{-1}s^{-1})	0.036	0.120	0.090
$FOM = \dfrac{\rho^{2.0} c_p^{1.6} k^{1.8}}{\mu^{1.4}}$	8.5 (10^{11})	1.8 (10^{11})	1.3 (10^{11})
Freezing point (°C)	14.4	-87.4	11.3
Thermal decomposition onset (°C)	446	424	457

The ~50°C higher onset of thermal decomposition for [emim][BF$_4$] compared to Therminol® VP-1 has the potential to increase efficiency in the power cycle and outweigh the cost of the increased pressure drop. Further studies on the feasibility of these and other ionic liquids are needed to confidently assess their applicability in CSP.

The temperature dependence of the thermophysical properties of ionic liquids has been reported by Van Valkenburg and others [96, 100-102]. In general, the heat capacity shows a weak dependence, while the thermal conductivity and density decrease slightly with increasing temperature. Chen et al. [102] determined that the viscosity of an imidazolium-based ionic fluid decreases with increasing temperature following an Arrhenius-like behavior; furthermore, their experiments show that the ionic fluid is Newtonian.

Few heat transfer experiments using ionic liquids as the heat transfer fluid exist in literature. Chen et al. [102] studied the convective heat transfer behavior of an [im]-based ionic fluid under laminar flow conditions. The thermal entrance length for the ionic fluid was determined to be very large compared to that of water because of the relatively low thermal conductivity and high viscosity of the ionic fluid. The convective heat transfer coefficient over the developing region correlated well with analytical predictions for their geometry (Shah's equation) but it was significantly lower than that for water under the same conditions. Thus, as predicted by the individually measured properties, the heat transfer performance of many ionic liquids is limited.

The difference between ionic fluids and ionic melts is becoming less distinct as current research using inorganic multi-component mixtures of salts is successfully lowering the liquidus temperature below 100°C. Research in both areas of ionic liquids and ionic melts will most likely converge toward multi-component systems optimized for heat transfer performance and a wide region of thermal stability. Cost-effective ionic liquids with comparable viscosities to synthetic oils and temperature stability approaching 500°C need to be developed. Similarly, multi-component salts are promising for solar parabolic trough applications but lower cost alternatives to lithium nitrate need to be incorporated.

5.4   Nanofluids

In order to enhance the thermophysical properties of common heat transfer fluids, researchers have investigated colloids where solid particles are suspended in a liquid. The basic idea originates from the assumption that the characteristic benefits of two or more components can be combined to achieve the desired properties. In the case of solid-liquid composites for example, the addition of solid particles was proposed to increase the effective thermal conductivity and storage density. However, it was found that solid-liquid composites with larger particles lead to problems with sedimentation, clogging, and erosion in heat transfer applications. Suspensions of submicron-sized solid particles, on the other hand, promise to alleviate some of the aforementioned issues and have recently received a significant amount of attention in literature.

This section focuses on suspensions of nanoparticles (i.e., nanofluids) including solid nanoparticles and phase-change nanoparticles. Nanofluids have generated much interest in the heat transfer community where order of magnitude thermal conductivity enhancements were experimentally obtained. Recent advances reported in literature regarding nanofluids are discussed and technological issues that need to be overcome before they can be successfully adopted in solar thermal applications are identified. The proposed mechanisms explaining the thermophysical properties of nanofluids are also discussed.

Nanofluids are primarily evaluated based on their performance under turbulent forced convection since those are the conditions most commonly encountered in existing solar collectors. Heat transfer enhancements deviating from predictions based on empirical correlations are discussed.

The dual-use potential of nanofluids in solar thermal applications is also explored, where in addition to being heat transfer fluids, they can act as volumetric solar receivers, replacing

selective surface coatings by directly absorbing solar radiation, or direct storage media, eliminating the need for an intermediate thermal storage medium. These dual-use applications have the potential of increasing the efficiency and reducing the cost of existing systems by eliminating the need for a specific component or loop.

5.4.1   Thermophysical properties

This subsection reviews the thermal conductivity, viscosity, heat capacity and radiative properties of nanofluids. The properties of solid-liquid composites are conventionally understood using effective medium theories or mixing rule formulations; however, nanofluids have shown behavior not captured by these classical approaches, generating much interest in the research community. Our discussion will focus on currently well-accepted mechanisms explaining the behavior of nanofluids since research in this area remains active and sometimes controversial.

Thermal Conductivity

Effective medium theory is a relatively simple approach used to describe transport properties (*e.g.*, thermal conductivity) of composites. In the limit that the thermal conductivity of the solid particles (k_p) is much higher than that of the basefluid (k_f), the effective conductivity k_{eff} of dilute nanofluids can approximately be described by

$$5\text{-}14 \qquad\qquad \frac{k_{eff}}{k_f} \approx 1 + C_k \phi,$$

where C_k is the thermal conductivity enhancement coefficient and ϕ is the volume fraction of the solid particles. For a dilute suspension ($\phi < 0.03$) of non-interacting spherical particles, Maxwell obtained that $C_k = 3$ [103]. Additional effects have been incorporated to generalize the effective medium theory such as particle shape and the interfacial resistance between the solid and the basefluid. Descriptions of these effects can be found in past reviews of nanofluids [104-107]. Many investigators have reported experimental data not explained by effective medium theory (EMT) and proposed physical mechanisms beyond EMT to explain the discrepancies and "anomalous" effects [108]. The dominant mechanisms have not been identified primarily due to a lack of agreement between the experimental results of different investigators, however, the main mechanisms discussed in literature are as follows [104]:

91

i) **Interfacial layering**: Ordering of basefluid molecules at the particle interface and formation of a high-conductivity solid-like interfacial layer (Figure 5-5a). An *in situ* study of an alumina-aluminum interface using a high-resolution transmission electron microscope provides experimental evidence of ordering of the liquid molecules at a crystal interface (*i.e.*, interfacial layer), even at elevated temperatures (~750 °C) [109]. Kaplan and Kauffmann [110] reviewed both theoretical and experimental studies of liquid molecule ordering adjacent to crystalline solids. Gerardi *et al.* [111] observed layering of water (forming a ~1.4 nm thick layer) on alumina particles using NMR, but they did not measure an anomalous conductivity enhancement.

ii) **Agglomeration**: Formation of particle clusters within the basefluid leading to increased effective solid fraction and preferential heat flow through the highly conductive clusters (Figure 5-5b). Timofeeva *et al.* [112] found that the thermal conductivity was not significantly affected by aggregation, whereas, Wamkam *et al.* [112, 113] observed a significant enhancement of thermal conductivities (>20%) in 3 wt % suspensions when aggregation was most pronounced. Both groups suggest that the reason for the discrepancy lies in the nature and amount of the agglomeration: strong aggregates, which could lead to k_{eff} enhancement; and aggregate-like ensembles, which occur due to weak repulsive forces between particles and are unlikely to enhance k_{eff} because of the solid-liquid-solid interfacial resistance. The effect of agglomeration will be discussed further in the next subsection as it plays an important role in the effective viscosity of nanofluids; more work needs to be done to quantify the effect of agglomeration on thermal conductivity.
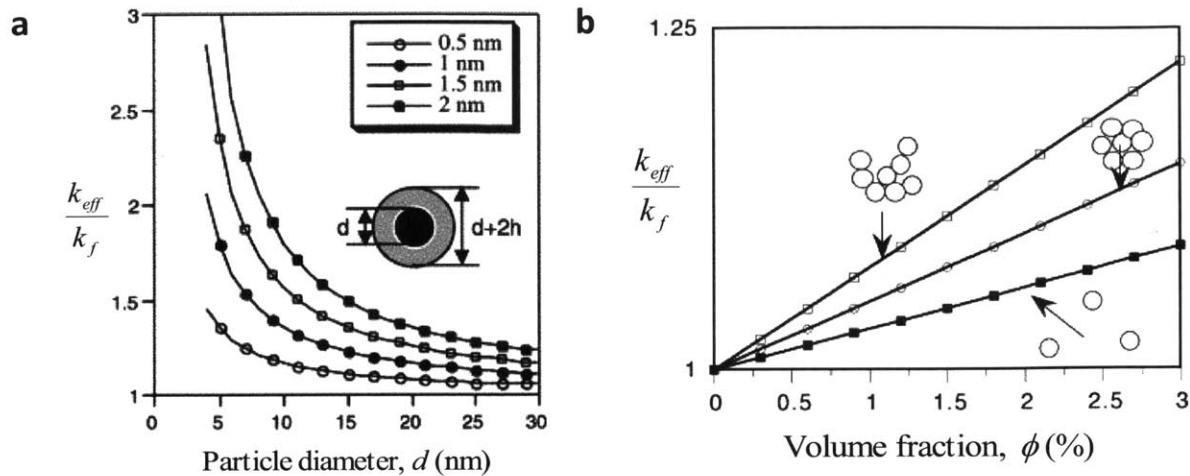
Figure 5-5 | Mechanisms proposed to explain thermal conductivity enhancement in nanofluids. a) Formation of a highly ordered interfacial layer (h) composed of basefluid molecules around a nanoparticle (diameter, d). Adapted from [114] (Copyright 2002, Elsevier); b) Formation of highly conductive aggregates leading to an increased effective solid volume fraction compared to ϕ of particles (solid squares: well-dispersed particles, circles: packed clusters (60 vol.% particles), open squares: loosely packed clusters (40 vol.% particles). Adapted from [104] (Copyright 2005, Elsevier).

A recent international collaboration (International Nanofluid Property Benchmark Exercise, or INPBE) was coordinated in order to build a consensus in the area. The INPBE had over 30 organizations worldwide measure the thermal conductivity of identical nanofluid samples using several different experimental approaches [115]. Experimental data collected for the INPBE is in good agreement (< 20% error) with the generalized form of the EMT [116] which includes the effects of particle shape and interfacial resistance. A drawback of the generalized EMT formulation, however, is that it has little predictive power since the magnitude of the interfacial resistance (which is not readily available) must be known. Although, the INPBE study observed no anomalous thermal conductivity enhancements and found that proposed theoretical mechanisms such as interfacial layering and agglomeration were not needed to explain the data [115], there is a still a debate as to which mechanisms are negligible and which ones can be exploited for thermal conductivity enhancements.

At present, the generalized form of the EMT [116] is recommended. Using this formulation, the thermal conductivity enhancement in nanofluids simply increases with increasing particle volume fraction, thermal conductivity (k_p) and aspect ratio. Further systematic studies with explicit control and characterization of the interfacial effects need to be performed to validate any mechanisms beyond the generalized EMT.

93

Viscosity

Similar to thermal conductivity (Eq. 6-14), the effective viscosity (μ_{eff}) of nanofluids depends strongly on the volume fraction of nanoparticles in suspension and can be approximately represented by [117]

$$5\text{-}15 \qquad\qquad \frac{\mu_{eff}}{\mu_f} \approx 1 + C_\mu \phi \ .$$

Einstein predicted that for a suspension of non-interacting, hard, uncharged, spherical particles, the coefficient of viscosity enhancement (C_μ) is 2.5 [118]. For non-spherical particles, limitations to rotational and translational Brownian motions lead to higher viscosity. In this case, the coefficient of viscosity enhancement scales with the aspect ratio [117]. In dilute suspensions ($\phi < 0.03$), these formulation were found to work well for particles sizes between 3 and 300 µm, but for suspensions of particles below 500 nm, the experimental viscosity exceeds predictions [119].

An INPBE study on viscosity determined that the measured viscosity dependence on the particle volume fraction for both spherical and non-spherical particles is roughly ten-times larger than predicted (C_μ was 23.4 for spherical particles, and 70.8 for rod-shaped particles) [117]. A slightly lower dependence on ϕ was observed in other studies ($C_\mu \approx 4\text{-}16$). Therefore, models used for micron-size particle suspensions underestimate the viscosity of nanofluids.

The drastically increased viscosity in nanofluids most likely occurs because basefluid molecules are trapped around particles and inside particle clusters leading to an increased effective volume fraction of the solid phase [113, 117, 120]. Electrical double layers and particle-particle interactions govern the formation of effective excluded volumes, as discussed below.

An electrical double layer forms around particles because they typically acquire a surface charge when placed in a liquid. Investigators suggest that the increase in viscosity is proportional to the double layer thickness because molecules in the double layer increase the effective volume of a particle [112, 119-121]. This effective excluded volume effect can play a significant role in small nanoparticles because of their large surface-to-volume ratio.

Agglomeration in nanoparticle suspensions is governed by particle-particle interactions. These interactions are understood as a balance between attractive Van der Waals forces and repulsive

electrostatic forces between particles of the same charge. As shown in Figure 5-6, the balance of these forces can lead to the formation of an energy barrier which reduces contact and aggregation of particles. The influence of surface charge, pH, surfactant additives, particle morphology, and basefluid properties on the particle-particle interactions is discussed in more detail below.
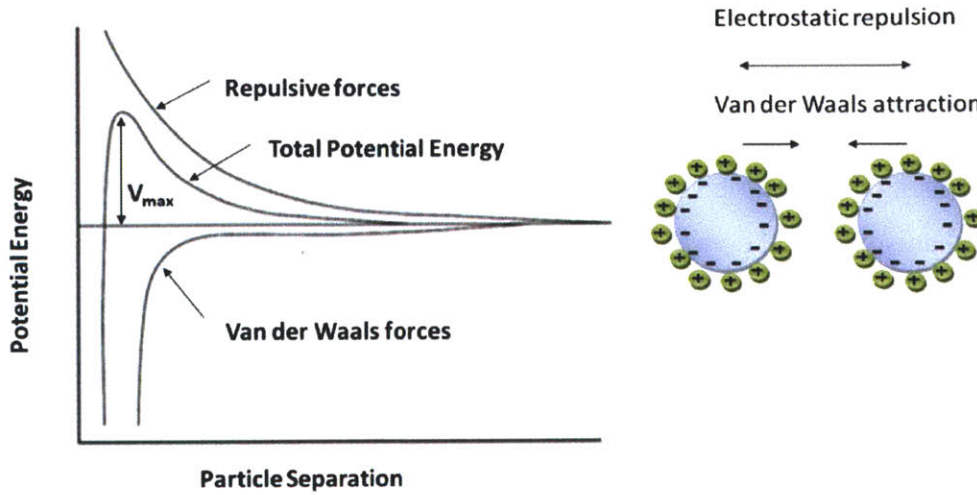
Figure 5-6 | Forces between suspended nanoparticles.
Schematic diagram of the variation in free energy with increasing particle separation, showing a balance between repulsive and attractive forces. From [113] (Copyright 2011, American Institute of Physics).

i) **pH:** Adjusting the pH of the nanofluid such that it is further from its isoelectric point (IEP) increases the surface charge of particles and ultimately the repulsive forces, as understood through DLVO theory [113, 122]. Timofeeva *et al.* showed that the viscosity of alumina and SiC nanofluids can be decreased by 31% [112] and by 34% [119], respectively, by controlling the pH of the suspension; while, Wamkam *et al.* [113] lowered the viscosity enhancement ratio from 66% to 20% by changing the pH in ZrO_2 suspensions from 8 to 10 (IEP at pH $\approx$ 6.2). Both results are explained by the fact that increasing the repulsive forces results in less aggregated suspensions with lower viscosity.

ii) **Surfactant additives:** Surfactants are typically ligands that adsorb to sites on the nanoparticle surface and impact the repulsive forces between the particles. Surfactants may provide both electrostatic and steric stabilization [121] and improve the viscosity of the suspension. Nevertheless, surfactants are not widely used in solar thermal heat transfer applications because large amounts of surfactant are needed to cover the total

95

nanoparticle interfacial area and the thermal stability of surfactants at elevated temperatures (>200 °C) has not yet been demonstrated.

iii) **Particle morphology:** the magnitude of the energy barrier preventing nanoparticles from aggregating can be enhanced by increasing the particle size (attractive forces scale with the particle diameter while repulsive forces scale with the diameter squared) [122].

Despite past efforts, the viscosity of nanofluids has yet to be fully connected to DLVO theory and explained using quantitative and predictive models. For agglomeration to be accepted as the dominant mechanism, then the viscosity of nanofluids should decrease with increasing repulsion forces between particles and increasing particle size. As discussed, repulsive forces between particles can be tuned using the pH of the suspension. However, practical. limitations on pH control and particle size exist such as corrosion and sedimentation, respectively.

Volumetric Heat Capacity

In general, the heat capacity and density of solid-liquid nanofluids is well-predicted using a simple property mixing rule and no dependence on the particle morphology has been observed [119]. The specific heat of nanofluids typically increases or decreases with increasing particle loading depending on whether the nanoparticles have a higher or lower capacity relative to the basefluid [25, 123]. However, a recent study by Shin *et al.* [124] reported an anomalously high increase in specific heat capacity (14.5%) of a suspension of silica nanoparticles (1 wt.%) in a high-temperature alkali salt eutectic. The mechanisms suggested to explain the increased heat capacity are similar to the mechanisms suggested for thermal conductivity enhancements; namely, the existence of a semi-solid interfacial layer. The anomalous results have not been confirmed by other investigators. Nevertheless, if the existence of a substantial interfacial layer with distinct thermophysical properties can be experimentally verified, the effect can be significant in nanofluids because of the high surface-to-volume ratio of nanoparticles.

A related but distinct approach to enhancing the specific heat of heat transfer fluids has been to suspend phase-change particles in the basefluid [125]. Micron-sized encapsulated phase-change materials (mePCMs) are most commonly composed of a wax or organic inner core and a polymer-based outer shell; paraffin is the most common inner core material because of its relatively high latent heat, low vapor pressure, negligible supercooling, and chemical stability

[25]. When suspended in a heat transfer fluid, PCMs serve to increase the effective heat capacity of a fluid over a relatively small temperature range as the inner core undergoes melting or phase-change. Unlike the study of nanofluids, thermophysical properties of mePCMs are well-described through a conventional understanding of mixtures. They have been successfully commercialized in specialized thermal management applications; however, in convective heat transfer applications, mePCM suspensions suffer from problems related to low thermal conductivity [25], damage of the encapsulation material [126], clogging, and increased pumping costs. At present, they have not been successfully integrated in mid or high-temperature solar thermal applications because of these drawbacks and also because they are limited to low temperatures.

Recent work on phase-change material suspensions has aimed to make nano-sized PCM particles to circumvent the practical issues associated with micro-encapsulated PCMs. Nano-encapsulated PCMs (nePCMs) have been synthesized and characterized [126]; however, since the encapsulation layer scales with the surface area of the particles, it constitutes a significant fraction of the mass which limits their effectiveness. To avoid the issues with encapsulation, Han et al. [127] synthesized an encapsulation free, suspension of phase-changing indium (melting temperature, 157 °C) using a dispersant to stabilize the suspensions and reduce coagulation. The use of encapsulation free phase-change nanofluids to simultaneously enhance thermal conductivity and effective heat capacity is an interesting approach but practical issues with fluid stability and lifetime remain a concern.

Radiative Properties

The radiative properties of nanofluids are dependent on both the basefluid and the nanoparticles. Potentially serving as basefluids, certain heat transfer fluids were found to be highly transparent for wavelengths in the solar spectrum such as molten salts [128], water, ethylene glycol, propylene glycol and Therminol® VP-1 [129]. Nanoparticles, on the other hand, can exhibit strong and tunable absorption peaks. As a first order approximation, investigators have proposed that the nanofluid absorption coefficient can be described using a simple addition of the basefluid absorption coefficient and that of the particles [130].

The radiative properties of nanoparticles are in principle well-described by Mie theory [131] when the surrounding is non-absorbing and the volume fraction is low ($\phi \ll 0.01$). A

nanoparticle in a dielectric medium exhibits a resonant absorption peak when the frequency of the incoming light coincides with a plasmon resonant mode (*i.e.,* collective oscillation free electrons) [132]. If the nanoparticle is indeed much smaller than the wavelength of incident light, absorption due to the particle is much stronger than scattering and is proportional to the volume of the particle [131, 133]. Hu *et al.* [134] extended the analysis by Bohren and Huffman [131] to describe nanoparticles in an absorbing medium by treating the optical constant of the host medium (*i.e.,* basefluid) as a complex number. Recently a quantum mechanical simulation has been used to validate that this description is applicable down to 10 nm in silver nanoparticles [135] as long as the optical properties of the bulk solid are modified to account for electron scattering by the interface when describing smaller nanoparticles. In metallic nanoparticles, the dominant resonant absorption peak typically occurs in the visible spectrum but can be modified by varying the particle size, shape or shell material. Cole *et al.* proposed that a combination of as little as three metallic nanoparticles types can selectively absorb the majority of the solar spectrum [136]; in this case, the optimized composition of nanoparticles was found to contain nanospheres and nanoshells ranging from 32 nm to 58 nm.

Plasmon resonant absorption peaks for nanoparticles in suspension have been experimentally demonstrated for a range of nanoparticle materials, shapes and sizes [137]. The experimental results match well with theory as long as the particles are sufficiently dispersed such that they can be treated as isolated. Recently, however, Taylor *et al.* [130] did not observe plasmon peaks using silver nanoparticles and attributed this result in part to the presence of impurities and particle aggregates leading to increased scattering. Thus, in order for nanofluids to maintain the sharp absorption peaks and have good absorption characteristics with solar light, care must be taken to avoid agglomeration; nevertheless, more research in this area is required. Moreover, the infrared properties of high temperature pure heat transfer fluids and nanofluids, critical for understanding their thermal emissivity, have not yet been fully characterized. The application for solar absorbing nanofluids will be described further in the following section.

5.4.2   Applications

Thus far this section has focused on recent experiments and understanding the thermophysical properties of nanofluids. For heat transfer applications, it is important to consider how those properties couple together in particular applications. The heat transfer performance of nanofluids

will primarily be evaluated for forced convection in solar thermal systems. Furthermore, this section considers direct absorption of solar radiation by the nanofluids for concentrated solar systems using volumetric receivers.

Forced Convection Heat Transfer

In convective heat transfer, the thermal performance of the nanofluid depends not only on the thermal conductivity but also on the density, viscosity, heat capacity and other dynamic mechanisms.

Investigators have shown that the heat transfer enhancements (compared to the pure basefluid) under turbulent forced flow conditions are typically between 15-45% [107]. However, Yu et al. [138] noticed that most of the previously reported heat transfer enhancements are based on a constant Re number such that the enhancement increases with increasing viscosity. When compared on the more practical basis of constant pumping power or constant velocity, only a small fraction (<30%) of studies report a forced convection heat transfer coefficient greater than that of their basefluid [138].

This result is not surprising since it was discussed in the Section 5.4.1 that the thermal conductivity of nanofluids does not significantly exceed the predictions of the generalized effective media theory, whereas the viscosity is typically 5-10 times the value suggested by existing models shown to apply for micro-particle suspensions. The viscosity increase typically surpasses any thermal conductivity enhancement such that the heat transfer performance of nanofluids in forced convection is commonly worse than for pure basefluids.

Enhancements in the heat transfer coefficient which cannot be predicted by traditional correlations such as Dittus-Boelter's (using the measured thermophysical properties of the nanofluids) are attributed to a variety of mechanisms. Buongiorno [139] theoretically investigated inertia, Brownian diffusion, thermophoresis, diffusiophoresis, Magnus effect, fluid drainage, and gravity as possible mechanisms which can produce a relative velocity between the particle and the fluid, and in turn, enhance heat transfer. The results show that only thermophoresis and Brownian diffusion were non-negligible slip mechanisms in nanofluids. An alternative explanation for the enhanced heat transfer was proposed: the viscosity of the nanofluid within the boundary layer may be significantly reduced because of the effect of the temperature gradient and thermophoresis, resulting in heat transfer enhancement [139].

Meanwhile, other studies suggest that the effects of thermophoresis and Brownian diffusion can also be neglected [119].

Timofeeva et al. [119] compared experimental heat transfer coefficient enhancements reported in literature [140-146] to a prediction using the Dittus-Boelter correlation based on the measured nanofluid properties (i.e., without additional dynamic mechanisms), as shown in Figure 5-7. It was found that most of the data is well-predicted by the correlation alone and noted that larger particle suspensions generally perform the best.
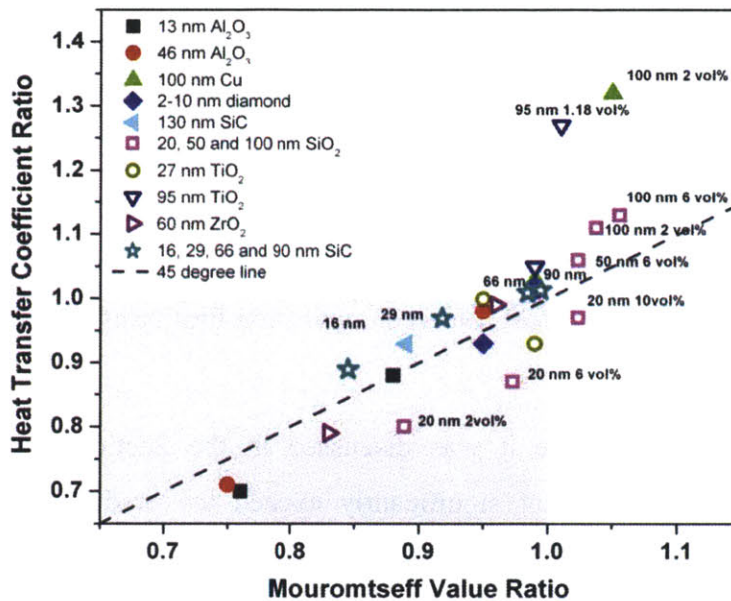
Figure 5-7 | Effect of nanoparticles on turbulent heat transfer.
Experimental enhancements of turbulent heat transfer coefficient (symbols) compared to enhancement predicted based on *Mo* number using nanofluid properties (dotted line). Grey region denotes property and performance deterioration compared to pure fluid. Adapted from [119] (Copyright 2010, IOP Science).

Other investigators [25] have studied hybrid suspensions of alumina nanoparticles and mePCMs to leverage the thermal conductivity enhancement of nanofluids and storage enhancements of PCMs. However, laminar forced convection experiments in a circular tube showed that the increase in friction factor exceeds enhancements in heat transfer since the viscosity of hybrid suspensions is anomalously high.

Presently, the best performing well-dispersed nanofluids are suspensions of larger spherical particles. As compared to small and non-spherical particles, larger spherical particles provide lower viscosity increases because of the decreased solid-liquid interfacial area [119] and reduced aggregation [147]. Practical limitations on the size of the particles are imposed by sedimentation

issues. Based on these factors, studies suggested that the optimized particle size is roughly ~130 nm (diameter) [147], but the exact size is application specific.

Future work in nanofluids could lead to superior heat transfer performance, however, coupling between the different thermophysical properties of nanofluids leading to performance tradeoffs needs to be tuned and optimized.

For forced convection in solar thermal applications, the observed viscosity decrease and thermal conductivity increase with temperature makes nanofluids promising for higher temperature applications [121]. However, further studies on the performance and material stability of nanofluids at high temperatures are needed. Moreover, further research needs to be conducted on additives to stabilize and lower the viscosity of nanofluids at high temperatures. Surfactants cannot currently withstand high temperatures, while using pH to prevent agglomeration may lead to corrosion issues.

Volumetric Receivers

Absorbing surfaces are most commonly used to convert solar energy from its radiative form into thermal energy in existing solar thermal technologies. However, at high levels of solar concentration, a large temperature difference between the absorber and the fluid arises depending on the effectiveness of the heat transfer. This temperature difference results in substantial emissive losses owing to the quartic dependence of thermal re-radiation on the absorber temperature. Alternatively, in a volumetric receiver design, concentrated solar radiation is directly absorbed and more uniformly distributed in the surrounding fluid, decreasing the temperature difference between the absorber and the fluid.

Nanofluid volumetric receivers, where nanoparticles in a liquid medium directly absorb solar radiation, promise increased performance over surface-based receivers by minimizing temperature differences between the absorber and the fluid. Several investigators have experimentally demonstrated that nanofluids are suitable solar absorbers [148, 149]. The radiative properties of the nanofluid can be tuned by adjusting the nanoparticle loading to achieve a balance between the distribution of heat throughout the fluid (*i.e.,* elimination of hotspots) and near-100% absorption of solar light, known as the optimum optical thickness [149]. Numerical studies showed that volumetric receivers are more efficient at higher levels of solar concentration and with increasing thickness of the absorbing nanofluid layer. As a result of

101

the high solar-to-thermal efficiencies at high temperatures, predicted optimum solar-to-electrical efficiencies of CSP plants utilizing nanofluid volumetric receivers exceed 35% [149]. From a practical standpoint, absorbing nanofluids are best suited for grounded solar receivers with integrated storage where a "reflective tower" [150] or hillside mounted heliostats [128] are used to beam down concentrated solar radiation into the nanofluid.

Similarly to ceramic-metallic (*i.e.,* cermet) surface absorbers, nanofluids have the potential to be spectrally selective if the basefluid is non-absorbing in the near and mid infrared (IR), while the absorbing particles are tuned to the solar spectrum. However, selective nanofluid absorbers have not yet been demonstrated. Furthermore, the stability of the nanofluid radiative properties with prolonged exposure to concentrated solar radiation and cycling in a high temperature thermal system requires more investigation.

The use of submicron particles in solar thermal systems is a promising method of achieving heat transfer and storage enhancements, however, concerns related to increased pumping power, material compatibility, and additional cost are currently preventing their widespread use.

The following fundamental areas need to be further explored to improve our understanding of nanofluids: characterization and understanding of the interfacial resistance and the interfacial semi-solid layer; systematic control, characterization and understanding of particle agglomeration and its effects on thermophysical properties and heat transfer performance; and, quantitative and predictive models of nanofluid viscosity. The high-temperature heat transfer performance and material stability of nanofluids needs to be realized before they are successfully adopted in solar thermal applications.

5.5   Summary

The development of heat transfer fluids is essential to the feasibility and efficiency of solar thermal power plants, as it determines the thermal and hydraulic performance of the collector field. In this chapter, the performance of heat transfer fluids was determined by a combination of thermophysical properties rather than by each of the individual properties. Following the work of Murakami and Mikić [79], the following figure of merit has been derived:

5-16
$$FOM = \frac{\rho^{2.0} c_p^{1.6} k^{1.8}}{\mu^{1.4}}$$

based on the assumption of forced turbulent convection inside a uniformly heated collector tube. The new FOM combines the effects of the thermal storage capacity of the fluid, the convective heat transfer from the walls to the fluid, and the hydraulic performance characterized by the pumping power. When evaluated based on this FOM, commonly-used heat transfer fluids generally performed as follows (in order of decreasing FOM): liquid metals, molten salts, oils, and gases. New developments in the field of mixtures, such as multi-component salts and ionic liquids, and composite fluids, such as nanofluids, were reviewed and discussed. Liquidus temperatures well below $100^{o}C$ have been demonstrated using inorganic multi-component salt mixtures (nitrite/nitrate mixtures of Li, Na, K). Ionic liquids were found to have wider temperature ranges than existing synthetic oils used in CSP, but challenges with high viscosity and high cost need to be addressed. Finally, heat transfer enhancements in nanofluids were explored. On the basis of constant pumping power or constant velocity, only a small fraction (<30%) of nanofluids studies report an enhancement in the forced convection heat transfer coefficient compared to the basefluid. Within practical limits, the best performing well-dispersed nanofluids are suspensions of larger spherical particles (~100 nm) since they have lower viscosities as compared to suspensions of small and non-spherical particles.

Chapter 6

6. Near-wall focusing of phase change microparticles for heat transfer enhancement

Phase change material (PCM) suspensions have received wide spread attention for increased thermal storage in solar thermal applications, as well as various other thermal systems such as heat sinks for electronics cooling.

Although previous work has focused on enhancing overall thermal performance using PCM suspension fluids, certain studies have also considered the effects of PCM suspensions on the local heat transfer characteristics. Local heat transfer coefficient variations along the axial direction (h_x) have been reported using both numerical models [33, 34] and in experiments [42-44]. Sabbah et al. showed that h_x increases when the melting interface is near the heated wall and decreases when the interface moves toward the tube center [34]. Meanwhile, Zeng et al. investigated the effects of the *Stefan* number (*Ste*), the PCM melting range (*Mr*), the flow rate, and the particle diameter on the local heat transfer characteristics; the amplitude of the h_x variation was observed to increase with decreasing *Ste* and decreasing *Mr*, which were the dominant parameters in the study. Furthermore, Wang et al. demonstrated local heat transfer enhancements as high as 60% compared to the basefluid and suggested a heat transfer correlation to predict the average heat transfer coefficient during PCM melting [43, 44]. The effects of PCMs on local heat transfer, however, have not been investigated in detail beyond these studies. In particular, understanding the influence of the distribution of PCM particles inside the channel and how it can be used to achieve further heat transfer enhancements was not considered in previous work.

This chapter investigates the effect of focusing micron-sized PCMs to a layer near the heated wall on local heat transfer coefficient. Various techniques have been used to focus, separate and sort microparticles demonstrating the feasibility of the proposed concept, including: pinched flows (*e.g.*, [151]), where flow asymmetries are used to separate particles; inertial focusing, where particles migrate away from the channel center and walls generating continuous particle streams due to inertial lift forces (*e.g.*, [152]); magnetophoresis (*e.g.*, [153]), where magnetic

particles are manipulated using an externally applied magnetic force; and acoustophoresis (*e.g.*, [154]), where particles are driven towards minima of an acoustic force field acting perpendicular to the flow direction due to density and compressibility contrast compared with the basefluid. The effect of focusing particles on heat transfer, however, has not been investigated.

To investigate this effect, a numerical model for fully-developed laminar flow with a constant heat flux applied to one wall is developed. Melting of the focused PCMs is incorporated using a temperature-dependent effective heat capacity. The effect of channel height, height of the focused PCM stream, heat flux, and fluid properties on the peak local *Nusselt* number (Nu^*) and the averaged *Nusselt* number over the melting length (Nu_{melt}) are investigated. Compared to the thermally-developed *Nusselt* number for this geometry ($Nu_o = 5.385$), enhancements in Nu_{melt} and Nu^* were determined. Optimization of the thickness of the focused layer relative to the channel height is considered.

The rest of the chapter explores the effects of various geometrical and material parameters on the features of the local *Nusselt* number (Nu_x). The local heat transfer coefficient profile is rationalized using simple physical arguments in 6.2. Based on this understanding, the effect of focusing the PCMs near the heated wall is explained (6.3). The effects of the PCM-particle mass fraction (ω), mean fluid velocity (U), channel height (H), and heat flux (q'') on Nu_x are explored in 6.4, and the results are summarized using three dimensionless groups 6.5.

To isolate the effects of phase change and particle focusing, the effect of the PCMs on the suspension properties (except for $c_{p,eff}$ during melting) are assumed to be negligible in 6.2-6.5. A physically realistic case is discussed in 6.6 which includes the parasitic effects associated with the dependence of the effective thermal conductivity and viscosity on the addition of PCMs.

6.1 Model Formulation

Nomenclature

c_p	Heat capacity [J/kg-K]	
d_p	Particle diameter [m]	
D_h	Hydraulic diameter (2H for parallel plates) [m]	
D_B	Brownian diffusion coefficient [m^2/s]	
h_{sf}	Latent heat of PCMs [kJ/kg]	
H	Channel height [m or mm]	
k	Thermal conductivity [W/m-K]	
L_{th}	Thermal entrance length [m]	
$\dot{m}$	Mass flow rate [kg/s]	
ML	Dimensionless initial subcooling: $(T - T_i)/\Delta T_o$ [-]	
Mr	Dimensionless melting temperature range: $\Delta T_{melt}/\Delta T_o$ [-]	
Nu	*Nusselt* number [-]	
P	Pressure [Pa]	
Pe	*Peclet* number: UD_h/α [-]	
q''	Heat flux [W/m^2]	
Re	*Reynolds* number: $\rho UD_h/\mu$ [-]	
Ste	*Stefan* number: $\dfrac{c_{p,f}}{\omega h_{sf}/\Delta T_o}$ [-]	
Ste_m	Modified *Stefan* number: $\dfrac{c_{p,f}}{\omega h_{sf}/\Delta T_{melt}}$ [-]	
T	Temperature [K]	
t	Time [s]	
u	Local velocity [m/s]	
U	Mean fluid velocity [m/s]	
x,y	Coordinates [m]	
x^*	Dimensionless position: $x/D_h Pe$ [-]	

Greek Symbols

α	Thermal diffusivity ($k/\rho c_p$) [m^2/s]	
δ	Height of the phase-change stream [m]	

δ_B PCM Brownian diffusion distance [m]

μ Viscosity (Pa·s)

ρ Density [kg/m^3]

ϕ PCM-particle volume fraction [-]

ω PCM-particle mass fraction: $\rho_p\,\phi\,/\rho_{eff}$ [-]

Superscript

*   Local maximum

min   Minimum

-    Onset of melting

+   End of melting

Subscripts

b   Bulk

δ Pertaining to phase-change stream

eff   Effective property of PCM suspension

f   Fluid medium

i   Inlet

melt   Averaged over PCM melt region

o   Thermally-developed

p   Particle (outside of melt region)

w   Heated wall

x   Local

A two-dimensional model (x,y) of laminar flow between parallel plates to is developed to investigate the effect of focusing PCMs near a heated wall. Constant heat flux (q'') is applied to the bottom wall, while the top wall is adiabatic. As shown in Figure 6-1, PCMs are confined to a layer near the bottom wall (δ) which is a fraction of the total channel height (H). Pure fluid and PCM streams are introduced upstream such that the flow is assumed to be hydrodynamically fully-developed by the time it reaches the heated region. The inlet temperature is uniform and well below the onset of melting (*i.e., ML* >> 1). Melting of the PCMs in the phase-change stream is modeled using a temperature-dependent effective heat capacity.
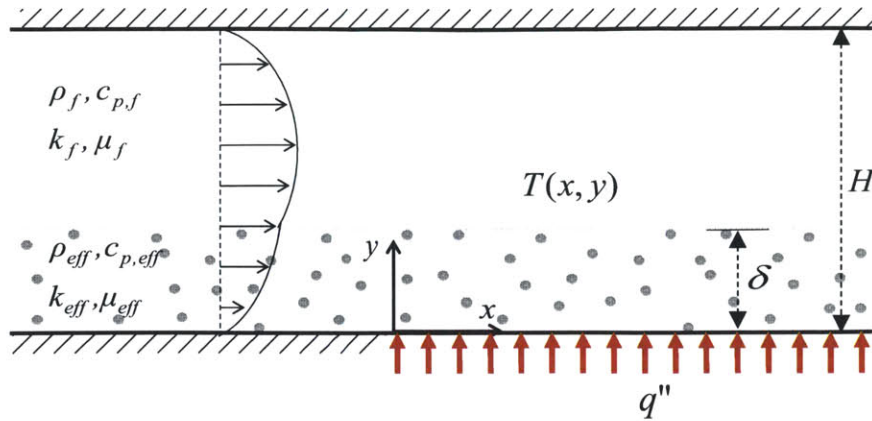
Figure 6-1 | Schematic of PCM-focusing for model formulation.
A 2-D parallel plate channel with fully-developed flow and PCMs confined to a layer (δ) near the heated bottom wall.

In modeling this system, the following simplifications are made in order to focus on the effect of the PCMs:

- Local temperature differences between the PCMs and the surrounding fluid are neglected. This assumption is consistent with bulk fluid treatments [28-31, 33] and was justified for PCMs on the order of a micron [30].

- Temperature dependence of the pure fluid material properties is neglected over the relatively small melting range.

- The differences in the properties of the solid and the post-melting phase of the PCMs are neglected.

- The encapsulating/stabilizing shell is assumed to be negligibly thin compared to the phase-changing core.

- Axial heat conduction and viscous dissipation are neglected.

- The PCM suspension is considered Newtonian.

- PCMs are homogenously distributed throughout the phase-change stream.

- Diffusion of PCMs from the phase-change stream is neglected since it is small relative to the channel height (see 6.1.6)

6.1.1 Effective Suspension Properties

In this study, the thermophysical properties of the PCM suspensions are described using effective models. The following models hold for spherical, non-agglomerating, micron-sized particles with volume fractions up to ~20%.

Density

Considering a simple mechanical mixture of components [155], the effective density of the PCM suspension is equal to:

$$\rho_{eff} = (1-\phi)\rho_f + \phi\rho_p$$

6-1

where ϕ is the particle volume fraction in the PCM stream.

Heat Capacity

The effective heat capacity is represented by a half-period sinusoidal function:

6-2
$$c_{p,eff} = (1-\omega^\delta)c_{p,f}$$
$$+ \omega^\delta\left\{c_{p,p} + \frac{\pi}{2}\left(\frac{h_{sf}}{\Delta T_{melt}} - c_{p,p}\right)\sin\left(\pi\frac{T-T^-}{\Delta T_{melt}}\right)\right\}$$

where ω^δ is the particle mass fraction inside the PCM stream, h_{sf} is the latent heat of PCMs, T^- is the temperature at the onset of melting, and $\Delta T_{melt} (= T^+ - T^-)$ is the melting range. This formulation is consistent with previous effective heat capacity models [28-31, 33].

Thermal Conductivity

Maxwell's effective theory [103] is used to calculate the thermal conductivity of the suspension:

6-3
$$\frac{k_{eff}}{k_f} = \frac{2 + k_p/k_f + 2\phi(k_p/k_f - 1)}{2 + k_p/k_f - \phi(k_p/k_f - 1)}$$

This relation agrees with experimental results for spherical microparticles with volume fractions up to 22% [38]. Microconvection-related enhancements discussed in studies considering larger particles are neglected in this study since they scale with d_p [156]; results from previous studies

110

indicate these effects are negligible for micro/nanoparticles compared to the effects of phase change [35, 38, 42].

Viscosity

The dependence of the effective viscosity (μ_{eff}) of the PCM stream on the volume fraction of particles is computed using Vand's [157] semi-empirical model:

$$6\text{-}4 \qquad \frac{\mu_{eff}}{\mu_f} = (1 - \phi - 1.16\phi^2)^{-2.5}$$

This model holds for non-interacting, hard, uncharged particles and agrees with experimental results for spherical microparticles ($d_p > 0.3$ μm) with volume fractions up to 20% [38]. Although several researchers have suggested higher enhancement coefficients by fitting their experimentally-measured viscosity (*e.g.*, [43]), Vand's model has been predominantly used in previous PCM studies (*e.g.*, [30, 31, 38]).

6.1.2 Governing Equations

Under the above assumptions, the momentum and energy equations for fully-developed laminar flow inside asymmetrically-heated parallel plates with a spatial and temperature dependent specific heat, simplify to the following:

$$6\text{-}5 \qquad \frac{\partial}{\partial y}\left[\mu(y)\frac{\partial u}{\partial y}\right] = \frac{dP}{dx}$$

$$6\text{-}6 \qquad \rho(y)c_p(y,T)u(y)\frac{\partial T}{\partial x} = \frac{\partial}{\partial y}\left[k(y)\frac{\partial T}{\partial y}\right]$$

Eq. 6-5, along with no-slip boundary conditions, is solved analytically in 6.1.3 to determine the velocity profile ($u(y)$) which is incorporated into the energy equation. Numerical methods for solving Eq. 6-6, along with the appropriate boundary conditions, are described in 6.1.4 and validated in 6.1.5.

6.1.3 Momentum Equation

The simplified momentum equation (Eq. 6-5) is written separately for stream 1 (focused PCM suspension) and stream 2 (pure fluid):

111

6-7 $\qquad$ $0 \leq y_1 \leq \delta$ $\qquad$ $\mu_1 \dfrac{\partial^2 u_1}{\partial y_1^2} = \dfrac{dP}{dx}$

6-8 $\qquad$ $0 \leq y_2 \leq H - \delta$ $\qquad$ $\mu_2 \dfrac{\partial^2 u_2}{\partial y_2^2} = \dfrac{dP}{dx}$

where $y_2 = H - y_1$. These two equations are coupled through the following boundary conditions at the walls and at $y = \delta$:

6-9 $\qquad$ $\left. \dfrac{\partial u_1}{\partial y_1} \right|_{y_1=0} = 0$ $\qquad$ (a)

$\qquad$ $\left. \dfrac{\partial u_2}{\partial y_2} \right|_{y_2=0} = 0$ $\qquad$ (b)

$\qquad$ $\mu_1 \left. \dfrac{\partial u_1}{\partial y_1} \right|_{y_1=\delta} = -\mu_2 \left. \dfrac{\partial u_2}{\partial y_2} \right|_{y_2=H-\delta}$ $\qquad$ (c)

$\qquad$ $u_1 \big|_{y_1=\delta} = u_2 \big|_{y_2=H-\delta}$ $\qquad$ (d)

Eqs. 6-6 and 6-8 - 6-9 are readily solved to obtain a fully-developed velocity profile depending on the viscosity ratio (μ_1 / μ_2) and height ratio (δ/H), as shown in Figure 6-2.
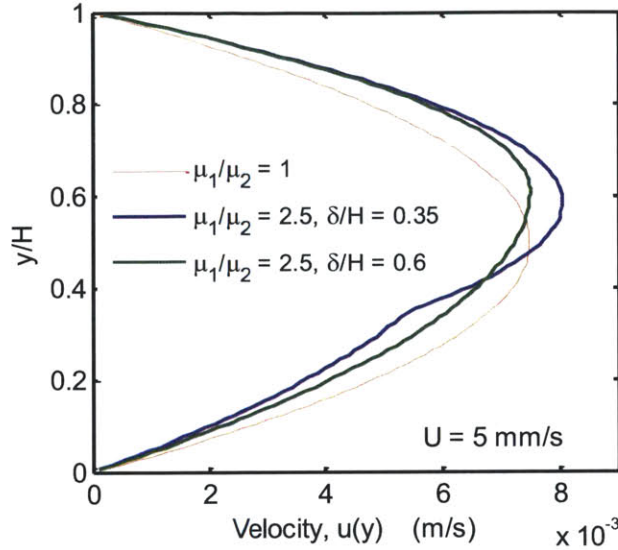
Figure 6-2 | Effect of PCM focusing on velocity profile.
Fully-developed velocity profile inside two-stream channel for the same mean fluid velocity
($U = 5$ mm/s) with different viscosity ratios ($\mu 1/ \mu 2$) and height ratios (δ/H).

6.1.4 Energy Equation

The overall energy equation for fully-developed laminar flow inside parallel plates with spatially-dependent and temperature-dependent thermophysical properties simplifies to Eq. 6-5. The fluid is assumed to enter the region of consideration at a uniform temperature (T_{in}).

6-10
$$T(0,y) = T_{in}$$

The boundary conditions at the walls are incorporated as follows:

$$-k \left.\frac{\partial T}{\partial y}\right|_{y=0} = q''$$

6-11

$$\left.\frac{\partial T}{\partial y}\right|_{y=H} = 0$$

6-12

The energy equations (Eqs. 6-5, 6-10, 6-11) are solved numerically to more easily incorporate the temperature dependent heat capacity. A finite difference scheme is used to solve the equations and the boundary conditions along the y-direction with thermophysical properties

113

defined at each node according to the nodal spatial location and temperature, while the 4th order Runge-Kutta method is used to step explicitly along the x-direction. A mesh refinement study along the y-direction was performed until the maximum variance in the *Nusselt* number is below 0.01%. The model is validated against an analytical solution for the developing local *Nusselt* number below such that it can confidently be used to simulate the effect of phase-change particles on the local heat transfer coefficient.

6.1.5   Validation

To validate the numerical model, it is compared to a known analytical solution on the basis of local *Nusselt* number (Nu_x), defined as follows:

$$6\text{-}13 \qquad\qquad Nu_x = \frac{q'' D_H}{k_f (T_{w,x} - T_{b,x})}$$

where D_H is the hydraulic diameter ($=2H$), k_f is the thermal conductivity of the pure fluid, $T_{w,x}$ is the local wall temperature, and $T_{b,x}$ is the local bulk temperature:

$$6\text{-}14 \qquad\qquad T_{b,x} = \frac{\displaystyle\int_0^H \rho(y) c_p(y,T) U(y) T \, dy}{\displaystyle\int_0^H \rho(y) c_p(y,T) U(y) \, dy}$$

Figure 6-3 shows Nu_x obtained using the numerical model for a thermally-developing flow between parallel plates with constant heat flux from both walls. The result is compared to a correlation recommended by Shah and London which is based on the infinite series analytical solution. The numerical model follows the analytical correlation exactly, thus, validating the accuracy of the numerical model and its ability to model thermally-developing flows.

114
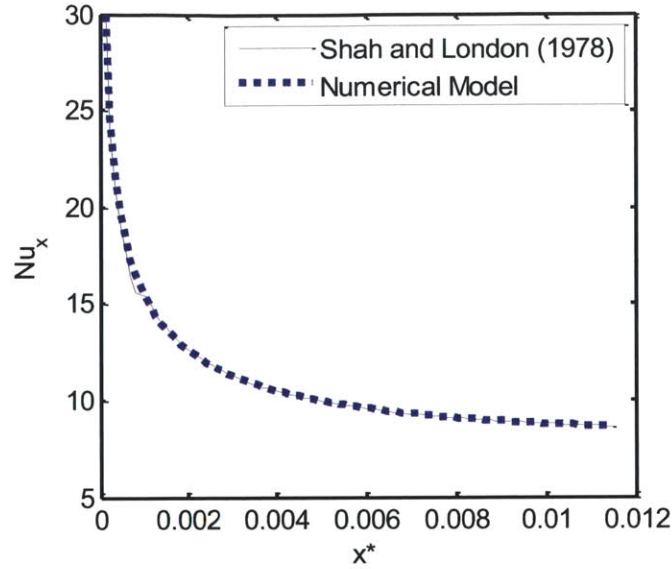
Figure 6-3 | Numerical model validation.
Thermally-developing local *Nusselt* number (Nu_x) as a function of the dimensionless length (x^*); comparing the numerical model (this study) with the analytical solution [158].

6.1.6   Brownian Diffusion of PCMs

Neglecting diffusion of PCMs across the two streams over the characteristic length of PCM melting is justified as described below:

The amount of time needed to fully melt the PCM particles (t_{melt}) can be approximated from an energy balance by dividing the energy required to melt the particles by the heat supplied from the bottom wall. For asymmetrically heated parallel plate geometries, this expression simplifies to the following:

$$6\text{-}15 \qquad\qquad t_{melt} \approx \frac{\rho_f H \omega h_{sf}}{q''}$$

The diffusion length (δ_B) of PCM microparticles through Brownian (random) motion during the melting time can be expressed as:

$$6\text{-}16 \qquad\qquad \delta_B \approx \sqrt{D_B t_{melt}}$$

where the Brownian diffusion coefficient, D_B, is given by the Einstein-Stokes equation:

115

$$6\text{-}17 \qquad\qquad D_B = \frac{k_B T}{3\pi\mu_f d_p}$$

and k_B is the Boltzmann constant, μ_f is the basefluid dynamic viscosity, and d_p is the diameter of a PCM microparticle. Comparing the PCM diffusion length (δ_B) to the channel height, H, the following ratio is obtained:

$$6\text{-}18 \qquad\qquad \frac{\delta_B}{H} \approx \sqrt{\frac{k_B T \rho_f \omega h_{sf}}{3\pi\mu_f d_p q'' H}}$$

For typical values used in the manuscript (*i.e.*, $\rho_f = 992$ kg/m^3, $\mu_f = 6.36 \cdot 10^{-4}$ Pa$\cdot$s, $h_{sf} = 150$ kJ/kg, $\omega = 0.10$, $q'' = 5$ kW/m^2, $H = 0.5$ mm) at a temperature of 313 K and with 1 µm particles, δ_B/H is approximately 0.002. In other words, the typical PCM interdiffusion length considered in the study is approximately 1 µm, which is negligible compared to the channel height (0.5 mm). Thus, diffusion between the two streams (*i.e.*, PCM diffusion) can be neglected.

6.2   Local Nusselt Number Profile

The following case illustrates the local heat transfer behavior during melting of a flowing PCM suspension: PCMs ($h_{sf} = 150$ kJ/kg) suspended in water ($k_f = 0.624$ W/mK, $c_{p,f} = 4067$ J/kgK, $\rho_f = 992$ kg/m^3, $\mu_f = 6.36 \cdot 10^{-4}$ Pa$\cdot$s) with $q'' = 5$ kW/m^2, $U = 5$ mm/s , and $H = 0.5$ mm. These parameters represent a low heat-flux case with Re numbers characteristic of laminar flows in micro/minichannels and high enough Pe numbers (>10) for axial conduction to be negligible.

The following case is considered first: the PCMs are uniformly distributed across the height of the channel (*i.e.*, $\delta = H$) with a mass fraction of 0.20, and assumed to melt across a 3 K temperature range ($\Delta T_{melt} = 3$ K) centered about 313 K. The effective heat capacity of the suspension is shown in Figure 6-4a.

116
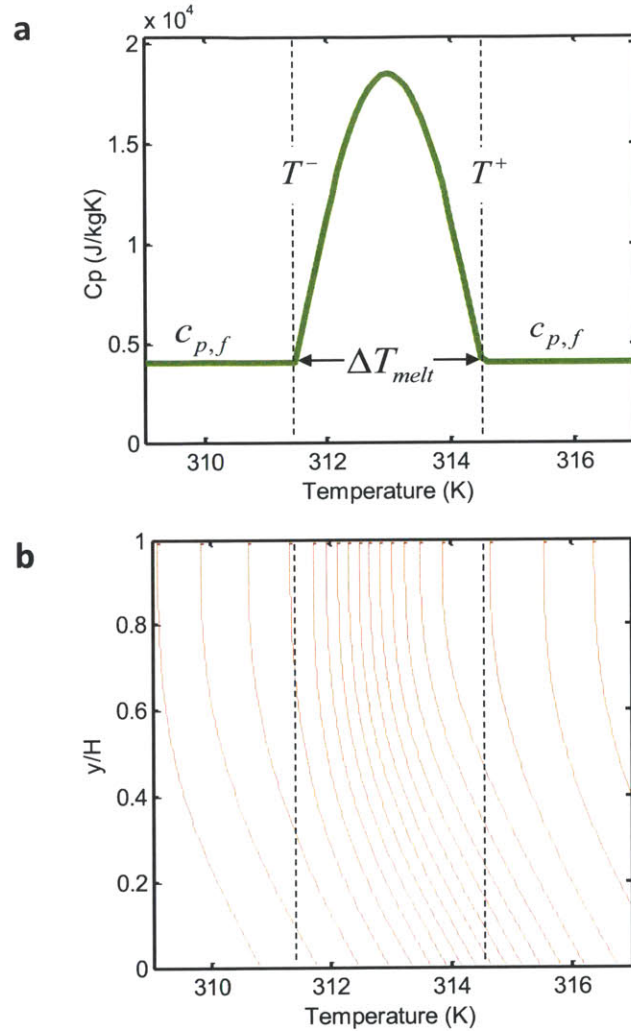
Figure 6-4 | Melting behavior of PCMs and impact on temperature profiles.
a) Effective heat capacity of the PCM suspension as a function of temperature. b) Temperature profiles at regularly spaced intervals (1.7 mm) along the axial direction of the channel. The melting range (ΔT_{melt}) is bound by T- and T+, represented by the region between the dashed lines (U = 5 mm/s, q"= 5 kW/m2, H = 0.5 mm, δ/H = 1, ΔT_{melt} = 3 K, ωh_{sf} = 30 kJ/kg, k = 0.624 W/mK, ρ = 992 kg/m3, $c_{p,f}$ = 4067 J/kgK).

Figure 6-4b shows the temperature profiles of the fluid as it traverses the melting region. The increased effective specific heat over the melting region has the effect of slowing down the rate of temperature rise locally. This observation is explicit in Figure 6-5a where the rate of change of temperature with respect to the axial distance (x) is much lower where the PCMs are melting.

However, the fluid near the heated wall is the first to enter and exit the melting region as shown in Figure 6-4. This movement of the melting interface away from the heated wall leads to maxima and minima in the local heat transfer as shown in Figure 6-5b. Similar effects on the local heat transfer have been observed in previous studies (*e.g.*, [33, 34, 42-44]).
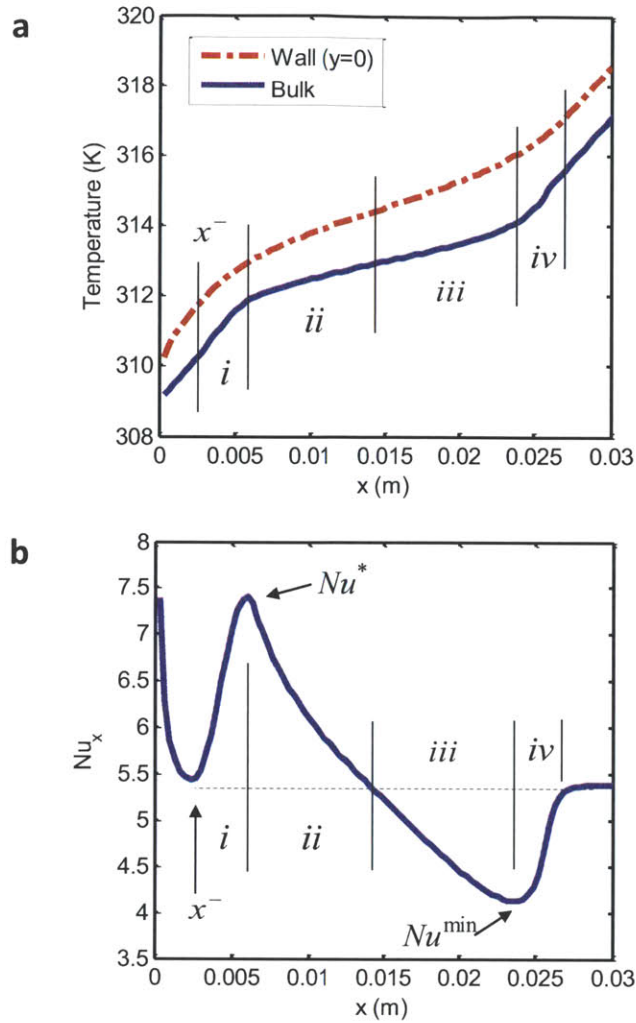
Figure 6-5 | Spatial heat transfer behavior due to PCM melting.
a) Bulk and wall temperatures as a function of length (x) showing a decrease in rate of temperature rise inside melting region and b) local *Nusselt* number as a function of length (x). Melting region divided into sub-regions (*i-iv*) to clarify thermal behavior (same parameters as Figure 6-4 were used).

The shape of Nu_x can be more easily understood by partitioning the melting range into the four sub-regions (*i-iv*) shown in Figure 6-5b.

Sub-region (i):

This sub-region is bound by the onset of melting (x^-) and the maximum local heat transfer coefficient (Nu^*). Initially, the temperature difference between the wall and the bulk is:

$$6\text{-}19 \qquad \Delta T_o \equiv T_{w,x^-} - T_{b,x^-} = \frac{q''D_H}{Nu_o k}$$

118

However, as the fluid near the wall enters the phase-change region, its rate of change of temperature decreases with respect to the bulk. To understand this effect, the local heat transfer coefficient is rewritten in terms of the temperatures at the onset of melting (x^-) and their respective linearized rates of temperature rise as a function of x:

$$6\text{-}20 \qquad h_x \approx \frac{q''}{\Delta T_o - (x - x^-)\left(\frac{\partial T_b}{\partial x} - \frac{\partial T_w}{\partial x}\right)}$$

When $\partial T_b / \partial x > \partial T_w / \partial x$, there is an enhancement in the heat transfer coefficient. For the purpose of this simple treatment, the rate of change of temperature is assumed to be constant in each sub-region and can be approximated using the rate of change for the thermally-developed case:

$$6\text{-}21 \qquad \frac{\partial T_b}{\partial x} \approx \frac{q''}{\dot{m} c_{p,f}} \qquad \text{(a)}$$

$$\frac{\partial T_w}{\partial x} \approx \frac{q''}{\dot{m}(\omega h_{sf} / \Delta T_{melt})} \qquad \text{(b)}$$

Since the rate of temperature rise at the wall (Eq. 6-21b) is inversely proportional to the effective heat capacity during melting of the PCMs $(\omega h_{sf}/\Delta T_{melt})$, it is indeed smaller than the rate of temperature rise of the bulk (Eq. 6-21a). Thus, the temperature difference between the wall and the bulk diminishes over the length of *sub-region (i)*, leading to a maximum (Nu^*). The axial length of this sub-region (Δx_i) is approximated by the distance needed for the bulk temperature to reach the original wall temperature (T_{w,x^-}) at a constant rate of temperature rise:

$$6\text{-}22 \qquad \Delta x_i \approx \frac{\Delta T_o}{\partial T_b / \partial x} = \frac{\dot{m} c_{p,f} D_H}{Nu_o k}$$

Sub-region (ii):

The beginning of this sub-region coincides with Nu^*. At this point, the difference between the wall and bulk temperatures is at a minimum. The bulk and wall regions have approximately the same effective heat capacity $(\omega h_{sf}/\Delta T_{melt})$ since the fluid is inside the melting region; hence, the temperature profile re-develops to its pre-melting shape. By analogy with the thermal entrance

length (L_{th}), the length of this region is proportional to the Pe number (and in turn, the effective heat capacity):

$$6\text{-}23 \qquad \Delta x_{ii} \approx Pe_{melt}D_H \propto \omega h_{sf}/\Delta T_{melt}$$

As compared to the inlet, the thermally diffusivity in *sub-region (ii)* is relatively low because of the high effective heat capacity; this explains why Δx_{ii} is significantly longer than the thermal entrance length.

Sub-region (iii):

This sub-region begins with a developed profile inside the melt region and ends with the minimum local *Nusselt* number (Nu^{min}). The sub-region is physically similar to *sub-region (i)*, except that the specific heat of the wall and the bulk regions are interchanged. The fluid near the wall exits the melting region while the bulk of the fluid remains in the region, amplifying the temperature difference and leading to deterioration of the local heat transfer. By analogy with *sub-region (i)*, the length of *sub-region (iii)* is proportional to $\omega h_{sf}/\Delta T_{melt}$:

$$6\text{-}24 \qquad \Delta x_{iii} \approx \frac{\dot{m}(\omega h_{sf}/\Delta T_{melt})D_H}{Nu_o k}$$

Since $\omega h_{sf}/\Delta T_{melt} > c_{p,f}$, Δx_{iii} is longer than Δx_i, as evident in Figure 6-5b.

Sub-region (iv):

The final sub-region occurs at the exit of the melting region. It begins at the location of Nu^{min}, where the temperature difference between the wall and bulk is at a maximum. The fully-developed temperature profile re-establishes itself over the course of this sub-region.

Its length (Δx_{iv}) is proportional to the thermal entrance length (L_{th}), and thus shorter than Δx_{ii}:

$$6\text{-}25 \qquad \Delta x_{iv} \approx Pe D_H \propto c_{p,f}$$

Although the above treatment is approximate, it rationalizes the basic features of the local heat transfer and will aid in explaining the effect of focusing PCMs near the heated wall.

6.3 Effect of PCM Focusing

The effect of the PCM stream height as a fraction of the channel height is shown in Figure 6-6a. As δ decreases, the deterioration of the local heat transfer vanishes since regions of complete near-wall melting with incomplete melting in the bulk (associated with *sub-regions iii-iv*) are eliminated. Thus, the Nu_x degradation can be circumvented by focusing the PCMs near the heated wall. For cooling applications, eliminating the degradation of Nu_x near the channel exit is desirable for hot-spot prevention (*i.e.,* to minimize the absolute temperature of the wall near the channel exit).

In other applications, the average *Nusselt* number over the entire melting region (Nu_{melt}) could be important if it is desired that the PCMs melt fully (*i.e.,* for improved thermal storage). If the mass fraction of PCMs in the phase-change stream (ω^δ) is kept constant as δ/H decreases, then Nu_{melt} has a distinct peak (29% enhancement) when δ/H is approximately 0.30, as shown in Figure 6-6b. A ~0.30 focused height ratio ($\delta/H \approx 0.30$) was in general found to optimize Nu_{melt} in this geometry (*i.e.,* asymmetrical heating between parallel plates with fully-developed flow).
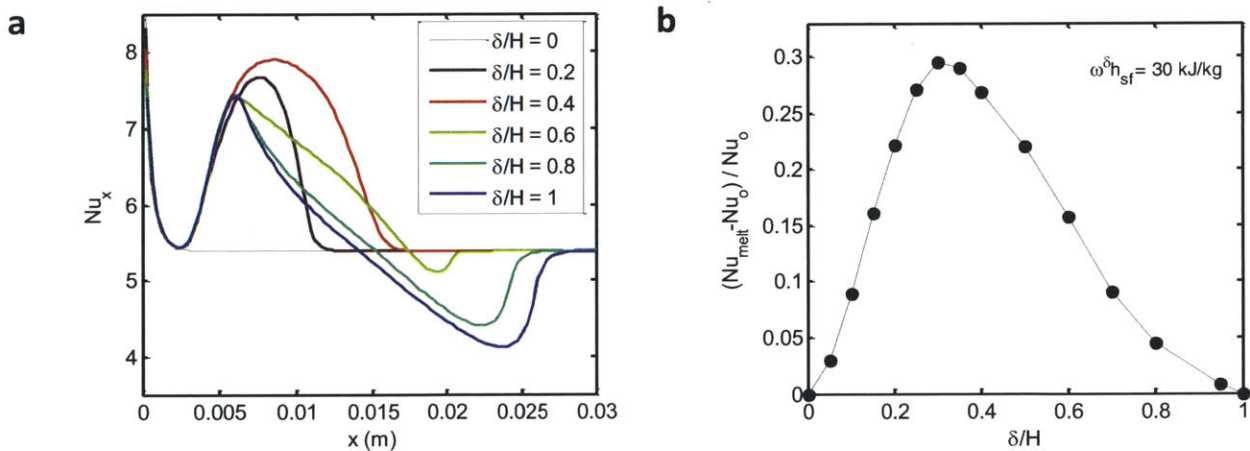
Figure 6-6 | Effect of PCM focusing on local heat transfer coefficient.
a) Local *Nusselt* number (Nu_x) and b) *Nusselt* number averaged over the melting region (Nu_{melt}) for δ/H ranging from 0-1. The mass fraction inside the phase-change stream is kept constant ($\omega^\delta h_{sf}$ = 30 kJ/kg, U = 5 mm/s, q "= 10 kW/m^2, H = 1 mm, ΔT_{melt} = 3 K, k = 0.624 W/mK, ρ = 992 kg/m^3, $c_{p,f}$ = 4067 J/kgK).

6.4 Parametric Study

This section explores the effects of velocity (U), latent heat (ωh_{sf}), heat flux (q ") and channel height (H) on the features of Nu_x. The baseline for this parametric study (solid red in Figure 6-7)

121

shows the case when $U = 5\,mm/s$, $q'' = 5\,kW/m^2$, $H = 0.5\,mm$, $\delta/H = 0.4$, $\Delta T_{melt} = 3\,K$, $\omega h_{sf} = 12\,kJ/kg$.

The velocity of the fluid (U) prolongs the length of the melt region, as shown in Figure 6-7a. Nevertheless, it is interesting to note that changes in velocity have no impact on the magnitude of Nu^*.

The total mass fraction of PCMs ($\omega = \omega^\delta\,\delta/H$) and the heat of fusion (h_{sf}) have a significant influence on the magnitude of heat transfer enhancement since they increase the effective heat capacity during melting. Figure 6-7b shows that the enhancement increases with increasing amount of latent heat in the channel.

The effect of heat flux (q'') on Nu_x is shown in Figure 6-7c. As the heat flux is increased above a threshold value ($\sim 5\,kW/m^2$ in this case), the magnitude of heat transfer enhancement decreases. Below this threshold value, however, the heat flux has little effect on Nu^*.

Although not as apparent as with q'', the height (H) of the channel displays a similar effect as shown in Figure 6-7d: increasing H has a negligible effect for small H values, but Nu^* decreases as H increases beyond a threshold value. The results of Figures 5c and 5d suggest the existence of two regimes: a low ΔT_o (low profile curvature) regime and a high ΔT_o (high profile curvature) regime. The following section will explore this observation further.
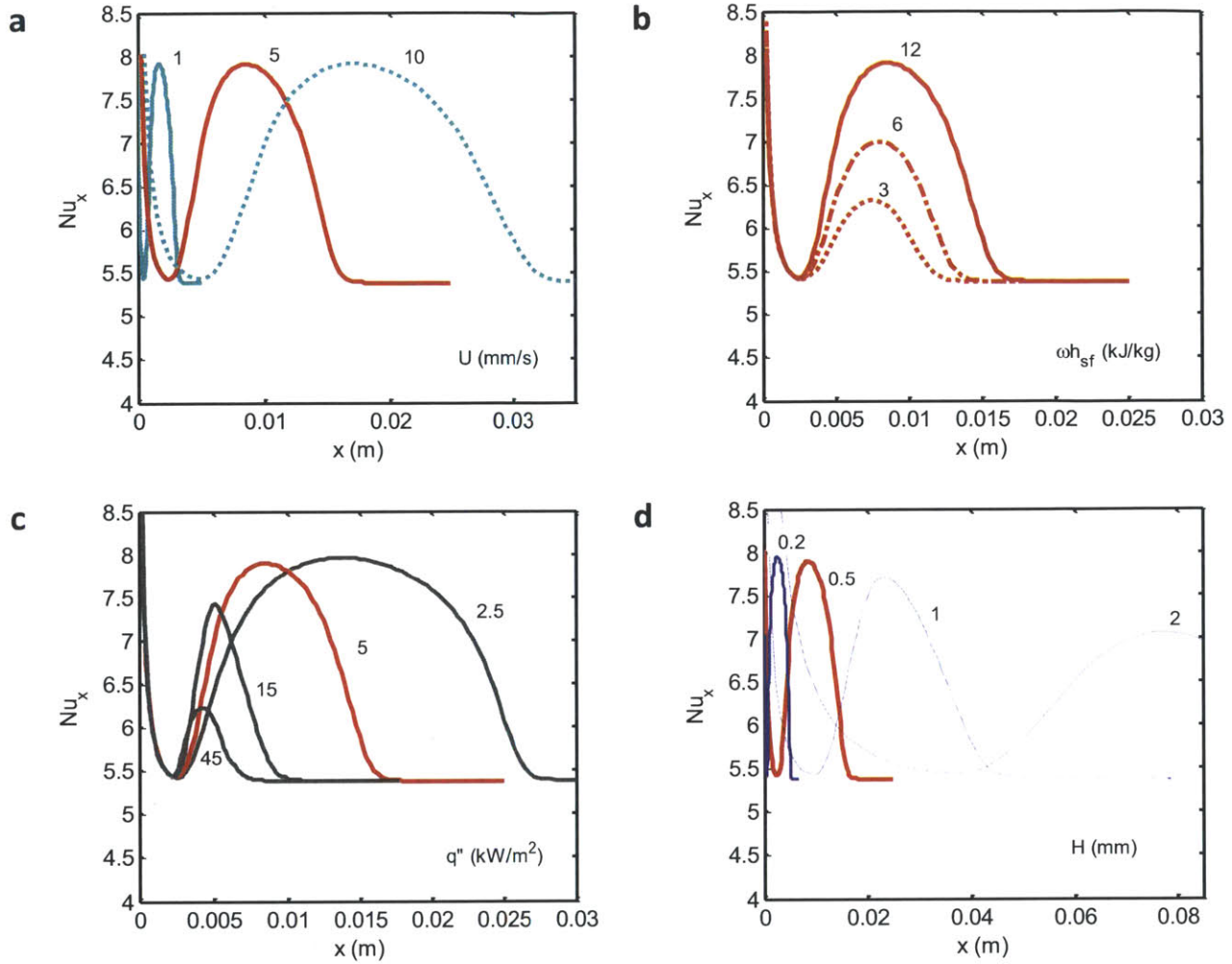
Figure 6-7 | Parametric study of Nu_x for variable latent heat and heat flux.
a) U ranging from 1 to 10 mm/s, b) ωh_{sf} ranging from 3 to 12 kJ/kg, c) q'' ranging from 2.5 to 45 kW/m^2,
and d) H ranging from 0.2 to 2 mm. The baseline in all of the graphs (solid red) shows the case when
$U = 5$ mm/s, $q'' = 5$ kW/m^2, $H = 0.5$ mm, $\delta/H = 0.4$, $\Delta T_{melt} = 3$ K, $\omega h_{sf} = 12$ kJ/kg, $k = 0.624$ W/mK,
$\rho = 992$ kg/m^3, $c_{p,f} = 4067$ J/kgK.

6.5 Dimensionless Groups

Dimensionless groups are presented to generalize the trends discussed above. When the model is simplified to isolate for the effect of phase-change, the following dimensionless groups are relevant: Ste (and Ste_m), a ratio of sensible to latent heat; δ/H, a ratio of the PCM-particle stream height to the channel height; and $\Delta T_{melt}/\Delta T_o$, a ratio of the melting temperature range to the initial temperature difference between the wall and the bulk (typically referred to as Mr):

$$6\text{-}26 \qquad\qquad Ste = \frac{c_{p,f}}{\omega h_{sf}/\Delta T_o}$$

123

6-27
$$\frac{\delta}{H}$$

6-28
$$Mr = \frac{\Delta T_{melt}}{\Delta T_o}$$

According to Figure 6-8a, Nu^* generally decreases as Mr increases but with two distinct slopes. This confirms the existence of two regimes, as suggested in the previous section. When $Mr<1$, the profile curvature does not have a significant effect on Nu^*. When $Mr>1$, however, increasing the heat flux or the channel height results in lowering of the heat transfer enhancement.
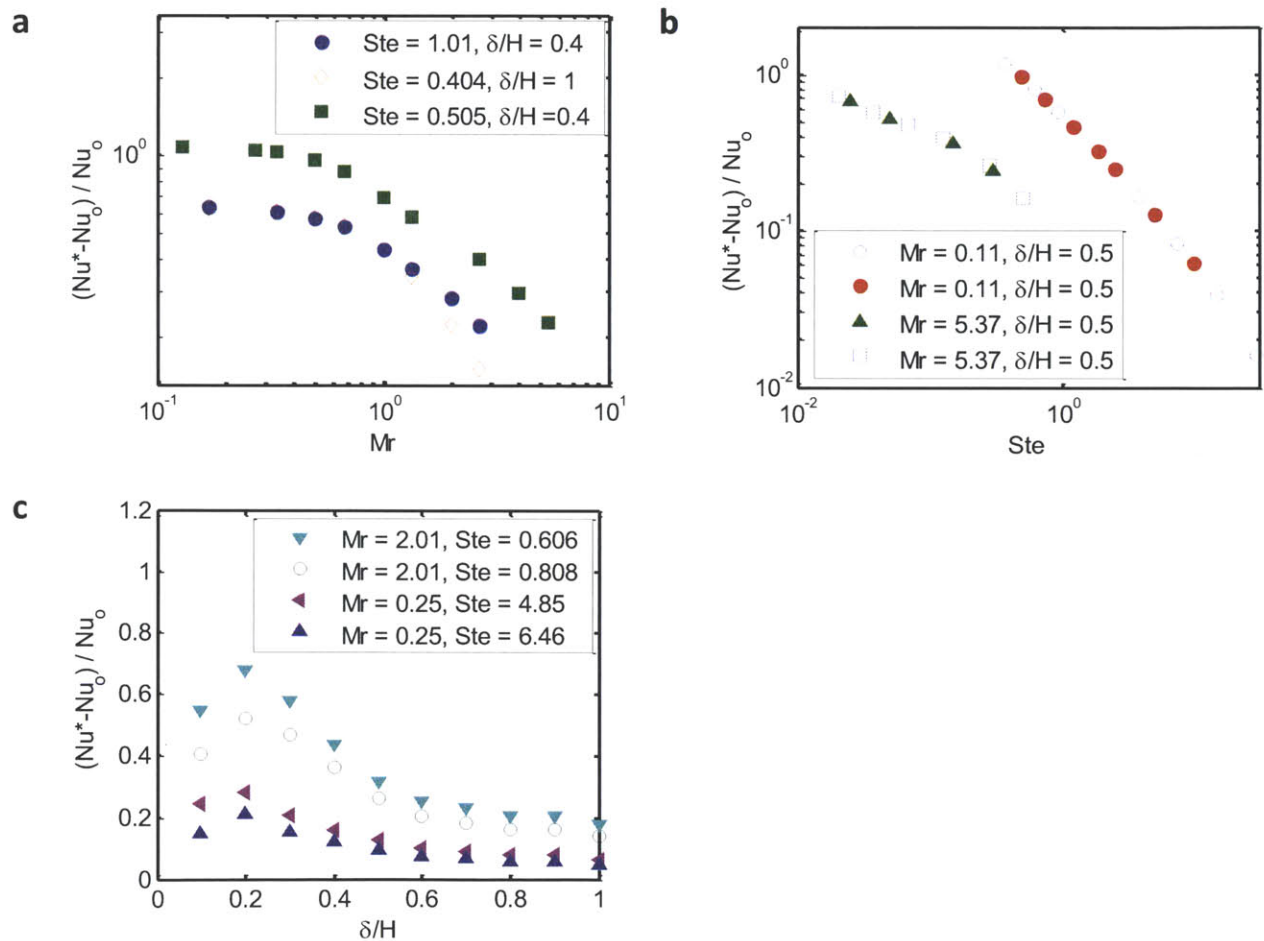
Figure 6-8 | Nu^* with respect to the following dimensionless groups.
a) Mr ranging from 0.1 to 10 (ΔT_{melt} varied), b) Ste, ranging from 0.01 to 30 ($c_{p,f}$ and h_{sf} varied), c) δ/H ranging from 0 to 1 (q'', δ, H varied).

The existence of these two regimes is also apparent in the Nu^* dependency on the Ste (Figure 6-8b). In both regimes, as the ratio of latent to sensible heat increases (decreasing Ste), the

124

enhancement in heat transfer is augmented. However, the enhancement scales differently depending on the regime: the effect of *Ste* is more significant when *Mr* <1.

Finally, the ratio of the PCM stream height to the channel height is shown in Figure 6-8c, where the total mass fraction ($\omega = \omega^{\delta} \, \delta/H$) was kept constant (such that *Ste* = const.) by increasing ω^{δ} to counteract the decrease in δ/H. In general, Nu^{*} increases as the PCMs are focused closer to the heated wall up to $\delta/H \sim 0.25$, at which point focusing the PCMs becomes detrimental. This reduction in Nu^{*} is most likely attributed to the increasing importance of heat conduction between the focused stream and the pure-fluid at small δ scales, which increases the wall temperature regardless of the phase-change.

Within the specified limits, results of this study are summarized in the form of correlations relating Nu^{*} to the three dimensionless groups presented:

6-29
$$[\, Mr <1,\ 0.3 < \frac{\delta}{H} \leq 1\,] \qquad \frac{Nu^{*}-Nu_{o}}{Nu_{o}} = 0.214 Ste^{-0.86} Mr^{-0.08}\left(\frac{\delta}{H}\right)^{-1}$$

6-30
$$[\, Mr >1,\ 0.3 < \frac{\delta}{H} \leq 1\,] \qquad \frac{Nu^{*}-Nu_{o}}{Nu_{o}} = 0.208 Ste_{m}^{-0.44} Mr^{-0.156}\left(\frac{\delta}{H}\right)^{-1}$$

Results from 157 unique simulations were fit to obtain the above expressions. In Eq. 6-30, defining the *Stefan* number with respect to ΔT_{melt} (as opposed to T_{o}) improves the quality of the fit significantly, indicating the dominance of ΔT_{melt} in the $Mr > 1$ regime. The coefficient of determination (R^{2}) for Eq. 6-29 and Eq. 6-30 is 0.99 and 0.86, respectively.
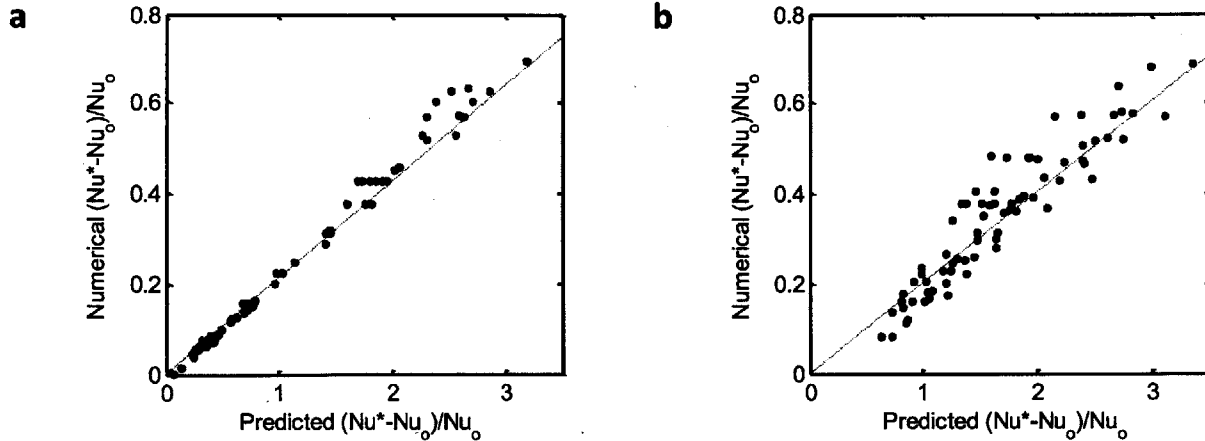
Figure 6-9 | Simulation results for Nu^* enhancement compared to the predicted values.
Predictions based a) Eq. 6-29 ($Mr < 1$), b) Eq. 6-30 ($Mr > 1$).

Eqs. 6-29 - 6-30 were obtained by determining a line of best fit between the simulation results and a power law expression involving the appropriate dimensionless quantities. For the low Mr case (Figure 6-9a), the prediction (Eq. 6-29) matches well with the results as quantified by the high R^2 value (0.99). In the high Mr range (Figure 6-9b), the proposed expression (Eq. 6-30) generally agrees with the numerical results; however, a higher uncertainty is observed ($R^2 = 0.86$) which is most likely because the shape of the effective heat capacity has a complex effect on the magnitude of the Nu^* enhancement in this regime.

6.6   Parasitic effects

It is well known that the addition of PCMs increases the viscosity of fluids and may degrade the overall heat transfer performance. Although the overall pressure drop may be reduced by focusing the PCM particles (compared to the $\delta/H = 1$ case), the presence of a higher viscosity fluid near the heated wall distorts the velocity profile and decreases the local heat transfer performance. The degradation of Nu_x scales approximately linearly with the viscosity ratio of the two streams (μ_{eff}/μ_f), as shown in Figure 6-10a.
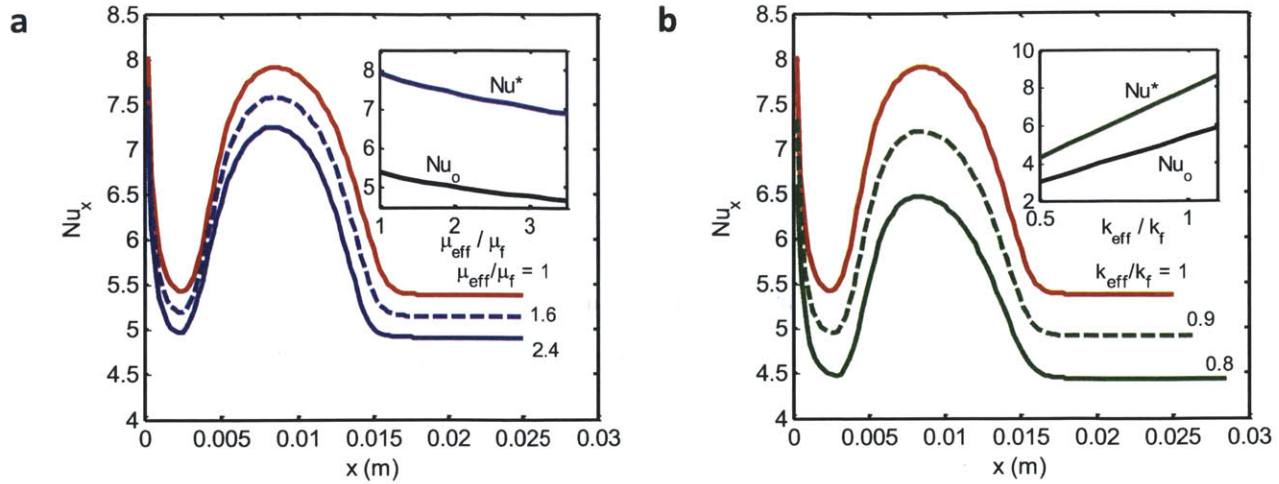
Figure 6-10 | Parasitic effects on Nu_x.
Effect of a) increased viscosity (μ_{eff}) and b) decreased thermal conductivity (k_{eff}) of the focused PCM stream. The baseline in all of the graphs (solid red) shows the case when $U = 5$ mm/s, $q'' = 5$ kW/m^2, $H = 0.5$ mm, $\delta/H = 0.4$, $\Delta T_{melt} = 3$ K, $\omega h_{sf} = 12$ kJ/kg, $k = 0.624$ W/mK, $\rho = 992$ kg/m^3, $c_{p,f} = 4067$ J/kgK.

Similarly, the effective thermal conductivity of the focused stream typically decreases with the addition of PCM particles which further degrades Nu_x as compared to the original pure fluid performance (note: the definition of Nu_x is written with respect to k_f for consistency). As shown in Figure 6-10b, Nu_x also scales approximately linearly with the thermal conductivity ratio of the two streams (k_{eff}/k_f).

Considering the non-negligible nature of these parasitic effects at higher volume fractions, the assumptions of Sections 3.1-3.4 are relaxed, and the idealized enhancements presented in Section 3.2 are re-evaluated based on mePCM property data measured by Zeng et al. [33]: $k_p = 0.211$ W/mK, $c_{p,p} = 1609$ J/kgK, $\rho_p = 1045$ kg/m^3. All other parameters are kept the same (i.e., $\delta/H=0.30$, $\omega^\delta = 0.20$, $h_{sf} = 150$ kJ/kg, water, etc.) such that: $\phi = 0.192$, $\rho_{eff}/\rho_f = 1.01$ (Eq. 6-1), $k_{eff}/k_f = 0.845$ (Eq. 6-3), and $\mu_{eff}/\mu_f = 1.952$ (Eq. 6-4). In this case, Nu^* and Nu_{melt} enhancements of 18.6% and 7.9% were obtained, respectively.

Although lower than the idealized results of 6.3, this result represents an un-optimized enhancement of local heat transfer within the bounds of applicability of the physical models and simplifying assumptions described in 0. In future work, application-dependent optimization should be investigated. Also, correction factors may be appended to Eqs. 6-29 - 6-30 to include the parasitic effects based on measured or predicted properties.

127

6.7 Summary

The effect of focusing micron-sized phase-change particles to a layer near the heated wall of a parallel plate channel was investigated. A numerical model was developed which models melting of the PCMs using a spatially-dependent and temperature-dependent effective heat capacity. In the unfocused case, the melting region was divided into four sub-regions based on the major features of the local *Nusselt* number profile, including the local peak (Nu^*) and minimum (Nu^{min}) *Nusselt* numbers. Deterioration of the local heat transfer (*i.e.*, Nu^{min}) associated with complete near-wall melting with incomplete melting in the bulk is eliminated when PCMs are focused to a region near the heated wall. A parametric study shows that Nu^* increases with increasing particle mass fraction and latent heat as well as with decreasing melting range, channel height and heat flux. The existence of two regimes depending on Mr was observed and the results were summarized using four dimensionless quantities (Ste, Ste_m, δ/H and Mr). The averaged *Nusselt* number over the melting length (Nu_{melt}) and Nu^* are both optimized when the PCMs are focused to within 30% of the channel closest to the heated wall. For a physically realistic case, Nu_{melt} and Nu^* enhancements of 8% and 19% were obtained, respectively. These studies suggest a new strategy to enhance heat transfer with phase change particles for cooling and solar thermal applications.

Chapter 7

7. Conclusions and Recommendations for Future Work

The first part of this thesis investigated the design of actual solar thermophotovoltaic (STPV) devices whose performance is strongly affected by the presence of non-idealities. In Chapter 2, a detailed-balance approach was used to maximize the STPV efficiency over a range of PV bandgaps and optical concentrations by determining the optimal operating temperature, geometry and spectral properties. The impact of non-idealities on the efficiency and the optimal parameters was investigated and explained using dimensionless parameters weighing the relative importance of non-idealities on the emitter-side and the absorber-side. These dimensionless parameters were used as a guide in Chapters 3 and 4 for materials selection and targeted spectral engineering.

Chapter 3 presented the design of an STPV device operating in the high concentration regime which exceeded previously reported efficiencies. Significant improvements in performance were achieved through the use of (i) Si/SiO$_2$ photonic crystals for improved spectral performance of the emitter and vertically aligned multi-walled carbon nanotubes (MWCNTs) for nearly ideal solar absorptivity and (ii) by operating the device in a higher-flux regime (*i.e.*, ~750 suns) through effective thermal spreading between the absorber and emitter, and optimization of the active emitter-to-absorber area ratio. An experimental device was designed to enable facile integration of nanophotonic surfaces while rigorously measuring the energy conversion and loss mechanisms. The following were easily accomplished in the planar experimental device layout: fabrication of nanophotonic surfaces via conventional planar processing techniques, and device optimization via tuning of the emitter-to-absorber area ratio

In Chapter 4, the spectral selectivity of a two-dimensional tantalum photonic crystal was leveraged to reach high-temperatures (~1300 K) at moderate/low optical concentrations (~100 Suns). By scaling up the emitter relative to the absorber and incorporating a sub-bandgap filter, we modeled that a 2D Ta PhC based STPV can exceed the Shockley-Queisser ultimate efficiency limit (for a 0.55 eV cell) at relatively low irradiances (~200 Suns). This chapter demonstrates the components and facilitates the design of such a high-efficiency system.

129

In Chapter 5, a new figure of merit is proposed to evaluate the performance of solar thermal heat transfer fluids. The new metric captures the combined effects of the thermal storage capacity of the fluid, convective heat transfer from the wall to the fluid and hydraulic performance characterized by pumping power. Conventional heat transfer fluids used in solar thermal applications such as oils and molten salts are evaluated based on this new figure of merit. Depending on the desired temperature range of operation, the results can be used a guideline for selection of the appropriate heat transfer fluid. The approach is also applied to emerging heat transfer fluids such as multi-component salts and nanofluids. By placing these new fluids in the same context as the existing ones and evaluating them on the same metric, it becomes apparent where the potential for relative improvements can be expected, what research directions might be fruitful and what physical mechanisms need to be better understood.

Chapter 6 of this thesis aimed to examine the effect of melting of suspended phase-change microparticles on the local heat transfer coefficient. A numerical model was developed to model the physical system. The local heat transfer characteristics displayed a maximum and minimum as the PCMs entered and exited their melting temperature window, respectively. This behavior was partitioned into distinct regions based on the major features of the local *Nusselt* number profile, and explained using physical scaling arguments based on entrance lengths and rates of local temperature rise. It was discovered that if the PCMs are focused to a region near the heated wall of the channel, then the minimum in local heat transfer associated with incomplete melting in the bulk is eliminated. The results of the study were summarized using four dimensionless quantities (Ste, Ste_m, δ/H and Mr) to predict the magnitude of maximum local heat transfer coefficient.

7.1 Contributions

Solid-state systems

1. Developed a framework to guide the design of solar thermophotovoltaics (STPVs)

    a. Identified which specific spectral properties are critical to STPV efficiency

    b. Elucidated the coupling between the relative importance of spectral properties depending on the device geometry

2. Developed an experimental platform for characterizing STPVs

    a. A versatile experimental platform to interchangeably test different STPV components without sacrificing experimental control

    b. An experimental procedure to quantify the energy conversion and loss mechanisms

3. Improved and validated energy conversion/transport models in STPVs

4. Demonstrated significant improvement in STPV efficiency

    a. In the high-concentration regime: exceeded previous experimental studies by roughly 3 times

    b. In the low-concentration regime: leveraged spectral selectivity to achieve comparable performance as the high-concentration regime

Thermal-fluid systems

1. Evaluated existing and emerging heat transfer fluids

    a. Proposed a new figure of merit to capture the thermal storage, heat transfer and pumping power requirements for a heat transfer fluid in a solar thermal system

    b. Evaluated existing and emerging fluids based on the new metric as well as practical issues

2. Phase change material (PCM) microparticle focusing

    a. Developed a physical model to explain the local heat transfer characteristics of a flowing PCM suspension undergoing melting

    b. Discovered and explained a mechanism for enhancement of heat transfer (averaged over the melting region) through control over the distribution of PCM particles inside a channel

7.2 Challenges Faced

In completing this work, I/we faced many challenges and hurdles along the way, particularly with the STPV portion of this thesis. The experiment is complex with many different elements, including thermal, optical, electrical and environmental; with so many elements there is always a higher risk that at any point in time one component will be out of order and delay the overall progress (*i.e.*, the solar simulator lamp would unexpectedly break way before its expected lifetime). Other than those frustrating yet more trivial experimental issues associated with a complex experimental setup and reliance on shared facilities, here is a list of some of the more general challenges associated with lab-scale high temperature STPV experiments:

- *Efficiency versus information.* Aiming for the highest efficiency of the overall STPV process competes with collecting information regarding its operation or visualizing the process itself. For example, in trying to measure the temperature of the absorber-emitter, a thermocouple or IR camera measurement relies on some energy being lost from the process (either through conduction or radiation) which adversely impacts the efficiency. This challenge was overcome via a two-step experimental procedure, where ultimately the useful output photocurrent was used as an indirect measure of the temperature.

- *CNT growth on non-traditional substrates/coatings.* Growing CNTs on a variety of substrates and coatings can be challenging and sometimes unpredictable. First, growing CNTs on rough substrates was not successful; they had to be at least optically smooth (not porous). Second, we originally set out to grow CNTs on Ta coated substrates. We observed however that Ta was a strong gatherer of carbon which led to poor CNT growth, so we decided to coat the Ta with an oxide layer to limit its gathering action during the CNT growth. We then ran into adhesion issues between the alumina and the Ta (and still observed poor CNT growth). The exposed alumina coating on the Ta would delaminate during the high temperature growth process, whereas the alumina underneath the Fe seed layer and CNT growth area would not delaminate (?). Later, we tried ALD coating hafnia on Ta substrates (of Chapter 4). We observed improvements with respect to the alumina coatings (sputter and ebeam), but only if the substrates were annealed at high temperatures in vacuum following the hafnia ALD coating. At some point in our work, we switched to W as the coating and no longer encountered the above issues with

exposed metals in the CVD furnace. From our perspective, however, this issue of direct CNT growth on Ta remains a question that needs to be explored further.

- *Simulating STPV conditions in a lab setting.* We ran across two main issues related to simulating the type of conditions that an STPV device would encounter in the field. First, we faced many challenges with supplying and characterizing highly concentrated sunlight in a lab setting. It seemed like many of the tools available for characterizing the power and the directionality of the incoming light were aimed for lower power or smaller spot size applications. To this day, we have not successfully found a way to provide more collimated yet high intensity sunlight on our substrates. Second, we relied on a high temperature furnace with an inert environment to simulate the conditions that our samples might face when exposed to the STPV experiment. However, these two tests are drastically different both in terms of thermal transients (rapid versus gradual ramps) and environments (vacuum versus inert gas). Some of the initial coatings we attempted to use as absorbers (namely HE6 [159]) survived the furnace tests but did not survive the STPV experiments.

7.3 Recommendations for Future Work

7.3.1 Solid-state systems

Looking ahead, the field of solid-state solar power generation is an exciting one because both our understanding of the energy conversion processes and our ability to process nanostructured materials in a scalable way to control spectral/directional properties are constantly improving. Although this thesis demonstrated nanophotonic STPVs with record-setting efficiencies, several major technological barriers need to be overcome for STPVs to become fully competitive with conventional PV cells in terms of efficiency, reliability and cost.

Several research and development areas should be pursued in hopes of bringing the potential of efficient and dispatchable solar power generation using STPVs closer to reality, including:

- Engineering a practical, fully-integrated and scaled-up nanophotonic device that is compatible with standard tests used for concentrated solar PV

133

- Researching ways to incorporate a back-up system for dispatchable power such a thermo-chemical based storage

- Improving the long-term high-temperature stability of these nanostructured absorber-emitters. Dielectric-filled photonic crystals [53] seem to be promising for simultaneous improvement in thermal stability and directional control.

There are also numerous fundamental questions related to STPVs that should be explored that may result in significant improvements in performance:

- *Order versus disorder of nanostructures for spectral selectivity.* Increasingly we have the ability to not only create ordered nanostructured materials but also to tune the level of disorder. There are several examples in the field of disordered photonics suggesting that there is an ideal level of disorder for applications such as light-trapping in solar cells. How disorder can be used to tune not only solar absorption but selective emission is an open area.

- *Near-field radiative heat transfer.* As two bodies approach each other and finally touch, the transition from a radiative to a conductive mode of heat transfer is not very well understood.

- *Excited charge-carriers.* The presence of excited charge-carriers and their effect on the energy conversion and transport processes in STPVs have not been explored. These effects will show up in the absorber-emitter, and well as in the form of radiative recombination in highly-efficient direct bandgap PV cells. Recently, hot-carrier processes such as multicarrier extraction in PVs and photon-enhanced thermionic emission [160] have received attention due to their potential to enhance the efficiency of the conventional systems. Research should focus on probing charge-carrier generation, transport, and recombination in semiconductor materials and studying the effects of nanostructures, interfaces, and increased temperature operation on photo-enhanced TPVs.

7.3.2   Thermal-fluid systems

The figure of merit proposed in this thesis is useful in comparing single-phase or composite heat transfer fluids but it does not fully capture the benefits of a liquid-vapor phase-change in a fluid such as water. Water is an exceptional heat transfer fluid considering its wide operating temperature range and additional increase in volumetric heat capacity during vaporization. The use of water as a heat transfer fluid for direct steam generation (DSG) is a promising method to increase the efficiency and reduce cost of solar plants because of the high temperature output and the elimination of a heat exchange process. The figure of merit analysis should be extended to include this class of heat transfer fluids in a quantitative way.

In terms of composite fluids (such as nanofluids), their use in solar thermal systems is promising considering they can lead to simultaneous heat transfer and storage enhancements. Future work should address the coupling between thermophysical properties of nanofluids (conductivity, viscosity, heat capacity) both to elucidate the fundamental mechanisms and to target practical thermal-fluid applications. This thesis has identified several fundamental areas that need to explored further: interfacial resistance between the nanoparticles and the surroundings, and the role of interfacial semi-solid layering around the particle, understanding and control over particle agglomeration and its effects on properties, and a quantitative understanding of nanofluid viscosity that is connected to DLVO theory.

The local heat transfer characteristics that were elucidated through the PCM focusing studies can be generalized for any convective heat transfer system with a spatially inhomogeneous distribution of heat capacity. The analysis can be extended to both heating and cooling situations, which would typically both be present in a practical thermal-fluid system. It can be applied to other material systems: fluids with a non-negligible temperature-dependent heat capacitance, chemically-reacting flows (endothermic and exothermic), *etc*.

The mechanism of heat transfer enhancement through PCM focusing can be leveraged in arrays of mini-channels for localized heat dissipation, where the maximum *Nusselt* number can be engineered to align with the hot spot. The design of a system that can focus the phase-change microparticles to a region near the heated wall can be accomplished by selectively applying external body forces on the PCMs, or by carefully designing the flow fields to promote accumulation of particles near the wall.

135

8. Bibliography

1. Turner, J.A., *A realizable renewable energy future.* Science, 1999. **285**(5428): p. 687-689.

2. Laboratory, L.L.N., *Estimated U.S. Energy Use in 2008,* https://publicaffairs.llnl.gov/news/energy/energy.html, Editor. 2008.

3. Harder, N.-P. and P. Würfel, *Theoretical limits of thermophotovoltaic solar energy conversion.* Semicond. Sci. Technol., 2003. **18**(5): p. 151-156.

4. Shockley, W. and H.J. Queisser, *Detailed balance limit of efficiency of p-n junction solar cells.* J. Appl. Phys., 1961. **32**(3): p. 510-519.

5. Rephaeli, E. and S. Fan, *Absorber and emitter for solar thermo-photovoltaic systems to achieve efficiency exceeding the Shockley-Queisser limit.* Opt. Express, 2009. **17**(17): p. 15145-15159.

6. Medina, A.D., *Development of Solar Thermophotovoltaic Systems,* in *Ingeniero en Electrónica.* 2011, Universidad Politecnica de Madrid: Madrid. p. 300.

7. Chan, W.R., et al., *Toward high-energy-density, high-efficiency, and moderate-temperature chip-scale thermophotovoltaics.* Proc. Acad. Nat. Sci. Phila., 2013. **110**(14): p. 5309-14.

8. Datas, A., D.L. Chubb, and A. Veeraragavan, *Steady state analysis of a storage integrated solar thermophotovoltaic (SISTPV) system.* Sol. Energ., 2013. **96**(0): p. 33-45.

9. Chubb, D.L., B.S. Good, and R.A. Lowe, *Solar thermophotovoltaic (STPV) system with thermal energy storage.* AIP Conf. Proc., 1996. **358**(1): p. 181-198.

10. Edenhofer, O., *IPCC special report on renewable energy sources and climate change mitigation.* 2012, International Panel on Climate Change, Working Group III: Geneva, Switzerland.

11. Fan, S., *Photovoltaics: An alternative 'Sun' for solar cells.* Nat Nano, 2014. **9**(2): p. 92-93.

12. Chubb, D.L., *Fundamentals of thermophotovoltaic energy conversion.* 2007, Amsterdam: Elsevier.

13. Datas, A. and C. Algora (2012) *Development and experimental evaluation of a complete solar thermophotovoltaic system.* Prog. Photovolt: Res. Appl., DOI: 10.1002/pip.2201.

14. Vlasov, A.S., et al., *TPV systems with solar powered tungsten emitters.* AIP Conf. Proc., 2007. **890**(1): p. 327-334.

15. Yugami, H., et al., *Solar thermophotovoltaic using Al2O3/Er3Al5O12 eutectic composite selective emitter.* IEEE Photovoltaic Spec. Conf., 2000. **28**: p. 1214-1217.

16. Siegel, R. and J.R. Howell, *Thermal radiation heat transfer.* 1981, Washington: Hemisphere Pub. Corp.

17. Florescu, M., et al., *Improving solar cell efficiency using photonic band-gap materials.* Sol. Energ. Mat. Sol. C., 2007. **91**(17): p. 1599-1610.

18. Bermel, P., et al., *Design and global optimization of high-efficiency thermophotovoltaic systems.* Opt. Express, 2010. **18**(S3): p. A314-A334.

19. Ghebrebrhan, M., et al., *Tailoring thermal emission via Q matching of photonic crystal resonances.* Phys. Rev. A, 2011. **83**(3): p. 033810.

20. Rinnerbauer, V., et al., *Recent developments in high-temperature photonic crystals for energy conversion.* Energy Environ. Sci., 2012. **5**(10): p. 8815-8823.

21. Rinnerbauer, V., et al., *High-temperature stability and selective thermal emission of polycrystalline tantalum photonic crystals.* Opt. Express, 2013. **21**(9): p. 11482-11491.

22. De Zoysa, M., et al., *Conversion of broadband to narrowband thermal emission through energy recycling.* Nat. Photon., 2012. **6**(8): p. 535-539.

23. Celanovic, I., N. Jovanovic, and J. Kassakian, *Two-dimensional tungsten photonic crystals as selective thermal emitters.* Appl. Phys. Lett., 2008. **92**(19): p. 193101-3.

24. Wu, C., et al., *Metamaterial-based integrated plasmonic absorber/emitter for solar thermo-photovoltaic systems.* J. Opt., 2012. **14**(2): p. 024005.

25. Ho, C.J., et al., *On laminar convective cooling performance of hybrid water-based suspensions of Al_2O_3 nanoparticles and MEPCM particles in a circular tube.* International Journal of Heat and Mass Transfer, 2011. **54**(11-12): p. 2397.

26. Dutil, Y., et al., *A review on phase-change materials: Mathematical modeling and simulations.* Renewable and Sustainable Energy Reviews, 2010. **15**(1): p. 112.

27. Zhang, P., Z.W. Ma, and R.Z. Wang, *An overview of phase change material slurries: MPCS and CHS.* Renewable and Sustainable Energy Reviews, 2010. **14**(2): p. 598-614.

28. Alisetti, E.L. and S.K. Roy, *Forced Convection Heat Transfer to Phase Change Material Slurries in Circular Ducts.* Journal of Thermophysics and Heat Transfer., 2000. **14**: p. 115.

29. Hu, X. and Y. Zhang, *Novel insight and numerical analysis of convective heat transfer enhancement with microencapsulated phase change material slurries: laminar flow in a circular tube with constant heat flux.* International Journal of Heat and Mass Transfer, 2002. **45**(15): p. 3163.

30. Kuravi, S., et al., *Numerical Investigation of Flow and Heat Transfer Performance of Nano-Encapsulated Phase Change Material Slurry in Microchannels.* Journal of Heat Transfer, 2009. **131**(6): p. 062901.

31. Zhang, Y., X. Hu, and X. Wang, *Theoretical analysis of convective heat transfer enhancement of microencapsulated phase change material slurries.* Heat and Mass Transfer, 2003. **40**(1): p. 59.

32. Zhao, Z., R. Hao, and Y. Shi, *Parametric Analysis of Enhanced Heat Transfer for Laminar Flow of Microencapsulated Phase Change Suspension in a Circular Tube with Constant Wall Temperature.* Heat Transfer Engineering, 2008. **29**(1): p. 97-106.

33. Zeng, R., et al., *Heat transfer characteristics of microencapsulated phase change material slurry in laminar flow under constant heat flux.* Applied Energy, 2009. **86**(12): p. 2661.

34. Sabbah, R., J. Seyed-Yagoobi, and S. Al-Hallaj, *Heat Transfer Characteristics of Liquid Flow With Micro-Encapsulated Phase Change Material: Numerical Study.* Journal of Heat Transfer, 2011. **133**(12): p. 121702.

35. Charunyakorn, P., S. Sengupta, and S.K. Roy, *Forced convection heat transfer in microencapsulated phase change material slurries: flow in circular ducts.* International Journal of Heat and Mass Transfer, 1991. **34**(3): p. 819.

36. Zhang, Y. and A. Faghri, *Analysis of Forced Convection Heat Transfer in Microencapsulated Phase Change Material Suspensions.* Journal of Thermophysics and Heat Transfer, 1995. **9**(4): p. 727.

37. Hao, Y.L. and Y.X. Tao, *A Numerical Model for Phase-Change Suspensions Flow in Microchannels.* Numerical Heat Transfer, Part A: Applications, 2004. **46**(1): p. 55.

38. Goel, M., S.K. Roy, and S. Sengupta, *Laminar forced convection heat transfer in microcapsulated phase change material suspensions.* International Journal of Heat and Mass Transfer, 1994. **37**(4): p. 593.

39. Roy, S.K. and B.L. Avanic, *Laminar forced convection heat transfer with phase change material emulsions.* International Communications in Heat and Mass Transfer, 1997. **24**(5): p. 653-662.

40. Inaba, H., M.-J. Kim, and A. Horibe, *Melting Heat Transfer Characteristics of Microencapsulated Phase Change Material Slurries With Plural Microcapsules Having Different Diameters.* Journal of Heat Transfer, 2004. **126**(4): p. 558-565.

41. Chen, B., et al., *An experimental study of convective heat transfer with microencapsulated phase change material suspension: Laminar flow in a circular tube under constant heat flux.* Experimental Thermal and Fluid Science, 2008. **32**(8): p. 1638.

42. Yamagishi, Y., et al., *Characteristics of microencapsulated PCM slurry as a heat-transfer fluid.* AIChE Journal, 1999. **45**(4): p. 696.

43. Wang, X., et al., *Flow and heat transfer behaviors of phase change material slurries in a horizontal circular tube.* International Journal of Heat and Mass Transfer, 2007. **50**(13-14): p. 2480.

44. Wang, X., et al., *Heat transfer of microencapsulated PCM slurry flow in a circular tube.* AIChE Journal, 2008. **54**(4): p. 1110-1120.

45. Hassanipour, F. and J.L. Lage, *New Bio-Inspired, Multiphase Forced Convection Cooling by ABS Plastic or Encapsulated Paraffin Beads.* Journal of Heat Transfer, 2010. **132**(7): p. 074501.

46. Ho, C.J., et al., *Water-based suspensions of Al2O3 nanoparticles and MEPCM particles on convection effectiveness in a circular tube.* International Journal of Thermal Sciences, 2011. **50**(5): p. 736-748.

47. Ho, C.J., et al., *On laminar convective cooling performance of hybrid water-based suspensions of Al2O3 nanoparticles and MEPCM particles in a circular tube.* International Journal of Heat and Mass Transfer, 2011. **54**(11–12): p. 2397-2407.

48. Ho, C., et al., *Forced convection performance of a MEPCM suspension through an iso-flux heated circular tube: an experimental study.* Heat and Mass Transfer, 2012. **48**(3): p. 487-496.

49. Bogaerts, W.F. and C.M. Lampert, *Materials for photothermal solar-energy conversion.* Journal Of Materials Science, 1983. **18**(10): p. 2847-2875.

50. Bermel, P., et al., *Selective solar absorbers.* Annual Review of Heat Transfer, 2012. **15**(15).

51. Rinnerbauer, V., et al., *Large-area fabrication of high aspect ratio tantalum photonic crystals for high-temperature selective emitters.* J. Vac. Sci. Technol. B, 2013. **31**(1): p. 011802-7.

52. Rinnerbauer, V., et al., *Metallic Photonic Crystal Absorber-Emitter for Efficient Spectral Control in High-Temperature Solar Thermophotovoltaics.* Advanced Energy Materials, 2014.

53. Chou, J.B., et al., *Design of wide-angle selective absorbers/emitters with dielectric filled metallic photonic crystals for energy applications.* Optics Express, 2014. **22**(S1): p. A144-A154.

54. Röger, M., et al., *Infrared-Reflective Coating on Fused Silica for a Solar High-Temperature Receiver.* Journal of Solar Energy Engineering, 2009. **131**(2): p. 021004-021004.

55. Rahmlow, T.D., et al., *Development of Front Surface, Spectral Control Filters with Greater Temperature Stability for Thermophotovoltaic Energy Conversion.* AIP Conf. Proc., 2007. **890**(1): p. 59-67.

56. Fourspring, P.M., et al., *Optical coatings for thermophotovoltaic spectral control.* Appl. Opt., 2006. **45**(7): p. 1356-1358.

57. Nam, Y., et al., *Solar thermophotovoltaic energy conversion systems with two-dimensional tantalum photonic crystal absorbers and emitters.* Solar Energy Materials and Solar Cells, 2014. **122**(0): p. 287-296.

58. Lenert, A., et al., *A nanophotonic solar thermophotovoltaic device.* Nat Nano, 2014. **9**(2): p. 126-130.

59. Boriskina, S.V. and G. Chen, *Exceeding the solar cell Shockley–Queisser limit via thermal up-conversion of low-energy photons.* Optics Communications, 2014. **314**(0): p. 71-78.

60. Kraemer, D., et al., *High-performance flat-panel solar thermoelectric generators with high thermal concentration.* Nat. Mater., 2011. **10**(7): p. 532-538.

61. Chen, G., *Theoretical efficiency of solar thermoelectric energy generators.* Journal of Applied Physics, 2011. **109**: p. 104908.

62. Telkes, M., *Solar thermoelectric generators.* Journal of Applied Physics, 1954. **25**(6): p. 765-777.

63. Bermel, P., et al., *Tailoring photonic metamaterial resonances for thermal radiation.* Nanoscale Research Letters, 2011. **6**(1): p. 549.

64. Yang, Z.-P., et al., *Experimental observation of an extremely dark material made by a low-density nanotube array.* Nano Lett., 2008. **8**(2): p. 446-451.

65. Yang, Z.-P., et al., *Experimental observation of extremely weak optical scattering from an interlocking carbon nanotube array.* Appl. Opt., 2011. **50**(13): p. 1850-1855.

66. Shi, H., et al., *Low density carbon nanotube forest as an index-matched and near perfect absorption coating*. Appl. Phys. Lett., 2011. **99**(21): p. 211103-211106.

67. Wang, C.A., et al., *High-quantum-efficiency 0.5 eV GaInAsSb/GaSb thermophotovoltaic devices*. Appl. Phys. Lett., 1999. **75**(9): p. 1305-1307.

68. Dashiell, M.W., et al., *Quaternary InGaAsSb thermophotovoltaic diodes*. IEEE Trans. Electron., 2006. **53**(12): p. 2879-2891.

69. Chan, W., et al., *Modeling low-bandgap thermophotovoltaic diodes for high-efficiency portable power generators*. Sol. Energ. Mat. Sol. C., 2010. **94**(3): p. 509-514.

70. Nam, Y., et al. *Solar thermophotovoltaic energy conversion systems with tantalum photonic crystal absorbers and emitters*. in *17th International Conference on Solid-State Sensors, Actuators and Microsystems*. 2013. Barcelona, Spain.

71. Posthuma, N.E., et al., *Emitter formation and contact realization by diffusion for germanium photovoltaic gevices*. IEEE Trans. Electron., 2007. **54**(5): p. 1210-1215.

72. Liu, V. and S. Fan, *S4 : A free electromagnetic solver for layered periodic structures*. Comp. Phys. Comm., 2012. **183**(10): p. 2233-2244.

73. Seraphin, B.O., *Solar energy conversion: solid-state physics aspects*. Solar Energy Conversion: Solid-state Physics Aspects. Vol. 31. 1979: Springer-Verlag.

74. Nam, Y., et al. *Solar thermophotovoltaic energy conversion systems with tantalum photonic crystal absorbers and emitters*. in *The 17th International Conference on Solid-State Sensors, Actuators and Microsystems (Transducers)*. 2013. Barcelona, Spain.

75. Lenert, A., et al., *A Nanophotonic Solar Thermophotovoltaic Device*. Nat. Nanotech., 2013.

76. Becker, M., *Comparison of heat transfer fluids for use in solar thermal power stations*. Electric Power Systems Research, 1980. **3**(3-4): p. 139-150.

77. Mouromtseff, I.E., *Water and forced air cooling of vacuum tubes*. Proceedings of the IRE 1942 **30**(4): p. 190-205.

78. Bonilla, C.F., *Nuclear Engineering*. 1957, New York: McGraw-Hill Book Company, Inc.

79. Murakami, Y. and B.B. Mikic, *Parametric optimization of multichanneled heat sinks for VLSI chip cooling*. Components and Packaging Technologies, IEEE Transactions on, 2001. **24**(1): p. 2-9.

80. McAdams, W.H., *Heat Transmission*. 1954, New York: McGraw-Hill.

81. Dittus, F.W. and L.M.K. Boelter, *Heat transfer in automobile radiators of the tubular type*. University of California Publications in Engineering, 1930. **2**: p. 443-461.

82. Kearney, D., *Solar Electric Generating Stations (SEGS)*. Power Engineering Review, IEEE, 1989: p. 4-8.

83. Moens, L. and D. Blake, *Mechanism of Hydrogen Formation in Solar Parabolic Trough Receivers, NREL/TP-510-42468*. 2008, National Renewable Energy Laboratory: Golden, CO.

84. Kearney, D., et al., *Engineering aspects of a molten salt heat transfer fluid in a trough solar field*. Energy, 2004. **29**(5-6): p. 861-870.

85. Solutia, *Therminol® VP-1*. 2008.

86. Coastal Chemical Co., L.L.C., *HITEC® Heat Transfer Salt*.

87. Sohal, M.S., et al. *Engineering Database of Liquid Salt Thermophysical and Thermochemical Properties, INL/EXT-10-18297.* 2010; Available from: http://www.inl.gov/.

88. NIST, *Thermophysical Properties of Fluid Systems*.

89. Vargaftik, N.B., *Handbook of physical properties of liquids and gases : pure substances and mixtures* 1996: Begell House.

90. Cordaro, J.G., N.C. Rubin, and R.W. Bradshaw, *Multicomponent Molten Salt Mixtures Based on Nitrate/Nitrite Anions*. Journal of Solar Energy Engineering, 2011. **133**: p. 011014:1-4.

91. Zarza, E., et al., *Direct steam generation in parabolic troughs: Final results and conclusions of the DISS project*. Energy, 2004. **29**(5-6): p. 635-644.

92. Pawar, S.H. and L.A. Ekal, *Advances in renewable energy technologies*. 2003.

93. Mills, D., *Advances in solar thermal electricity technology*. Solar Energy, 2001. **76**(1-3): p. 19.

94. Hank, P., et al., *Advances in Parabolic Trough Solar Power Technology*. Journal of Solar Energy Engineering, 2002. **124**(2): p. 109-125.

95. Moens, L., et al., *Advanced Thermal Storage Fluids for Solar Parabolic Trough Systems*. Journal of Solar Energy Engineering, 2003. **125**(1): p. 112-116.

96. Van Valkenburg, M.E., et al. *Ionic liquid heat transfer fluids*. in *Fifteenth Symposium on Thermophysical Properties*. 2003. Boulder, Colorado, U.S.A.

97. Janz, G.J., *Molten salts handbook*. 1967, New York: Academic Press.

98. Bradshaw, R.W., J.G. Cordaro, and N.P. Siegel. *Molten Nitrate Salt Development for Thermal Energy Storage in Parabolic Trough Solar Power Systems*. in *ASME 3rd International Conference on Energy Sustainability*. 2009: ASME.

99. Seddon, K.R., *Ionic Liquids for Clean Technology*. Journal of Chemical Technology & Biotechnology, 1997. **68**(4): p. 351.

100. Fredlake, C.P., et al., *Thermophysical Properties of Imidazolium-Based Ionic Liquids*. Journal of Chemical & Engineering Data, 2004. **49**(4): p. 954.

101. Van Valkenburg, M.E.V., et al., *Thermochemistry of ionic liquid heat-transfer fluids*. Thermochimica Acta, 2005. **425**(1-2): p. 181-188.

102. Chen, H., et al., *Rheological and heat transfer behaviour of the ionic liquid, [C4mim][NTf2]*. International Journal of Heat and Fluid Flow, 2008. **29**(1): p. 149.

103. Maxwell, J.C., *A Treatise on Electricity and Magnetism*. 1881, Clarendon: Oxford.

104. Keblinski, P., J.A. Eastman, and D.G. Cahill, *Nanofluids for thermal transport*. Materials Today, 2005. **8**(6): p. 36.

105. Das, S.K., S.U.S. Choi, and H.E. Patel, *Heat Transfer in Nanofluids - A Review*. Heat Transfer Engineering, 2006. **27**(10): p. 3 - 19.

106. Wang, X.-Q. and A.S. Mujumdar, *Heat transfer characteristics of nanofluids: a review*. International Journal of Thermal Sciences, 2007. **46**(1): p. 1.

107. Yu, W., et al., *Review and Comparison of Nanofluid Thermal Conductivity and Heat Transfer Enhancements*. Heat Transfer Engineering, 2008. **29**(5): p. 432 - 460.

108. Kleinstreuer, C. and Y. Feng, *Experimental and theoretical studies of nanofluid thermal conductivity enhancement: a review*. Nanoscale Research Letters, 2011. **6**(1): p. 229.

109. Oh, S.H., et al., *Ordered Liquid Aluminum at the Interface with Sapphire*. Science, 2005. **310**(5748): p. 661-663.

110. Kaplan, W.D. and Y. Kauffmann, *STRUCTURAL ORDER IN LIQUIDS INDUCED BY INTERFACES WITH CRYSTALS*. Annual Review of Materials Research, 2006. **36**(1): p. 1-48.

111. Gerardi, C., et al., *Nuclear magnetic resonance-based study of ordered layering on the surface of alumina nanoparticles in water*. Applied Physics Letters, 2009. **95**: p. 253104.

112. Timofeeva, E.V., J.L. Routbort, and D. Singh, *Particle shape effects on thermophysical properties of alumina nanofluids*. Journal of Applied Physics, 2009. **106**(1): p. 014304.

113. Wamkam, C.T., et al., *Effects of pH on heat transfer nanofluids containing ZrO_2 and TiO_2 nanoparticles*. Journal of Applied Physics, 2011. **109**(2): p. 024305.

114. Keblinski, P., et al., *Mechanisms of heat flow in suspensions of nano-sized particles (nanofluids)*. International Journal of Heat and Mass Transfer, 2002. **45**(4): p. 855.

115. Buongiorno, J., et al., *A benchmark study on the thermal conductivity of nanofluids*. Journal Of Applied Physics, 2009. **106**(9).

116. Nan, C.W., et al., *Effective thermal conductivity of particulate composites with interfacial thermal resistance*. Journal Of Applied Physics, 1997. **81**(10): p. 6692-6699.

117. Venerus, D.C., et al., *Viscosity Measurements On Colloidal Dispersions (Nanofluids) For Heat Transfer Applications*. Applied Rheology, 2010. **20**(4).

118. Einstein, A., *Eine neue Bestimmung der Moleküldimensionen*. Annalen der Physik, 1906. **324**(2): p. 289.

119. Timofeeva, E.V., et al., *Particle size and interfacial effects on thermo-physical and heat transfer characteristics of water-based alpha-SiC nanofluids*. Nanotechnology, 2010. **21**(21): p. 215703.

120. Anoop, K.B., et al., *Rheological and flow characteristics of nanofluids: Influence of electroviscous effects and particle agglomeration*. Journal of Applied Physics, 2009. **106**(3): p. 034909.

121. Timofeeva, E., et al., *Nanofluids for heat transfer: an engineering approach*. Nanoscale Research Letters, 2011. **6**(1): p. 182.

122. Cao, G., *Nanostructures & nanomaterials : synthesis, properties & applications*. 2004, London: Imperial College Press.

123. Bergman, T.L., *Effect of reduced specific heats of nanofluids on single phase, laminar internal forced convection.* International Journal of Heat and Mass Transfer, 2009. **52**(5-6): p. 1240.

124. Shin, D. and D. Banerjee, *Enhancement of specific heat capacity of high-temperature silica-nanofluids synthesized in alkali chloride salt eutectics for solar thermal-energy storage applications.* International Journal of Heat and Mass Transfer, 2010. **54**(5-6): p. 1064.

125. Kasza, K.E. and M.M. Chen, *Improvement of the Performance of Solar Energy or Waste Heat Utilization Systems by Using Phase-Change Slurry as an Enhanced Heat-Transfer Storage Fluid.* Journal of Solar Energy Engineering, 1985. **107**(3): p. 229-236.

126. Fang, G., et al., *Preparation and characterization of nano-encapsulated n-tetradecane as phase change material for thermal energy storage.* Chemical Engineering Journal, 2009. **153**(1-3): p. 217.

127. Han, Z.H., F.Y. Cao, and B. Yang, *Synthesis and thermal characterization of phase-changeable indium/polyalphaolefin nanofluids.* Applied Physics Letters, 2008. **92**(24): p. 243104.

128. Slocum, A.H., et al., *Concentrated Solar Power on Demand.* Solar Energy, 2011. **85**(7): p. 1519-1529.

129. Otanicar, T.P., P.E. Phelan, and J.S. Golden, *Optical properties of liquids for direct absorption solar thermal energy systems.* Solar Energy, 2009.

130. Taylor, R., et al., *Nanofluid optical property characterization: towards efficient direct absorption solar collectors.* Nanoscale Research Letters, 2011. **6**(1): p. 225.

131. Bohren, C.F. and D.R. Huffman, *Absorption and scattering of light by small particles.* 1998, New York: Wiley-VCH. xiv, 530 p.

132. Kreibig, U. and M. Vollmer, *Optical Properties of Metal Clusters.* 1995, Berlin Heidelberg: Springer.

133. Modest, M.F., *Radiative Heat Transfer.* Second ed. 2003, Burlington: Academic Press. 361.

134. Hu, L., X. Chen, and G. Chen, *Surface-Plasmon Enhanced Near-Bandgap Light Absorption in Silicon Photovoltaics.* Journal of Computational and Theoretical Nanoscience, 2008. **5**: p. 2096.

135. He, Y. and T. Zeng, *First-Principles Study and Model of Dielectric Functions of Silver Nanoparticles.* The Journal of Physical Chemistry C, 2010. **114**(42): p. 18023.

136. Cole, J.R. and N.J. Halas, *Optimized plasmonic nanoparticle distributions for solar spectrum harvesting.* Applied Physics Letters, 2006. **89**(15): p. 153120.

137. Kelly, K.L., et al., *The Optical Properties of Metal Nanoparticles: The Influence of Size, Shape, and Dielectric Environment.* The Journal of Physical Chemistry B, 2002. **107**(3): p. 668.

138. Yu, W., et al., *Thermophysical property-related comparison criteria for nanofluid heat transfer enhancement in turbulent flow.* Applied Physics Letters, 2010. **96**(21): p. 213109.

139. Buongiorno, J., *Convective Transport in Nanofluids*. Journal of Heat Transfer, 2006. **128**(3): p. 240-250.

140. Pak, B.C. and Y.I. Cho, *Hydrodynamic and Heat Transfer Study of Dispersed Fluids with Submicron Metallic Oxide Particles*. Experimental Heat Transfer, 1998. **11**(2): p. 151 - 170.

141. Williams, W., J. Buongiorno, and L.-W. Hu, *Experimental Investigation of Turbulent Convective Heat Transfer and Pressure Loss of Alumina/Water and Zirconia/Water Nanoparticle Colloids (Nanofluids) in Horizontal Tubes*. Journal of Heat Transfer, 2008. **130**(4): p. 042412.

142. Xuan, Y. and Q. Li, *Investigation on Convective Heat Transfer and Flow Features of Nanofluids*. Journal of Heat Transfer, 2003. **125**(1): p. 151-155.

143. Torii, S. and W.-J. Yang, *Heat Transfer Augmentation of Aqueous Suspensions of Nanodiamonds in Turbulent Pipe Flow*. Journal of Heat Transfer, 2009. **131**(4): p. 043203.

144. Yu, W., et al., *Heat transfer to a silicon carbide/water nanofluid*. International Journal of Heat and Mass Transfer, 2009. **52**(15-16): p. 3606.

145. Kulkarni, D.P., et al., *Convective Heat Transfer and Fluid Dynamic Characteristics of SiO₂ Ethylene Glycol/Water Nanofluid*. Heat Transfer Engineering, 2008. **29**(12): p. 1027 - 1035.

146. He, Y., et al., *Heat transfer and flow behaviour of aqueous suspensions of TiO2 nanoparticles (nanofluids) flowing upward through a vertical pipe*. International Journal of Heat and Mass Transfer, 2007. **50**(11-12): p. 2272.

147. Gharagozloo, P.E. and K.E. Goodson, *Temperature-dependent aggregation and diffusion in nanofluids*. International Journal of Heat and Mass Transfer, 2011. **54**(4): p. 797.

148. Otanicar, T.P., et al., *Nanofluid-based direct absorption solar collector*. Journal of Renewable and Sustainable Energy, 2010. **2**(3): p. 033102.

149. Lenert, A. and E.N. Wang, *Optimization of Nanofluid Volumetric Receivers for Solar Thermal Energy Conversion*. Solar Energy, submitted (2011).

150. Epstein, M., A. Segal, and A. Yogev, *A molten salt system with a ground base-integrated solar receiver storage tank*. J. Phys. IV France, 1999. **09**(PR3): p. 95-104.

151. Takagi, J., et al., *Continuous particle separation in a microchannel having asymmetrically arranged multiple branches*. Lab on a Chip, 2005. **5**(7).

152. Di Carlo, D., et al., *Continuous inertial focusing, ordering, and separation of particles in microchannels*. Proceedings of the National Academy of Sciences of the United States of America, 2007. **104**(48): p. 18892.

153. Pamme, N. and A. Manz, *On-Chip Free-Flow Magnetophoresis: Continuous Flow Separation of Magnetic Particles and Agglomerates*. Analytical Chemistry, 2004. **76**(24): p. 7250.

154. Petersson, F., et al., *Free Flow Acoustophoresis: Microfluidic-Based Mode of Particle and Cell Separation*. Analytical Chemistry, 2007. **79**(14): p. 5117.

145

155. Callen, H.B., *Thermodynamics and an introduction to thermostatistics*. 1985, New York: Wiley.

156. Leal, L.G., *On the Effective Conductivity of a Dilute Suspension of Spherical Drops in the Limit of Low Particle Peclet Number*. Chemical Engineering Communications, 1973. **1**(1): p. 21.

157. Vand, V., *Theory of Viscosity of Concentrated Suspensions*. Nature, 1945. **155**(3934): p. 364.

158. Shah, R.K. and A.L. London, *Laminar Flow Forced Convections in Ducts*. Advances in Heat Transfer. 1978, New York: Academic Press. p.182.

159. Brandt, R., C. Bird, and G. Neuer, *Emissivity reference paints for high temperature applications*. Measurement, 2008. **41**(7): p. 731-736.

160. Schwede, J.W., et al., *Photon-enhanced thermionic emission for solar concentrator systems*. Nat. Mater., 2010. **9**(9): p. 762-767.